VSEBINA   CONTENT

Obnovitev članstva v strokovnem društvu MIDEM in iz tega izhajajoče ugodnosti in obveznosti

Spoštovani,

V svojem več desetletij dolgem obstoju in delovanju smo si prizadevali narediti društvo privlačno in koristno vsem članom.Z delovanjem društva ste se srečali tudi vi in se odločili, da se v društvo včlanite. Življenske poti, zaposlitev in strokovno zanimanje pa se z leti spreminjajo, najrazličnejši dogodki, izzivi in odločitve so vas morda usmerili v povsem druga področja in vaš interes za delovanje ali članstvo v društvu se je z leti močno spremenil, morda izginil. Morda pa vas aktivnosti društva kljub temu še vedno zanimajo, če ne drugače, kot spomin na prijetne čase, ki smo jih skupaj preživeli. Spremenili so se tudi naslovi in način komuniciranja.

Ker je seznam članstva postal dolg, očitno pa je, da mnogi nekdanji člani nimajo več interesa za sodelovanje v društvu, se je Izvršilni odbor društva odločil, da stanje članstva uredi in **vas zato prosi, da izpolnite in nam pošljete obrazec priložen na koncu revije.**

Naj vas ponovno spomnimo na ugodnosti, ki izhajajo iz vašega članstva. Kot član strokovnega društva prejemate revijo »Informacije MIDEM«, povabljeni ste na strokovne konference, kjer lahko predstavite svoje raziskovalne in razvojne dosežke ali srečate stare znance in nove, povabljene predavatelje s področja, ki vas zanima. O svojih dosežkih in problemih lahko poročate v strokovni reviji, ki ima ugleden IMPACT faktor. S svojimi predlogi lahko usmerjate delovanje društva.

Vaša obveza je plačilo članarine 25 EUR na leto. Članarino lahko plačate na transakcijski račun društva pri A-banki: 051008010631192. Pri nakazilu ne pozabite navesti svojega imena!

Upamo, da vas delovanje društva še vedno zanima in da boste članstvo obnovili. Žal pa bomo morali dosedanje člane, ki članstva ne boste obnovili do konca leta 2011, brisati iz seznama članstva.

Prijavnice pošljite na naslov:

MIDEM pri MIKROIKS

Stegne 11

1521 Ljubljana

Ljubljana, junij 2011

Izvršilni odbor društva

BV$_{CEO}$ ENGINEERING IN SOI LBT STRUCTURE WITH TOP CONTACTED BASE

Marko Koričić, Tomislav Suligoj

Department of Electronics, Microelectronics, Computing and Intelligent Systems, Faculty of Electrical Engineering and Computing, University of Zagreb, Zagreb, Croatia

Key words: SOI, lateral bipolar transistor, extrinsic base, charge sharing effect, common-emitter breakdown voltage, cutoff frequency

Abstract: Properties of SOI LBT structure with the base contact on top are analyzed by device simulations. The effect of the extrinsic base width on the common-emitter breakdown voltage (BV$_{CEO}$) is studied in detail. Charge sharing between extrinsic and intrinsic base acceptors can be controlled to achieve fully depleted collector. Shielding of the electric field across intrinsic junction by the extrinsic base electric field can be used to limit the peak value of the electric field along the current path in the collector-base depletion region and to increase the value of BV$_{CEO}$. Two peaks of electric field appear in the base-collector depletion region – the first one at the intrinsic junction and the second in the drift region toward extrinsic collector. The area in which breakdown occurs depends on the value of the electric field in two peaks, which can be controlled by the extrinsic base width (w$_{bext}$).

Inženiring parametra *BV$_{CEO}$* v SOI LBT tranzistorski strukturi z baznim kontaktom na vrhu

Kjučne besede: SOI, bipolarni tranzistor, ekstrinzična baza, deljenje naboja, prebojna napetost s skupnim emiterjem, mejna frekvenca

Izvleček: Simulirali smo lastnosti SOI LBT tranzistorske strukture z baznim kontaktom na vrhu. Podrobno smo proučili vpliv širine ekstrinzične baze na prebojno napetost tranzistorja, BV$_{CEO}$. Kontroliramo lahko porazdelitev naboja akceptorjev intrinzične in ekstrinzične baze, da dosežemo popolnoma osiromašen kolektor. Senčenje električnega polja ekstrinzične baze čez intrinzičen spoj lahko uporabimo za omejitev najvišje vrednosti električnega polja vzdolž tokovne poti v osiromašenem področju spoja kolektor-baza, kakor tudi za povečanje prebojne napetosti BV$_{CEO}$. Pojavita se dva vrhova električnega polja v osiromašenem področju spoja baza-kolektor. Področje, kjer pride do preboja, je odvisno od vrednosti električnega polja teh dveh vrhov, ki ju lahko kontroliramo s širino baze, *w$_{bext}$*.

1. Introduction

Recently, the extremely-thin silicon-on-insulator (SOI) has been marked as a potential CMOS technology for 22 nm node and below, /1/. Small parasitic capacitances inherent for SOI technology, good electrostatic behavior and low variability due to undoped channel promise a good solution for short channel effects (SCE) and scaling properties of such CMOS. This trend in IC industry will force SOI wafer manufacturers to improve wafer production in terms of lower defect density and reduced cost. It can be expected that wafer cost of not only ultra-thin-film SOI, but also thicker film SOI, will be reduced in the near future. In the past years, thin-film SOI technology has been proposed as a potential technology for radio-frequency (RF) system-on-chip (SoC) integration /2/, /3/. Excellent characteristics regarding the device isolation and small parasitic capacitances, as well as higher quality passives compared to bulk-silicon technologies, make this technology appropriate for low-power battery supplied applications like mobile phones, GPS, WiFi, etc. In order to achieve SoC level of integration for RF applications, bipolar transistors are desired in a technology platform due to their superior analog performance such as lower noise figure and higher gain. Vertical bipolar transistors in SOI may become prohibitively expensive due to more complex process /4/, which in addition to the higher cost of SOI wafers may result in a technology that is not economically viable. On the other hand, lateral bipolar transistors (LBTs) in SOI can be fabricated in a process that is less complex with the significant cost reduction compared to the vertical bipolar transistors, either in bulk or SOI substrates. It can be expected that cost of technology will be reduced further with the advance in SOI wafer manufacturing. Due to the nature of intrinsic base fabrication, which relies on the spacer technique and lateral redistribution of impurities, cutoff frequencies (*f$_T$*) of SOI LBTs above 20 GHz were not reported. The only LBT with reported state-of-the-art electrical performance is Horizontal Current Bipolar Transistor (HCBT) but it is fabricated in bulk-silicon wafers /5/. However, reported AC performance of SOI LBTs is still suitable for applications in microwave frequency range including the most important wireless application standards. Several LBT structures have been proposed so far and can be roughly categorized with respect to the base contact position as laterally contacted /6/, /7/, /8/ and top-contacted structures /2/, /3/, /9/, /10/. One benefit of placing the base contact on the top is that transistor length can be increased in the third dimension by the mask design if higher current drive is needed in the applications. In the case of laterally contacted base, i.e. two-sided base contact, transistor

operating current cannot be increased by increasing the emitter length, because the intrinsic base resistance would be increased. The ultimate result is that AC performance of the transistor is degraded through the reduction of maximum oscillation frequency (f_{max}). To overcome this issue, transistors of unit emitter size can be connected in parallel, which gives less flexibility in the circuit design. In order to achieve a SoC level of integration, transistors with different values of breakdown voltages should be available in a certain technology. In standard vertical transistors it is accomplished by the different parameters of the selectively implanted collector, which implies the usage of additional lithographic masks and results in an increased process complexity and ultimately higher cost of technology. On the other hand, in LBT structures with top contacted base, different values of breakdown voltages can be obtained by the mask design and the control of the width of the base contact region, i.e. extrinsic base width (w_{bext}), without any increase in the process complexity. In this paper, design tradeoff between cutoff frequency (f_T) and common-emitter breakdown voltage (BV_{CEO}), specific for SOI LBT structure with top-contacted base are analyzed by the device simulations. Physical mechanisms in the extrinsic base effect on transistor's breakdown voltage are analyzed in detail.

2. Simulation structure

A typical LBT structure such as the one reported in /2/ is analyzed by device simulation in MEDICI. The highest maximum oscillation frequency (f_{max}) and common emitter current gain (β) as well as the lowest base resistance (R_B) among all LBTs are reported for this structure. Cross-section of the device with marked geometrical parameters and the doping profile of the intrinsic transistor are shown in Fig. 1 and 2, respectively. Technological parameters are summarized in Table 1. Emitter height (h_E) is determined by the thickness of the silicon on insulator film and the small link-base region (l_b), which is defined during the extrinsic

Table 1. Technological and geometrical parameters of the soi lbt simulation structure

N_{ABext}, (cm^{-3})	N_{DC}, (cm^{-3})	N_{DE}, (cm^{-3})	w_{bext}, (nm)	l_b, (nm)	h_E, (nm)	d_{poly}, (nm)	d_E, (nm)	d_C, (nm)	d_{OX}, (nm)
$2 \cdot 10^{20}$	$1.5 \cdot 10^{17}$	$1.8 \cdot 10^{20}$	500	70	120	200	300	500	300
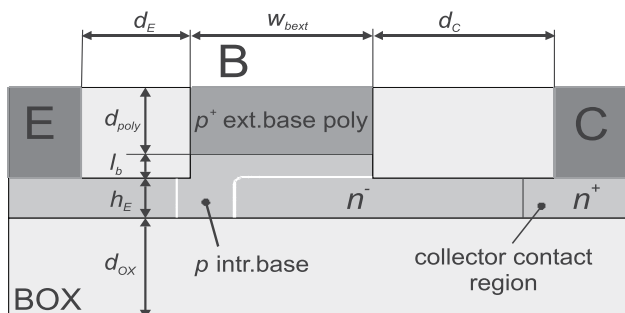
Fig. 1.   Cross-section of the device simulation structure with marked geometrical parameters.
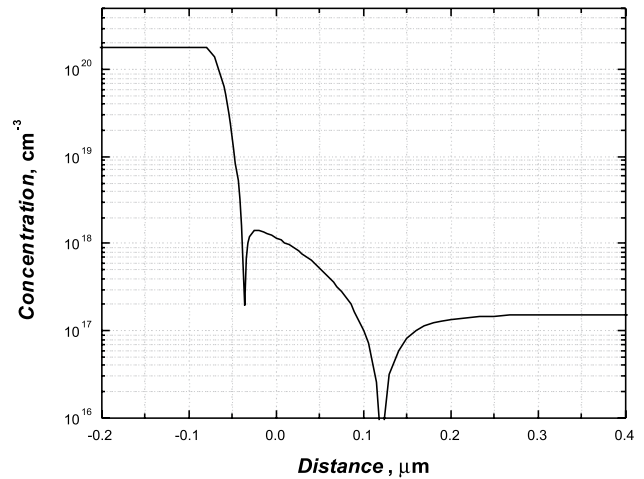
Fig. 2.   Doping profile of the intrinsic transistor.

base polysilicon overetching. In this way, the extrinsic base profile, which is diffused from the extrinsic-base polysilicon, does not overlap the upper edge of the emitter, which could reduce the current gain and degrade base current ideality at lower base-emitter voltages due to the high-field effects and band to band tunneling /11/. Intrinsic transistor is formed by ion implantation of the intrinsic base and emitter, which are separated by the spacer formed on the sidewall defined during the extrinsic base polysilicon etching. Later on in the process, dopants are laterally diffused to form the final intrinsic transistor profile. This represents the fundamental limit on the control of the intrinsic base profile and basewidths cannot be scaled below 100 nm as it is routinely done in standard vertical bipolar transistors. Since the emitter region is not implemented in polysilicon, the distance between emitter contact and the base-emitter junction should be larger than the minority hole diffusion length in order to obtain smaller associated component of the base current and the larger current gain. The minimum distance between highly doped n^+ collector contact region, i.e. extrinsic collector, and the p^+ extrinsic base is limited by breakdown voltages of the transistor. Extrinsic base polysilicon should be highly doped and thick enough to suppress electron diffusion to the extrinsic base region, which could
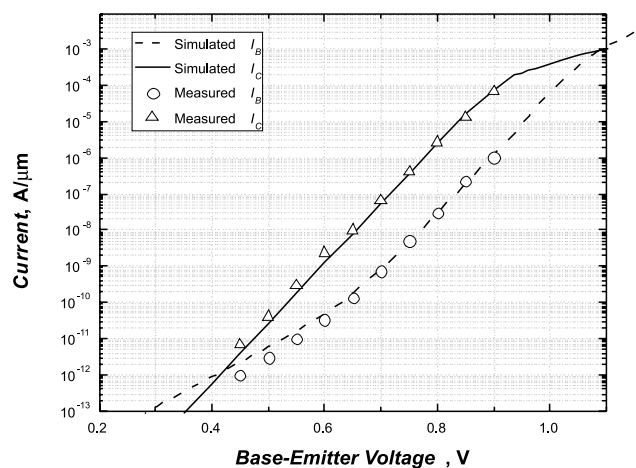
Fig. 3.   Simulated Gummel characteristics. Measured data from /2/ is included for reference.

increase the base current and degrade the current gain (β). This structure has the base contact placed on the top and the base current is supplied only from one direction. Therefore, one-sided base contact is formed, which is not beneficial regarding the value of the base resistance (R_B). Nevertheless, the smallest R_B and the highest f_{max} value among SOI LBTs are reported for this structure, owing to a small thickness of SOI film and silicided base contact, which results in a small intrinsic component of the base resistance and a small contact resistance, respectively.

3. Simulation of electrical characteristics

Simulated Gummel characteristics of the transistor are presented in Fig. 3. Measured data is taken from /2/ for the reference. Doping profile in the intrinsic base is adjusted to get reasonable fit of the collector current. Summary of the simulated characteristics is given in Table 2.

Table 2. Summary of the simulated electrical characteristics

β	f_T, (GHz)	f_{max}, (GHz)	R_B, (Ω)	C_{jBC}, (fF)
83	12.7	67.1	250	1.55

3.1. Analysis of common emitter breakdown voltage and cutoff frequency

Tradeoff between speed and the breakdown voltage in bipolar transistors is well known. In order to suppress base widening at higher collector currents (i.e. Kirk effect) and to increase the cutoff frequency of the transistor (f_T), collector doping concentrations are increased, which results in a higher electric field in the base collector depletion region and lower value of breakdown voltages. Common emitter breakdown voltage (BV_{CEO}) is more important since it is typically 2 to 3 times lower than the common base breakdown voltage (BV_{CBO}) and is responsible for evaluation of transistor's safe operating area. The tradeoff is usually evaluated in terms of ($f_T BV_{CEO}$) product, bounded by the Johnson's limit /12/, which approximately equals 200 GHzV and 400 GHzV for implanted base and SiGe epi-base transistors, respectively /13/. Cutoff frequency (f_T) and common emitter breakdown voltage (BV_{CEO}) are simulated in MEDICI. f_T is calculated from AC analysis. Y-parameters are simulated and converted to h-parameters. f_T is determined as the frequency at which, h_{21} falls to unity. For evaluation of the common emitter breakdown voltage, base current reversal method in forced V_{BE} measurement is used /13/. Base-emitter voltage (V_{BE}) is set to 0.7 V and collector-emitter voltage (V_{CE}) is swept. BV_{CEO} is determined as the V_{CE} at which the base current changes the sign, i.e. turns from positive to negative. Non-local impact ionization model based on lucky electron model with hard threshold energy /14/ is used in simulations. All BV_{CEO} simulations are done with standard drift-diffusion model and the effects of self-heating are not considered. However, simulations

are done for V_{BE} of 0.7 V at which collector current is small and no substantial self-heating is expected.

The unique geometry of LBTs with the base contact placed on the top results in a collector region which is surrounded by the extrinsic base from the top, the intrinsic base from one side and buried oxide from the bottom (Fig. 1). In the forward active mode of transistor operation, the base-collector junction is reversely polarized and the electric field is supported by the fixed charge in the depletion region. In the case of top contacted structure, there are two components of the electric field. Vertical component originates from the electric field lines which are terminated between collector donor charge and the extrinsic base acceptors, whereas horizontal component originates from the electric field lines which are terminated on the intrinsic base acceptors. Total amount of the collector charge is limited by the donor concentration in the collector and the thickness of the silicon on insulator film. This two-dimensional effect of collector charge sharing between extrinsic and intrinsic base acceptors, i.e. vertical and horizontal component of the electric field can be controlled in the way that collector becomes fully depleted and breakdown voltage improved for transistors with wider extrinsic base (w_{bext}).

At first, dependence of the BV_{CEO} on extrinsic base width (w_{bext}) is investigated. Simulations are done for the structures with different collector concentrations (N_{DC}). Intrinsic base profile is kept the same in the simulations, meaning that intrinsic base is narrower and current gain (β) slightly higher for transistors with higher collector concentration. Results are shown in Fig. 4. For the doping concentrations up to $2.5 \cdot 10^{17}$ cm^{-3} the effect of the BV_{CEO} improvement can be observed if the extrinsic base width (w_{bext}) is increased. BV_{CEO} value saturates for extrinsic base width larger than 0.8 μm. Therefore, engineering of the breakdown voltage by the mask design is possible for extrinsic base widths up to 0.8 μm. For collector doping concentrations larger than $2.5 \cdot 10^{17}$ cm^{-3}, breakdown voltages are sharply reduced and
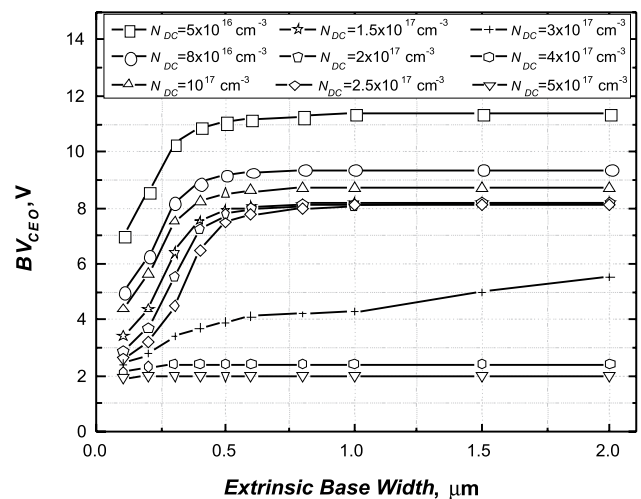
Fig. 4. Dependence of BV_{CEO} on the extrinsic base width (w_{bext}) for different collector concentrations.

a)

b)
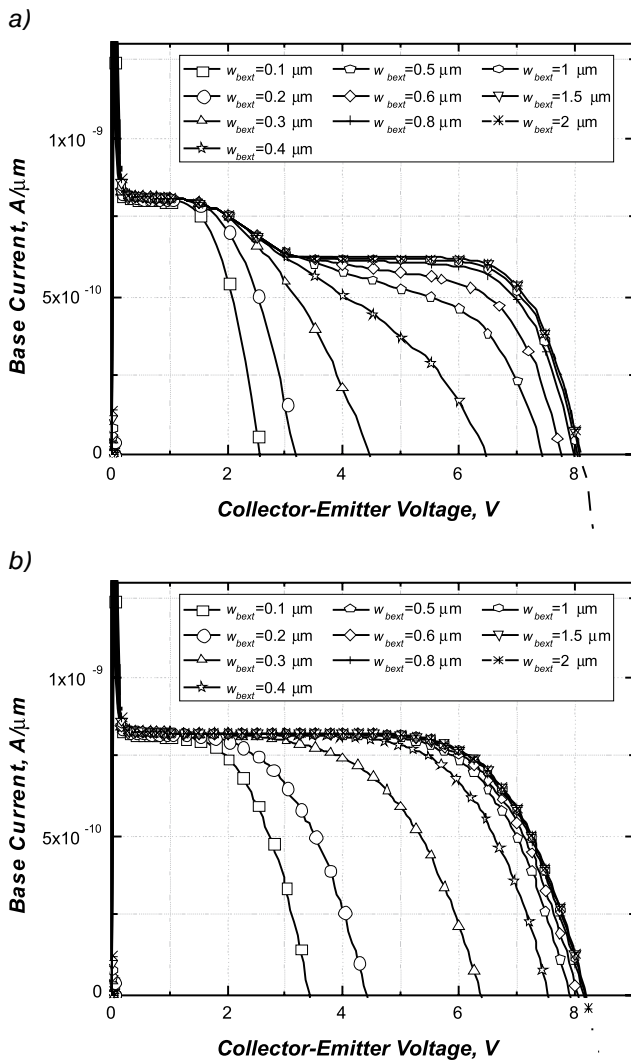
Fig. 5.   Simulation of BV_{CEO} dependence on w_{bext} for:
a) $N_{DC}=2.5\cdot10^{17}$ cm^{-3}, b) $N_{DC}=1.5\cdot10^{17}$ cm^{-3}.

cannot be improved by extending w_{bext}. BV_{CEO} simulations for collector concentrations of $2.5\cdot10^{17}$ and $1.5\cdot10^{17}$ cm^{-3} are shown in Fig. 5.a and 5.b, respectively. For collector concentration of $2.5\cdot10^{17}$ cm^{-3} a plateau in the base current is observed for transistors with wider extrinsic base. These characteristics indicate that electric field has two peak values in the base-collector depletion region. The first peak appears at the intrinsic base-collector junction and approaches the value of the critical electric field at V_{CE} around 3 V. Weak avalanche starts and generated holes drift to the base side reducing the base current. However, peak electric field at the intrinsic base-collector junction is not increased for V_{CE} larger than 3 V and impact ionization is limited as indicated by the plateau in the characteristics for voltages between 3 and 7 V. This is explained by the full depletion of the collector region and the extrinsic base shielding effect. Impact ionization rate in the transistor for V_{CE} of 3 and 9 V is shown in Fig. 6.a and 6.b, respectively. For $V_{CE}=3$ V, just before full depletion of the collector, maximum impact ionization rate occurs at the intrinsic base-collector junction. When V_{CE} is further increased up to 9 V, another region with high impact ionization rate appears
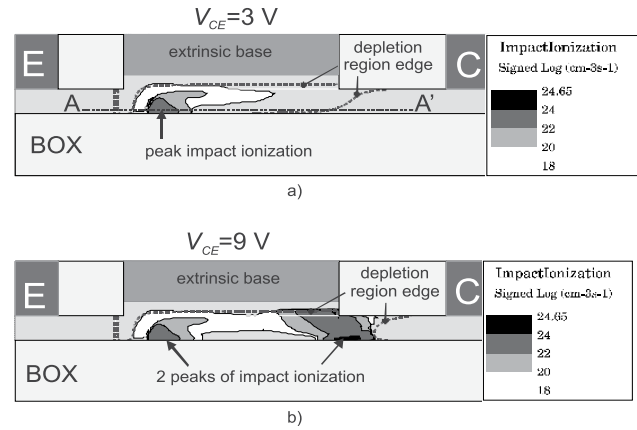
Fig. 6.   Impact ionization rate for structure with $N_{DC}=2.5\cdot10^{17}$ cm^{-3} at $V_{BE}=0.7$ V and a) $V_{CE}=3$ V, b) $V_{CE}=9$ V.

in the drift region to the right side of the extrinsic base. Maximum rate occurs in the bottom part near the buried oxide interface since electrons are pushed down by the vertical component of field and current is crowded near the buried oxide interface. Since the holes generated by impact ionization drift to the base side and are injected to the emitter, a positive feedback of electrons due to transistor's current gain (β) occurs and causes BV_{CEO} to be 2 to 3 times lower than BV_{CBO}. Moreover, for BV_{CEO} to occur the critical electric field has to appear along the current path since the avalanche multiplication process is initiated by mobile electrons. Simulated distribution of electric potential, field and impact ionization rate for different V_{CE} in the plane AA' from Fig. 6. are shown in Fig. 7.a-c. From the potential distribution in Fig. 7.a it can be observed that collector is not fully depleted for V_{CE} below 3 V. Potential is constant across neutral collector region below extrinsic base and electric field is zero. Potential drop appears across depletion region and peak electric field is placed at the intrinsic base-collector junction (Fig. 7.b). For V_{CE} of 4 V and above, the collector under the extrinsic base is fully depleted. Characteristics of potential distribution bends and deviates from standard square function in the area below the extrinsic base and electric field magnitude in that area is reduced. Furthermore, the potential drop across the intrinsic-base-collector junction practically doesn't increase with V_{CE} and the peak of the electric field at intrinsic base-collector junction is constant (Fig. 7.b). Since the collector charge under the extrinsic base is completely shared, there is no available charge to support increase of potential and electric field across the intrinsic base-collector junction. The rest of the potential drop appears across the drift-region on the right side with respect to the extrinsic base-collector junction. Electric field vectors for transistors with w_{bext} of 0.5 μm and 1 μm are shown in Fig. 8.a and 8.b, respectively. Direction of the vectors indicates the direction of the electric field, whereas length of the vectors is proportional to the magnitude of the electric field, i.e. density of the electric field lines in given points of the structure. In case of $w_{bext}=0.5$ μm, a part of the field lines terminated on the intrinsic base acceptors are originated from donors in the

a)

b)

b)
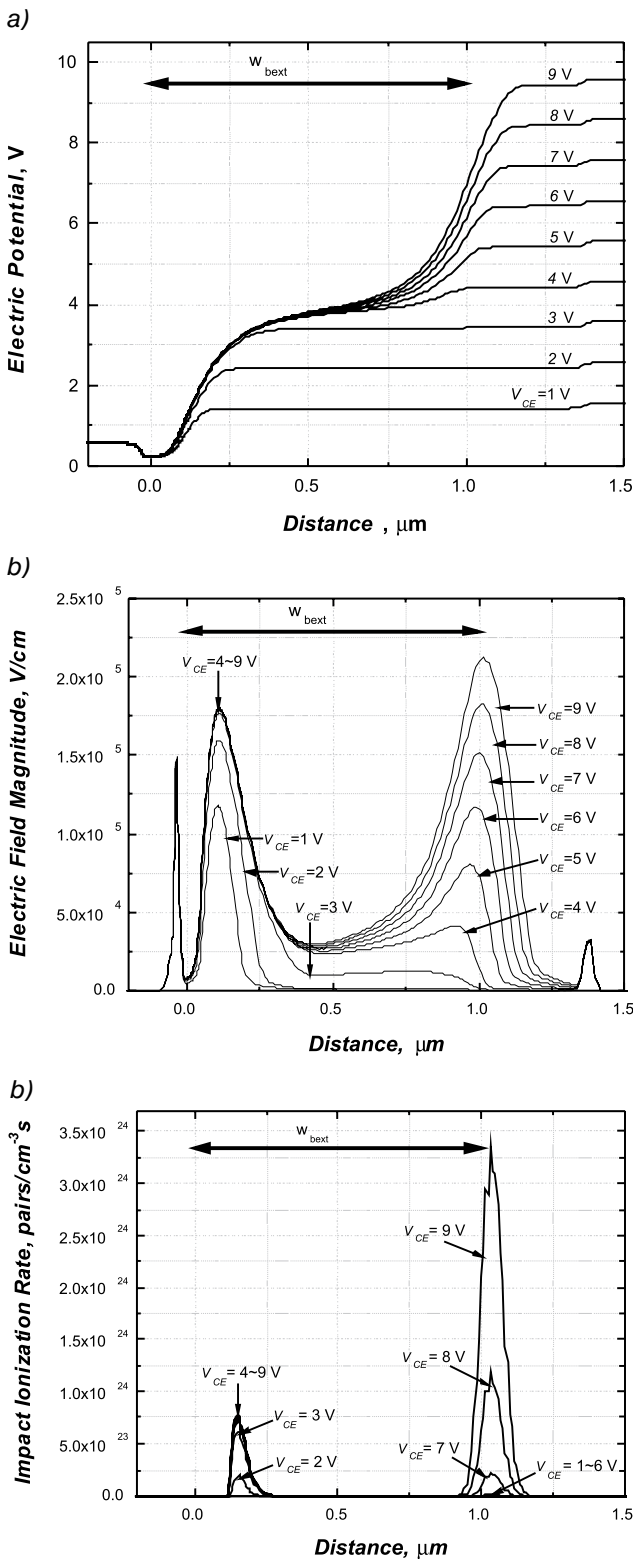
Fig. 7. *Distribution of: a) electric potential, b) electric field, c) impact ionization rate dependence on V_{CE} in the bottom part of the transistor, in the plane marked AA' in Fig.6. 15 nm from the buried oxide. Extrinsic base is located between 0 and 1 μm.*

(a)

(b)
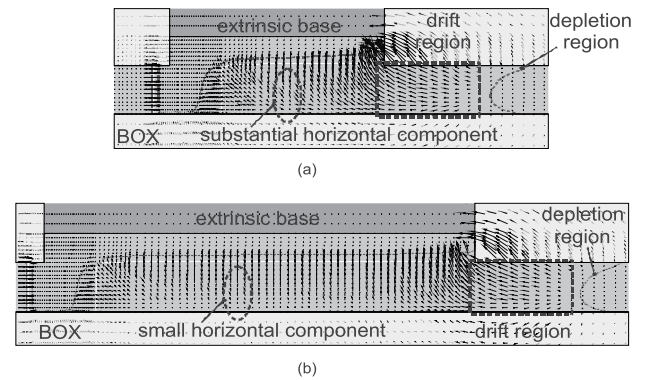
Fig. 8. *Electric field lines at V_{CE}=8 V for structures with a) w_{bext}=0.5 μm and b) w_{bext}=1 μm*

at the intrinsic junction can be increased with V_{CE} but at a slower rate. Shielding is more efficient for larger w_{bext} and the current generated by impact ionization is smaller, which can be observed as a smaller reduction of the base current in Fig. 5.a and the appearance of the plateau in the characteristics. For w_{bext}=1 μm, intrinsic base electric field, which has only horizontal component is completely terminated between donors below the extrinsic base and the intrinsic base acceptors, which is observed as a shorter horizontal arrows in Fig. 8b. Therefore, horizontal electric field is effectively shielded by the extrinsic base vertical field and cannot be further increased with V_{CE}. Density of electric field lines that are terminated on the extrinsic base acceptors is increased in the area next to the drift region, since there is more available donor charge in the area toward extrinsic collector. Field lines originated from donors in the drift region are spread laterally through the drift region and then bent upwards and terminated on the extrinsic base acceptors. Electric field associated with the extrinsic base-collector junction has vertical and horizontal component. The result of this effect is that the second peak of the electric field appears in the drift region as it can be observed in Fig. 7.b. For larger w_{bext}, if V_{CE} is further increased, critical field is exceeded in the drift region and transistor breakdown occurs. From the impact ionization rate shown in Fig. 7.c it can be seen that two regions of the high impact ionization rate associated with two peaks of the electric field, appear in the transistor. The first one is at the intrinsic base-collector junction, which does not increase substantially for voltages above 3 V, whereas the second is placed in the drift region and increases rapidly for V_{CE} above 7 V. These observations are in a good agreement with the characteristics shown in Fig. 5.a. In the case of the characteristics in Fig. 5.b for collector concentration of 1.5·10^{17} cm^{-3} the peak of the electric field at the intrinsic base-collector junction does not approach the critical value and no substantial impact ionization occurs in this region. Critical electric field is achieved in the drift region only and no plateau in the characteristics in Fig. 5.b is observed.

Influence of the collector concentration on the cutoff frequency (f_T) is simulated as well and the results are shown in Fig. 9. As expected, f_T is increased for higher collector concentrations. This is attributed to the narrower intrinsic

drift region, which can be observed as a longer horizontal arrows in Fig. 8a. Therefore, horizontal electric field is only partially shielded by the vertical field and the peak value
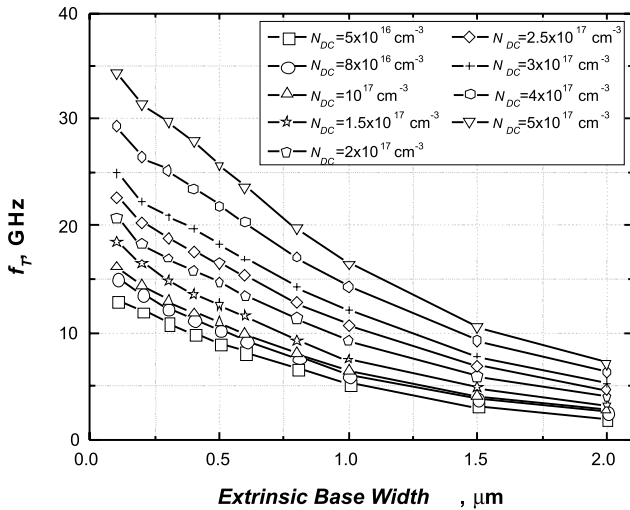
Fig. 9. *Dependence of the cutoff frequency (f_T) on extrinsic base width (w_{bext}) for different collector concentrations.*

base and the shorter base transit time. In addition, Kirk effect is pushed to higher current densities. It is also observed that f_T decreases for larger w_{bext}. This can be explained by the influence of the vertical electric field on the current flow under the extrinsic base. Electrons flowing through the base-collector depletion region are pushed down by the vertical electric field toward buried oxide and local current density is increased causing the Kirk effect to appear at lower values of the collector current. Furthermore, in the case of fully depleted collector, electrons have to travel through the wider depletion region, which results in a longer transit time. Both effects reduce cutoff frequency.

Influence of the distance between n^+ extrinsic collector and the p^+ extrinsic base is also investigated. BV_{CEO} dependence on w_{bext} is shown in Fig. 10. It can be seen that BV_{CEO} can be increased for larger w_{bext}. However, BV_{CEO} saturates at smaller value if the distance between collector contact and extrinsic base (d_c) is reduced. This is explained by
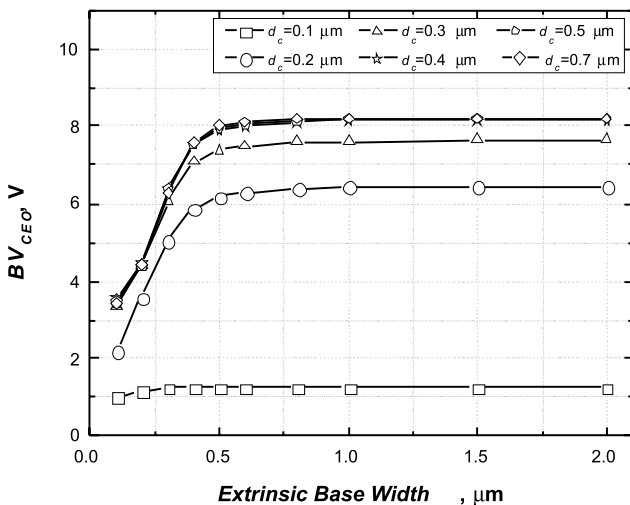
Fig. 10. *Dependence of BV_{CEO} on w_{bext} for different distances between n^+ collector and p^+ extrinsic base (d_c).*

the reduced depletion region width if n^+ region is brought closer to the p^+ extrinsic base. Electric field is increased in the drift region and breakdown occurs at lower collector-emitter voltages. It can also be observed that the increase of BV_{CEO} with d_c saturates at d_c=0.4 μm. Obviously, for larger values of d_c, the base-collector depletion region does not reach n^+ extrinsic collector and does not cause an increase of the electric field in the drift region. Influence of d_c on cutoff frequency is also investigated. However, less than 5% improvement in f_T can be achieved by bringing the n^+ collector contact region closer to the extrinsic base.

3.2. Emitter height dependence

Dependence of the BV_{CEO} and f_T on the emitter height (h_E) is investigated next. Link base length (l_b) of 70 nm and collector concentration of 1.5·10^{17} cm^{-3} are kept constant in the simulations. Intrinsic transistor profile from Fig. 2 is used in simulations. In the real process, h_E would be determined by the thickness of the silicon on insulator film. Dependence of BV_{CEO} on h_E with w_{bext} as a parameter is shown in Fig. 11. It can be observed that BV_{CEO} is increased with h_E as long as collector is fully depleted for collector-emitter voltage that is lower than the breakdown voltage. Since the extrinsic base shielding effect is stronger for larger w_{bext}, BV_{CEO} has the tendency of rise even for larger values of h_E. For larger w_{bext}, electric field lines of the horizontal component of field are completely terminated between intrinsic base acceptors and donors below extrinsic base and there is no penetration of the horizontal field associated with intrinsic base-collector junction all the way to the drift region. Magnitude of the electric field for structures with h_E of 0.2 μm and w_{bext} of 1 μm and 0.5 μm are presented in Fig. 12.a and 12.b, respectively. It can be seen that for structure with w_{bext}=1 μm peak electric field at the intrinsic base-collector junction rises for V_{CE} voltages up to 5 V and after that it is practically constant. Horizontal field is shielded by the extrinsic base vertical field completely. If V_{CE} is increased further, the second peak of the electric field appears in the drift region and causes the transistor breakdown to occur when critical field is reached. For structure with w_{bext}=0.5 μm,
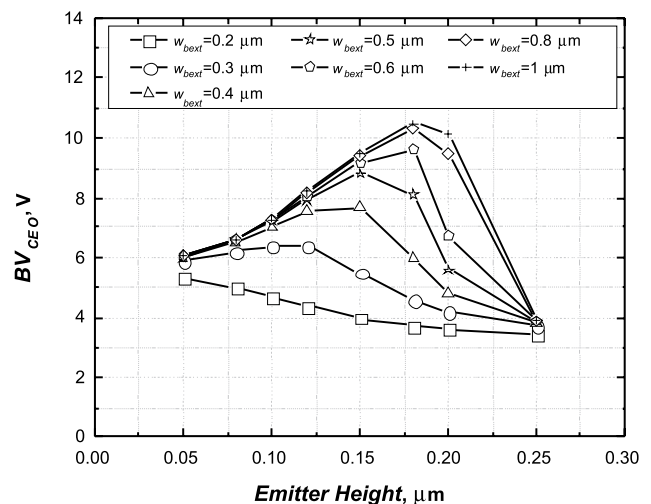
Fig. 11. *Dependence of BV_{CEO} on h_E for different w_{bext}.*

a)

b)
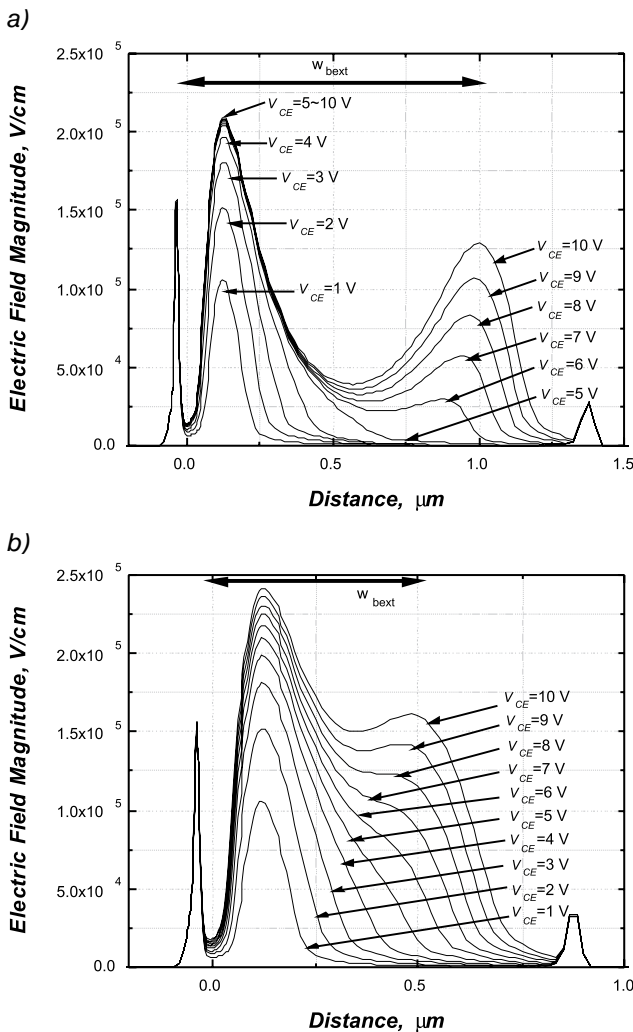
Fig. 12. Electric field in the transistor 15 nm from buried oxide for structure with N_{DC}=1.5·10^{17} cm^{-3}, h_E=0.2 μm and a) w_{bext}=1 μm, b) w_{bext}=0.5 μm.

the extrinsic base shielding is not complete. Peak electric field at the intrinsic base-collector junction increases even for voltages greater than 5 V and can reach the critical value for transistor breakdown. Since part of the electric field lines originated from donors in the drift region to the right side of the extrinsic base are terminated at extrinsic base acceptors, there are more available donor charge below extrinsic base which can support horizontal electric field over the intrinsic base-collector junction. Horizontal field penetrates toward the drift region and the peak at the intrinsic base-collector junction is increased. Avalanche multiplication and transistor breakdown occur at the intrinsic base-collector junction.

In addition, for larger w_{bext} current flows over a longer distance under the influence of vertical electric field and is pushed down to the buried oxide interface. Therefore, current flows through the part of the drift region where magnitude of the electric field is smaller compared to the upper part, closer to the p^+ extrinsic base region, resulting in a lower impact ionization rate.
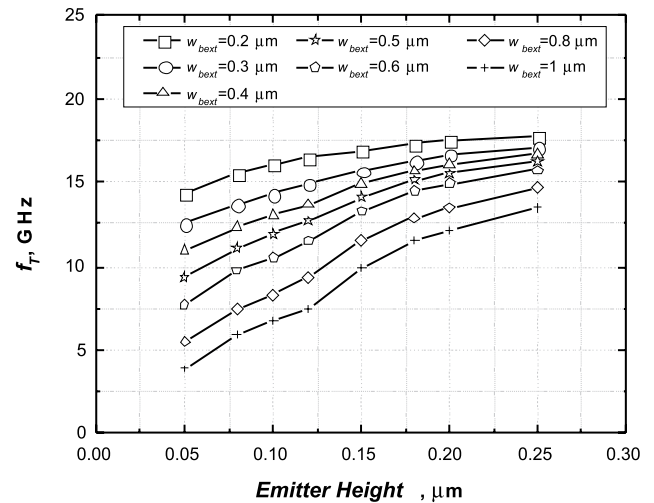
Fig. 13. Dependence of f_T on h_E for different w_{bext}.

As h_E is reduced, the amount of the available donor charge under the extrinsic base is reduced and voltage drop associated with vertical electric field is smaller. Therefore, a larger voltage drop appears laterally across the drift region and critical electric field for avalanche multiplication in the drift region is reached at lower V_{CE}, causing the decrease in BV_{CEO}. For the largest values of h_E, BV_{CEO} decreases since collector is not fully depleted any more.

Simulation results of f_T dependence on h_E for different w_{bext} is presented in Fig. 13. For larger h_E, f_T is increased. As h_E is increased, cross-section of the neutral collector is increased and current crowding due to vertical field influence is less pronounced. Kirk effect is pushed to higher collector currents as local current density is reduced and f_T is increased. The current crowding effects are more pronounced for structures with larger w_{bext} which can be observed as a smaller value of f_T in Fig. 13. In addition, electrons are traveling through the wider depletion region increasing the associated transit time. For w_{bext} larger than 0.5 μm the transit time through the depletion region becomes comparable to the base transit time. Furthermore, time constant associated with the collector-base capacitance and the collector resistance i.e. $R_C C_{BC}$ is increased for larger w_{bext}, which further reduces f_T.

3.3. Link-base length dependence

Influence of the link-base length (l_b) on BV_{CEO} and f_T is also investigated. Emitter height (h_E) is kept constant at 120 nm and collector concentration is set to 1.5·10^{17} cm^{-3}. By increasing l_b, thickness of the n-collector under the extrinsic base is increased and a higher collector-emitter voltage is needed to reach full depletion of the collector region. Simulation results for BV_{CEO} dependence on l_b with w_{bext} as a parameter are shown in Fig. 14. For larger w_{bext}, shielding by the extrinsic base field is more efficient and higher BV_{CEO} values are observed. This dependence is similar to the dependence on h_E, since in both cases the amount of collector charge is changed by the variation in the thickness of the n-collector below the extrinsic base. Results of
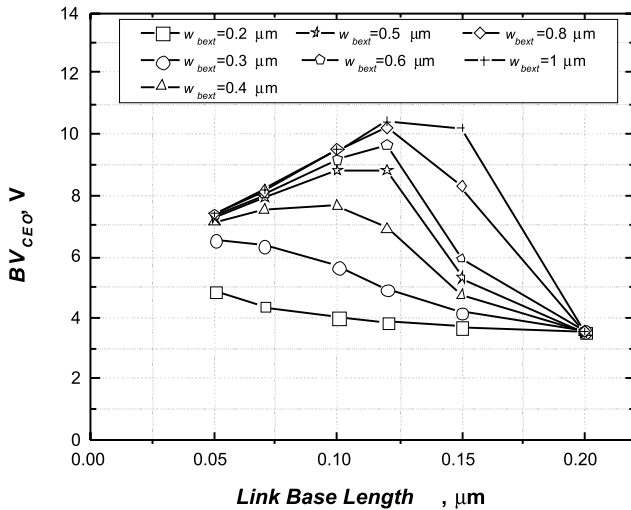
Fig. 14. Dependence of BV_{CEO} on link-base length (l_b) for different w_{bext}.

f_T dependence on l_b are presented in Fig. 15. showing the similar behavior as dependence on h_E. Current crowding effects are relaxed by increasing the link-base length and f_T is improved. Degradation of f_T by current crowding is more severe in the case of larger w_{bext} as seen from Fig. 15.

4. Conclusions

LBT structure with the base contact on top is analyzed by the device simulations. Influence of the extrinsic base width (w_{bext}) on common-emitter breakdown voltage (BV_{CEO}) and cutoff frequency (f_T) is examined in detail. The effect of collector charge sharing can be used to obtain structures with different values of BV_{CEO} and f_T. Total amount of collector charge is determined by the collector concentration and the silicon film thickness, which can be controlled to achieve full depletion of the collector region. In case of fully depleted collector, two peaks of the electric field appear along the current path in the base-collector depletion region. The first one is at the intrinsic-base collector junction and the
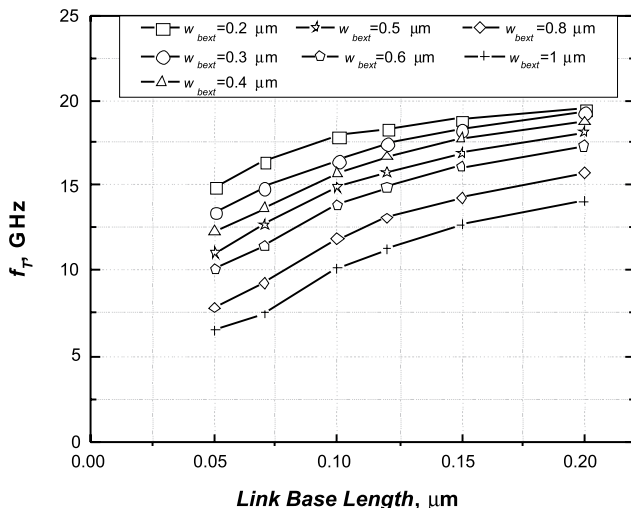
second one in the drift region toward extrinsic collector. Extrinsic base shielding effect can be used to control the value of the peak electric field at the intrinsic-base collector junction. For smaller w_{bext}, the horizontal field associated with the intrinsic base junction is partially shielded and the peak electric field increases with V_{CE}. In case of larger w_{bext}, shielding is more effective; the peak electric field increases at slower rate with V_{CE} and approaches the critical value for avalanche multiplication at higher V_{CE}. In both cases avalanche occurs at the intrinsic-base collector junction but BV_{CEO} is increased for larger w_{bext} due to smaller increase of the peak electric field with V_{CE}. For very large w_{bext}, horizontal field is completely shielded by the vertical field and the peak electric field at the intrinsic base junction does not increase with V_{CE}. However, the second peak in the drift region increases with V_{CE} and can reach the critical value for avalanche multiplication. Transistor breakdown occurs in the drift region for transistors with larger w_{bext}. It is shown that BV_{CEO} engineering can be achieved for w_{bext} below 0.8 μm. Tradeoff between breakdown (BV_{CEO}) and transistor's cutoff frequency (f_T) is presented and design guidelines regarding collector concentration and transistor geometry is given. The potential of BV_{CEO} engineering for top contacted SOI LBT structure without additional increase in cost of technology is demonstrated.

References

/1/ K. Cheng, A. Khakifirooz, P. Kulkarni, S. Ponoth, J. Kuss, D. Shahrjerdi, L. F. Edge, A. Kimball, S. Kanakasabapathy, K. Xiu, S. Schmitz, A. Reznicek, T. Adam, H. He, N. Loubet, S. Holmes, S. Mehta, D. Yang, A. Upham, S.-C. Seo, J. L. Herman, R. Johnson, Y. Zhu, P. Jamison, B. S. Haran, Z. Zhu, L. H. Vanamurth, S. Fan, D. Horak, H. Bu, P. J. Oldiges, D. K. Sadana, P. Kozlowski, D. McHerron, J. O'Neill, B. Doris, "Extremely Thin SOI (ETSOI) CMOS with Record Low Variability for Low Power System-on-Chip Applications", *IEDM Tech. Dig.,* 2009, pp. 49-52

/2/ H. Nii, T. Yamada, K. Inoh, T. Shino, S. Kawanaka, M. Yoshimi, Y. Katsumata, "A Novel Lateral Bipolar Transistor with 67 GHz f_{max} on Thin-Film SOI for RF Analog Applications", *IEEE Trans. Electron Devices,* Vol. 47, No. 7, pp. 1536–1541, July 2000.

/3/ M. Sun, W. T. Ng, K. Kanekiyo, T. Kobayashi, H. Mochizuki, M. Toita, H. Imai, A. Ishikawa, S. Tamura, K. Takasuka, "Lateral High-Speed Bipolar Transistors on SOI for RF SoC Applications", *IEEE Trans. Electron Devices,* Vol. 52, No. 7, pp. 1376–1383, July 2005.

/4/ J. Cai, M. Kumar, M. Steigerwalt, H. Ho, K. Schonenberg, K. Stein, H. Chen, K. Jenkins, Q. Ouyang, P. Pldiges, and T. Ning, "Vertical SiGe-base bipolar transistors on CMOS-compatible SOI substrate", Proc. Bipolar/BiCMOS Circuits Technol. Meeting, 2003, pp. 215–218.

/5/ T. Suligoj, M. Koričić, H. Mochizuki, S. Morita, K. Shinomura, and H. Imai, "Horizontal Current Bipolar Transistor (HCBT) with a Single Polysilicon Region for Improved High-Frequency Performance of BiCMOS ICs," IEEE Electron Device Lett., in press.

/6/ S. A. Parke, C. Hu, P. K. Ko, "A High-Performance Lateral Bipolar Transistor Fabricated on SIMOX", *IEEE Electron Device Letters*, Vol. 14, No. 1, pp 33-35, January 1993.

/7/ T. Shino, K. Inoh, T. Yamada, H. Nii, S. Kawanaka, T. Fuse, M. Yoshimi, Y. Katsumata, S. Watanabe, J. Matsunaga, "A 31 GHz fmax Lateral BJT on SOI Using Self-Aligned External Base Formation Technology", *IEDM Tech. Dig.*, 1998, pp 953-956.

/8/ „ „R. Dekker, W.T.A. v.d. Einden, H.G.R. Maas, "An Ultra Low Power Lateral Bipolar Polysilicon Emitter Technology on SOI", *IEDM Tech. Dig.*, 1993, pp 75-78.

Fig. 15. Dependence of f_T on link-base length (l_b) for different w_{bext}.

/9/ G. G. Shahidi, D. D. Tang, B. Davari, Y. Taur, P. McFarland, K. Jenkins,D. Danner, M. Rodriguez, A. Megdanis, E. Petrillo, M. Polcari, and T. H. Ning, "A novel high-performance lateral bipolar on SOI", *IEDM Tech. Dig.,* 1991 pp. 663-666.

/10/ W. L. M. Huang, K. M. Klein, M. Grimaldi, M. Racanelli, S. Ramaswami, J. Tsao, J. Foerstner, B. C. Hwang, "TFSOI Complementary BiCMOS Technology for Low Power Applications", *IEEE Trans. Electron Devices,* Vol. 42, No. 3, pp. 506–512, March 1995.

/11/ J. M. Stork, R. D. Isaac "Tunneling in Base-Emitter Junctions", *IEEE Trans. Electron Devices,* Vol. 30, No. 11, pp. 1527–1534, July. 1983.

/12/ E. O. Johnson, "Physical limitations on frequency and power parameters of transistors," *RCA Rev.*, Vol. 26, pp. 163-177, 1965.

/13/ J. D. Cressler, G. Niu, *Silicon-germanium Heterojunction Bipolar Transistors*, Artech House,2003.

/14/ C.Jungemann, R.Thoma and W.L.Engl, "A Soft Threshold Lucky Electron Model for Efficient and Accurate Numerical Device Simulation," Solid-State Electronics, Vol. 39, No. 7, pp.1079-1086, 1996.

Marko Koričić[*], Tomislav Suligoj
Department of Electronics, Microelectronics, Computing and Intelligent Systems, Faculty of Electrical Engineering and Computing, University of Zagreb, Unska 3, HR-10000 Zagreb, Croatia

[*] Corresponding author.
Tel.: +385-1-6129671, fax.: +385-1-6129653, e-mail address: marko.koricic@ fer.hr

STRUCTURING SOFT-MAGNETIC COMPOSITE MATERIALS

M.V.Zagirnyak[1], V.V.Prus[1], V.P.Lyashenko[1], D. Miljavec[2]

[1]Kremenchuk Ostrogradskiy State Polytechnic University,Kremenchuk,Ukraine
[2]University of Ljubljana, Faculty of electrical engineering, Slovenia

Key words: Powder metallurgy, Soft-magnetic composites, hysteresis losses, eddy current losses, iron losses

Abstract: The aim of the proposed paper is to present different procedures for preparation the mixture of soft-magnetic powder material and to show the influence of different manufacturing processes for achieving particular structures and properties of soft magnetic composite (SMC) material. The technique of SMC production with improved mechanical properties and the necessary electrical and magnetic parameters by means of powder metallurgy methods are described. A novel laminated powder structure of SMC material is developed. The content of the paper gives useful hints for specialists dealing with creation and research of new magnetic materials and magnetic systems for electric machines and power electronics.

Strukturiranje mehkomagnetnega kompozitnega materiala

Kjučne besede: Metalurgija prahov, mehko-magnetni kompozitni material, histerezne izgube, vrtinčne izgube, izgube v železu

Izvleček: V članku so predstavljeni različni načini priprave mešanice mehkomagnetnih prahov z dodatki in vplivi različnih tehnoloških postopkov izdelave na končne lastnosti mehkomagnetnih kompozitnih (MMK) materialov. Predstavljen je merilni sistem, ki omogoča določanje magnetnih lastnosti MMK materiala. Opisane so tudi lastnosti nove lamelirane strukture MMK materiala. Vsebina članka podaja koristne napotke specialistom, ki se ukvarjajo z ustvarjanjem in raziskovanjem novih magnetnih materialov ter elektromagnetnih sklopov za elektične stroje in močnostno elektroniko.

1. Introduction

Soft-magnetic composites, i.e. ferromagnetic material in the powder form are mainly made by atomization of Fe-Si compound. The material is mostly used for electric micro and small machine cores /1, 2/ and in power electronic for inductor cores. The powder can be pressed to the required shape and thus forming a magnetic core of desired geometric properties.

The world production of soft-magnetic composites is limited, which results in a relatively high material cost. The price is lower regarding the 0.1 mm laminated steel, but higher as that of 0.5 mm laminated steel, traditionally used in electric machines manufacturing /3-7/.

Existing production techniques ensure the required properties and characteristics of soft-magnetic composite materials due to high quality of expensive primary materials – iron powders and bonding materials, which causes a significant increase of their cost. That is why development of high-quality soft-magnetic materials and decrease of their production cost is a prospective direction of the study /8, 9/.

The objective of this analysis is to improve the method of manufacturing the soft-magnetic composites samples with the required mechanical, electrical and magnetic characteristics. That include magnetic saturation B_s, residual magnetization B_R, coercive force H_c, electric conductivity, iron losses Pm, mechanical strength and compactness. Taking into consideration the range of change of the analyzed parameters, it is necessary that the measuring equipment and methods of processing the measurement results take into account nonlinear properties of the magnetic material.

The measurements must achieve assigned accuracy in a wide range of parameters change, including the condition of high saturation level. In this way the magnetic measurements carried out during researching are different from measurements performed throughout normative testing or during the production monitoring.

2. Preparation and fabrication of soft magnetic composite material

Taking into account the peculiarities of the soft-magnetic material structure, a sequence of the main cycles of manufacturing technique by means of powder metallurgy is summarized:

1. Powder is produced by means of an electrolytic method, which provides high powder dispersion and well-developed dendrite shape of grain particles.

2. Preparation of powders for pressing, which includes their pre-firing at the temperature of 250-350⁰C, formation of a powder sieve structure with preset fractional dimensions, then mixing it with a lubricant and plastic bonding material ensuring maximum electrical isolation between ferromagnetic grains. Powder sieve structure is analogous to the one stated in /10, 11/.

3. Warm pressing under controlled pressure and temperature of 200-450°C, which enables plastic bonding material to cover the grain surface uniformly and to electrically insulate the grains between each other. The process of this stage also influences the formation of the grain structure into final product shape.

In the frame of our research we made some specimens of SMC material in the form of rings. The rings were

prepared for microscopic analysis and some of the results are presented below. Separate grains of different size (10÷20 μm) are visible in Fig. 1. The grains are separated with inclusions layer. The separation blisters are visible, but the additives are not observed. The separate sintered grains (5÷20 μm) and alloyed or sintered grains without a separating interlayer are also shown in Fig. 2.

4. Annealing at temperatures of 1150-1250^{0}C provides formation of the necessary grain structure in the product and ensures the required mechanical, electrical and magnetic properties of the soft-magnetic composite structure.

For each of the mentioned cycles there are only general recommendations due to a wide range of parameters variation and different modes of performing the cycles. The task of our research is to select of all the parameters, beginning with the ones which influence the analyzed characteristics. This mainly refers to the second and fourth cycle. During the preparation for the pressing cycle the research should be focused on iron powder compositions, choice of the plastic bonding material and a lubricant to improve the necessary mechanical properties, as well as electrical and magnetic parameters. In case of high-temperature annealing it is also necessary to exactly measure the specimen temperature and cycle duration.

Further results were obtained by annealing the specimen at the temperature of 220^0 C. The texture of soft magnetic iron-based sample was made in this way. Uniform distribution of plastic bonding material on the grains surface was revealed (Fig. 3) by scanning the sample. The X-ray spectrum analysis of specimen (Fig. 4) shows that the electric isolation layer is spread uniformly across the grain surface. The results are presented in Fig. 4. This insulation layers decrease electric conductivity of the material and reduce induced eddy currents.
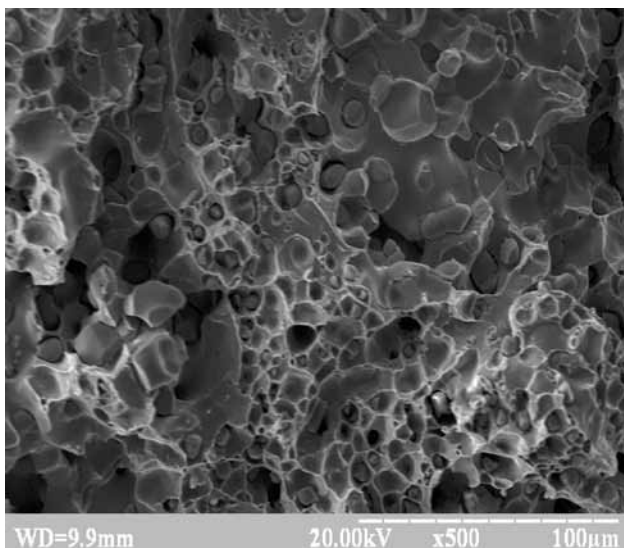
Metallographic analysis was made using NIAPHOT-2 microscope (France). Fracture investigation was made by REM-106I focused beam electronic microscope (Sumy, Ukraine).
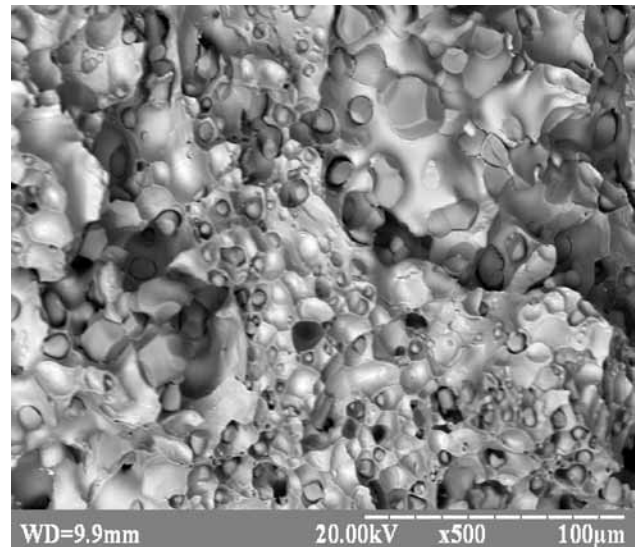
Fig. 2: *The separate sintered grains 5÷20 micrometers and alloyed or sintered grains without separating interlayer.*
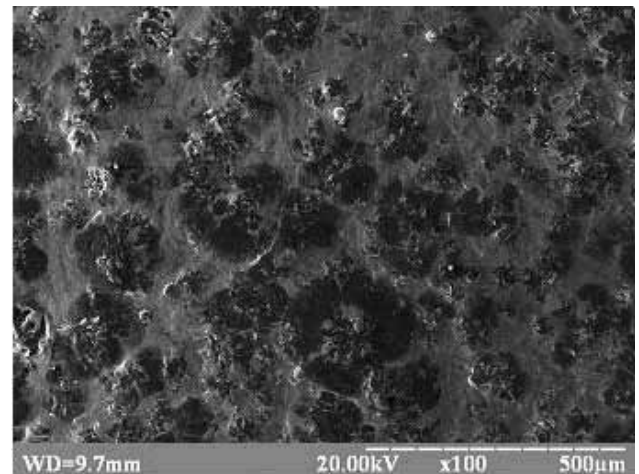
Fig. 3: *Uniform distribution of plastic bonding material on the grains surface*
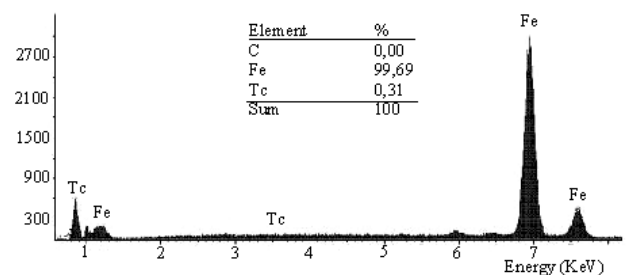
Fig. 4: *The X-ray spectrum analysis of a specimen*

Fig. 1: *Separate grains of different size (10÷20 μm) with inclusions layer*

3 Measuring system

Regarding the requirements of testing equipment /12/, the use of inductive measuring procedure with alternating magnetization of samples with changing amplitude and frequency is the most reasonable one.

The structure of the measuring system (MS) is shown in Fig. 5. A tested sample (TS) represents a closed magnetic system with magnetization and measuring windings. The parameters which characterize the testing system are: current $i_1(t)$, voltages $u_1(t)$ and $u_2(t)$. The signals from TS go to current CT and voltage VT2 transducers. Output signal $u_1(t)$ from off-line sinusoidal voltage source (PS) is connected to the voltage transducer VT1 and to the tested sample.
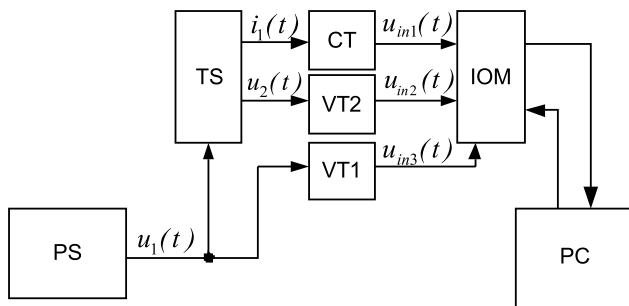
Fig. 5: Block diagram of the measuring system for testing soft-magnetic composite material samples

Signals from the transducers go through input/output module (IOM) to a computer, whose functions are data gathering, storage and processing. The offered MS uses certified testing module E14-440D (L-Card, Russia) as an IOM. Measuring software is realized in software environment Lab View 8.2 with the aim to achieve the reconfiguration flexibility and visualization of measurement process.

Due to magnetization of soft-magnetic material in alternating magnetic fields the determination of the magnetic flux density $B(t)$ and the magnetic field strength $H(t)$ frequency spectrum from the linear section of magnetization up to the saturation level is required. Also, the conditions of frequency spectrum decomposition and further composition have to be formulated.

Taking into consideration the above described peculiarities of the test, the determination of all the parameters was established on the base of preliminary decomposition of the measured signals applying Fourier transform. The results are used to compute the necessary parameters, such as magnetic flux density, magnetic field strength, hysteresis losses and eddy current losses.

The amplitude of magnetic flux density is calculated by:

$$B_m = \frac{\sqrt{2}}{2\pi} \frac{U_2}{f N_{ms} S_c}, \qquad (1)$$

where U_2 is the effective value of measuring winding voltage; N_{ms} – number of measuring winding turns; S_c – mag-

netic circuit core cross-section area; f – magnetization frequency.

Magnetic field strength is computed by:

$$H = I_1 N_{mg}/l \qquad (2)$$

where I_1 is the effective value of current in magnetizing winding, N_{mg} is the number of magnetizing winding turns and l is the average length of magnetic circuit.

If $B(t)$ and $H(t)$ are not sinusoidal at a linear section of magnetization curve, the computation is carried out only on the basis of the first harmonic components. Total harmonic distortion of signals is estimated with the help of current $i_1(t)$ and voltage $u_2(t)$ harmonic factor:

$$k_h = \sqrt{\sum_{p=2}^{k} A_p^2} \bigg/ A_1, \qquad (3)$$

where p is the higher harmonic number, k is the number of the considered harmonics, A_1 and A_2 are, correspondingly, effective values of the first and p-th order harmonics in signal.

Losses in magnetic material are derived by

$$P_{q\mu p} = \frac{N_{mg}}{N_{ms}} (a_{i1p} a_{u2p} + b_{i1p} b_{u2p})/4, \qquad (4)$$

Where a_{i1p}, b_{i1p}, a_{u2p} and b_{u2p} are, correspondingly, current $i_1(t)$ and voltage $u_2(t)$ signals squared components.

After processing the measured values $i_1(t)$ and $u_2(t)$ a dynamic hysteresis loop is created. Instantaneous value of the magnetic field strength is found from the relation

$$H(t) = i_1(t) N_{mg}/l. \qquad (5)$$

Instantaneous value of the magnetic flux density $B(t)$ is determined by using voltage signal $u_2(t)$ by

$$B(t) = \frac{1}{N_{ms} S_C} \sum_p \frac{U_{2mp}}{p\omega} \cos(p\omega t + \varphi_p), \qquad (6)$$

Where $\omega = 2\pi f$ is signal of the first harmonic angular frequency, U_{2mp} and φ_p are, correspondingly, voltage $u_2(t)$ of the harmonic components amplitude and of the initial phase obtained from the expansion into a Fourier series.

A possibility to determine the relationships between magnetic losses measured at different frequencies was investigated, the aim of which was to separate them into hysteresis and eddy current losses at a constant magnetic flux. In this case the voltage amplitude must change proportionally to its frequency

$$\frac{U}{f} = const, \qquad (7)$$

Where U, f are the amplitude and frequency of the supply voltage.

The values of hysteresis and eddy current losses components are expressed by relation:

$$P_\mu = P_{\mu h} + P_{\mu ec} = C_h f + C_{ec} f^2, \qquad (8)$$

Where P_μ, $P_{\mu h}$ and $P_{\mu ec}$ are total magnetic losses, hysteresis and eddy current losses, accordingly; C_h and C_{ec} are the corresponding coefficients.

Specific hysteresis and eddy current losses are found from coefficients C_h and C_{ec} in accordance with the relations:

$$p_{\mu h1,0/50} = \frac{50 C_h}{m \left(\dfrac{B_m}{1,0} \right)^2} \qquad (9)$$

and

$$p_{\mu ec1,0/50} = \frac{2500 C_{ec}}{m \left(\dfrac{B_m}{1,0} \right)^2}, \qquad (10)$$

where $p_{\mu h1,0/50}$ and $p_{\mu ec1,0/50}$ are specific hysteresis and eddy current losses at the values of magnetic induction of 1T and frequency of 50 Hz, B_m is magnetic induction for which coefficients C_h and C_{ec} were found and m is a mass of the tested sample.

Then, by means of solving the equation system

$$\begin{cases} p_{\mu h1,0/50} + p_{\mu ec1,0/50} = p_{\mu 1,0/50} \\ p_{\mu h1,0/50}\left(\dfrac{f}{50}\right) + p_{\mu ec1,0/50}\left(\dfrac{f}{50}\right)^2 = p_{\mu 1,0/50}\left(\dfrac{f}{50}\right)^\alpha \end{cases} \qquad (11)$$

when there are two arbitrary similar values of frequency, the values of specific magnetic losses $p_{\mu 1,0/50}$ at magnetic flux density of 1 T, frequency of 50 Hz and at coefficient a are defined. These results are used to define the value of total magnetic losses for the developed SMC structure in the function of magnetic flux density and frequency.

4. Production and analysis of experimental smc samples

In our research, the sample produced from Hoganas (Sweden) soft magnetic powder material Somaloy 700 served as a reference. This material has one of the best electrical and magnetic properties at present.

During the research process it was taken into consideration that all the mentioned properties are achieved when the composite compactness is increased and also when the additives are added to the iron powder to improve the

desired properties. It means that powder can be pressed into a high-density composite, which is easily taken out of a press tool and preserves good quality of the surface.

The powder was finished in the form of electrically isolated particles forming soft-magnetic material. Fatty acid amides, colophony and lump rubber were used as electrical insulators. Besides, a phosphorous containing insulating layer was also made.

Many samples of SMC rings, with parameters given in Table 1, were made by various methods. Sample No.1 was made from Hoganes (Sweden) material, sample No. 2 is a laminated structure (magnetically oriented powder) with plastic bonding material based on lump rubber with annealing parameters $T_2 = 1150^0$ C and $t_2 = 0,5$ h, sample No. 3 is an isotropic structure with plastic bonding material based on colophony with annealing parameters $T_3 = 900^0$ C and $t_3 = 2$ h, samples No. 4-5 are made as isotropic structures with plastic bonding material based on lump rubber with annealing parameters $T_4 = 1100^0$ C, $t_4 = 1$ h and $T_5 = 1150^0$ C, $t_5 = 0,5$ h.

Analyzed properties are given in Table 2. Figures 6 – 10 show a family of hysteresis loops for produced samples. The excitation frequency was 50 Hz. Fig. 11 demonstrates the dependence of iron losses in the function of magnetic flux density at this frequency.

Table 1: Parameters of the samples

Param.	Samp. No. 1	Samp. No. 2	Samp. No. 3	Samp. No. 4	Samp. No. 5
Outer diameter /cm	5,5	2	2,14	2,1	2,1
Inner diameter /cm	4,5	1,45	1,5	1,5	01,5
Height /cm	0,98	0,17	0,27	0,33	0,29
Mass /g	60	2	3	3	3
N_{mg}	85	65	65	65	65
N_{ms}	100	60	100	100	100
R_{mg} /Ω	1,6*	0,15	–	0,16	0,17
R_{ms} /Ω	3,5*	1,54	–	3,18	3,05

* Resistance was measured by *U-I* method, in other cases by measuring bridge.

Table 2: Results of magnetic and electrical parameters for analyzed samples

Param.	Samp. No. 1	Samp. No. 2	Samp. No. 3	Samp. No. 4	Samp. No. 5
Residual magnetization /T	0,18	0,39	0,22	0,19	0,18
Coercive force /(A/m)	153	379	668	574	553
Saturation point B/H /(T/A/m)	0,42/756	0,62/795	0,31/1160	0,22/735	0,24/1075
Specific iron losses B_m=0,4T, *f*=50Hz* /(W/kg)	0,45	0,66	3,74	≈5,5	≈3,8

*For a number of samples there was not possible to determine iron losses at magnetic flux density 1T, because it was physically impossible to reach required level (sample get magnetically saturated before 1T).
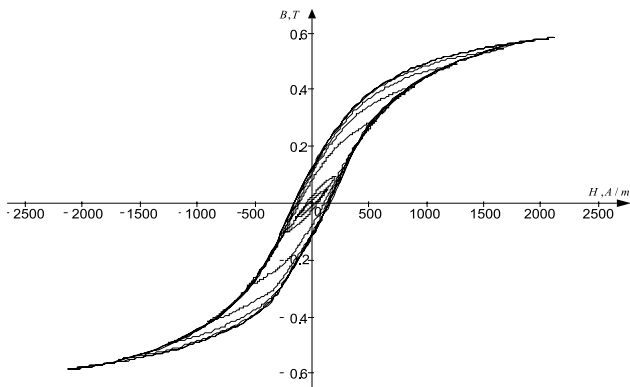
Fig. 6:   *Family of hysteresis loops* for a sample made from Hoganes powder material

Fig. 7:   *Hysteresis loops for sample No. 2*

Fig. 8:   *Hysteresis loops for sample No. 3*

Fig. 9:   *Hysteresis loops for sample No. 4*

Fig. 10: *Hysteresis loops for sample No. 5*

Fig. 11: *Iron losses curves $p\mu = f(B_m)$ for the analysed samples*
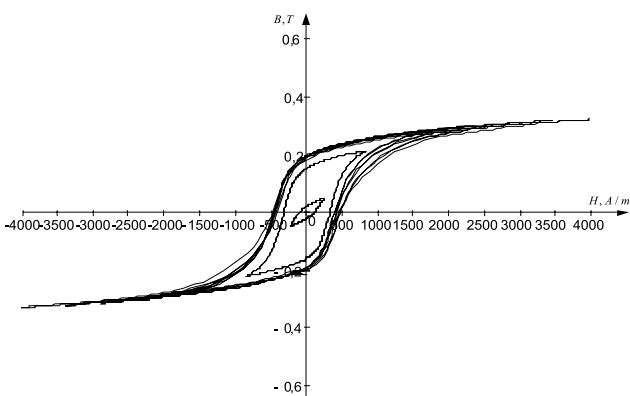
The results show that the nearest sample to the one made from the Hoganas company material is the sample No. 2 presenting a laminated powder structure. This structure is very promising for further research related to material structure improvement and to optimization of manufacturing process.

Comparison of the gained results with the known data for the used material show that the error of the parameters measurement is within the permissible limits. Hence, the developed measuring system can be used to determine the properties of soft-magnetic composite materials.

5.   Conclusions

The procedure of preparing the mixture of soft-magnetic composite material was presented. The influence of different manufacturing processes in achieving particular structures and properties of SMC material was explained. Different samples were prepared and analyzed during the research. The sample produced from Hoganas ferromagnetic powder material served as a reference from the point of mechanical, electrical and magnetic characteristics. A measuring system was developed, which enables to analyze magnetic properties of developed SMC material. The system allows to measure hysteresis loops and iron losses at different excitation levels and frequencies. The results show that the sample No. 2 presenting a novel laminated

powder structure has properties similar to the reference one. Further research will be based on the laminated powder structures as most prospective from the point of view of obtaining the required mechanical, electrical and magnetic characteristics within the focus of material cost reduction.

References

/1/ H. Kuhn, B. Ferguson: Powder forging. MPIF, Princeton, NJ, 1990.

/2/ M. Zagirnyak & all: Proceeding of 2000 PM2TEC International Conference, May 30 – June 3, 2000, New York, USA.

/3/ D. Miljavec, B. Zidarič, M. Zagirnyak, "Soft magnetic composite in design of BLDC motor", 16th International conference on electrical machines, Conference proceedings. /Cracow/: ICEM, 2004.

/4/ G. Štumberger, M. Hadziselimovic, B. Štumberger, D. Miljavec, D. Dolinar, I. Zagradišnik, "Comparison of capabilities of reluctance synchronous motor and induction motor", J. magn. magn. mater.. /Print ed./, 2006, vol. 304, iss. 2, pp. 835-837.

/5/ D. Nedeljković, R. Fišer, V. Ambrožič, Time-optimal magnetization of inductors with permanent magnet cores = Časovno-optimalno magnetenje dušilk z jedrom iz trajnega magneta. Inf. MIDEM, 2004, 34, No. 1, pp. 32-36.

/6/ M. Bugeza, R. Fišer, Estimation of linear electrical motor performance using finite element method = Vrednotenje obratovalnih lastnosti linearnih električnih motorjev s pomočjo metode končnih elementov. Inf. MIDEM, mar. 2007, 37, No. 1, pp. 42-49,

/7/ L. Gašperlin, A. Černigoj, S. Markič, R. Fišer, Additional cogging torque components in permanent-magnet motors due to manufacturing imperfections. IEEE trans. magn., Mar. 2009, vol. 45, no. 3, pp. 1210-1213,

/8/ Standard Test Methods for Metal Powders and Powder Metallurgy Products. MPIF, Princeton, NJ, 1995.

/9/ S. ST-Laurent, F. Chargon, Y. Thomas: Proceeding of 2000 PM2TEC International Conference, May30-June 3, 2000, New York, USA.

/10/ Powder Testing Center model PTC-03DT, User's manual V-20. KSK Powder Technologies Corp., 1996.

/11/ Patent of Ukraine UA 71954 C2 of 25.04.07, International application PCT/5E2004/001865, 20041215.

/12/ F. Meizda. Electronic measuring equipment and measurement methods: Translation from English. – M.: Mir, 1990. – 535 p.

M.V.Zagirnyak, V.V.Prus, V.P.Lyashenko
Kremenchuk Ostrogradskiy State Polytechnic
University, vul. Pershotravneva, 20, 39614,
Kremenchuk, Ukraine, e-mail: mzagirn@polytech.
poltava.ua

D. Miljavec
University of Ljubljana, Faculty of electrical
engineering, Trzaska 25, 1000 Ljubljana, Slovenia,
e-mail: miljavec@fe.uni-lj.si

ELECTROMAGNETIC ABSORBING MATERIALS

Branka Mušič[1], Andrej Žnidaršič[2], Peter Venturini[1]

[1]Helios Domžale d.d., Domžale, Slovenija
[2]Nanotesla Institut, Ljubljana, Slovenija

Key words: electromagnetic waves, magnetic composite, ferromagnetic materials, microwaves, measurements

Abstract: Around 15 years have passed since the wireless technologies started with rapid development. During that time, different fields of electromagnetic waves have become more active.

As a result of rapid advances in technology the use of wireless communication and radar systems is expanding quickly, which leads to a significant increase in the levels of background electromagnetic (EM) radiation /1/.

To avoid potential health effects from high exposure to electromagnetic waves, unnecessary EM waves should be eliminated to protect human bodies, especially expectant mothers and children /2/.

In European Pre-standard ENV 50166-2:1995 – Human exposure to electromagnetic fields – High frequency, is stated that electromagnetic fields interact with the human body and other systems through a number of physical mechanisms. Therefore, it is necessary to protect all of these systems.

As mentioned in ENV standard, it is recognized that additional considerations have been made by some countries, regarding the reference levels as minimum requirements in certain frequency ranges. Those considerations resulted in additional reference margins /3/.

This is the reason why is nowhere a background of electromagnetic waves including many reviews of diverse articles on topics of electromagnetic materials.

We decided to bring out that summery to deliver this diversified information to all types of readers, both technical and non-technical.

Absorberji elektromagnetnega valovanja

Kjučne besede: elektromagnetno valovanje, magnetni kompoziti, feromagnetni materiali, mikrovalovi, meritve

Izvleček: Okoli 15 let je minilo, odkar se je začel hiter razvoj brezžične tehnologije. Med tem časom so postala bolj aktivna tudi različna območja elektromagnetnih valov.

Kot rezultat hitrega razvoja tehnologije, se je uporaba brezžičnih komunikacij in radarskih sistemov naglo razširila. To vodi v znatno povišanje koncentracije elektromagnetnega sevanja v okolici /1/.

V izogib potencialnemu vplivu, pri visoki izpostavljenosti elektromagnetnemu valovanju, bi morali elektromagnetno sevanje omejiti oz. odstraniti, da bi zaščitili ljudi, posebno matere in otroke /2/.

V evropskem pred-standardu ENV 50166-2:1995 – Izpostava ljudi elektromagnetnemu polju – Visoke frekvence, je navedeno, da elektromagnetno polje vpliva na človeško telo in druge sisteme s številnimi fizikalnimi mehanizmi. Zato je potrebno vse te sisteme zaščititi.

Kot je zapisano v ENV standardu, so bile v nekaterih državah narejene dodatne raziskave, o minimalnih varnostnih zahtevah v zvezi z izpostavljenostjo v določenih frekvenčnih območjih. Ugotovitve teh raziskav so vodile v določenih državah do dodatnih, strožjih ukrepov. /3/.

Zgoraj omenjena dejstva in ugotovitve so povod, da smo v tem članku opisali ozadje elektromagnetnega valovanja in pregled različnih člankov na temo elektromagnetnih materialov.

1. Introduction

We have a different type of electromagnetic sources. The first one is natural source. Electromagnetic fields are present everywhere in our environment. Electric fields are produced by the local build-up of electric charges in the atmosphere and released with thunderstorms. Electromagnetic fields at low frequencies exist whenever a positive or negative electrical charge is present. Besides natural sources, the electromagnetic spectrum also includes fields generated by human-made sources. Various kinds of higher frequency radiowaves are used to transmit information – whether via TV antennas, radio stations or mobile phone base stations and radar produce high RF fields. And for example in the workplace: computers, fax machines, fluorescent lights, printers, scanners, telephone switching systems, electrical instruments, electric engines and other electrical devices. Additional sources are household appliances, such as stereo systems, refrigerators, blend-ers, portable heaters, clothes washers and dryers, coffee makers, vacuum cleaners, toasters, microwave ovens and others.

Like electric fields, magnetic fields are strongest close to their origin and rapidly decrease at greater distances from the source. Materials, such as building materials and trees, provide some shielding capability. Therefore, the electric fields from power lines outside the house are reduced by walls, buildings, and trees. Conductors, such as metal, provide very effective shield. However, magnetic fields are not blocked by common materials, buildings' walls, for example.

The protection from electromagnetic radiation is an up to date theme. Since the discovery that electromagnetic fields can affect our health, researchers have investigated these phenomena in vivo and in vitro, in animals /4-6/ and humans /7-13/.

A multiphase study has been performed to find an effective protection and method to evaluate systems and patients exposure to electromagnetic field (EMF). We have two typical ways. We can shield from EMF or use the absorbing method. But the shielding materials cannot eliminate or weaken EMI radiation, and moreover the reflected wave may interact with the incident wave, which causes disturbance to other devices. Another way is usage of electromagnetic absorbers like multipart materials that absorb incident electromagnetic radiation in limited wave spectrum. Only by using electromagnetic wave absorbing materials and transferring the electromagnetic energy to other forms can the radiation be attenuated to the furthest extent /14/.

In physics, absorption of electromagnetic radiation is procedure by which the energy of a photon is taken up by matter, typically the electrons of an atom. Thus, the electromagnetic energy is transformed to other forms of energy, for example, to heat.

According to the wave absorption mechanism, traditional wave absorbers can be divided into three types as electric loss, magnetic loss and dielectric loss materials. Carbon materials and conductive polymers are electric attenuation absorbents, which have higher electric loss tangent (tan δ_e) and the electromagnetic energy is mainly attenuated as resistor. Ferrites and fine powder are magnetic loss absorbents, which have higher magnetic loss (tan δ_m), and attenuate and absorb electromagnetic energy by polarisation mechanisms such as hysteresis loss and magnetic domain resonance. Metal fibre and many ceramic materials such as barium titanate belong to dielectric loss absorbents, which mainly attenuate electromagnetic energy by electronic and ionic polarisation. Most of the metal based absorbants used in cement matrix composites are steel fibres and ferrites, for which Japanese institute have made many studies /15/.

The reflection curve of an electromagnetic absorber is a function of a complex interplay between the permittivity, the permeability and the thickness of the absorber. From material point of view both permeability and permittivity can be varied, whereas with design an additional degree of freedom is obtained (thickness).

Absorptive layer can be made from either dielectric or soft-magnetic materials with appropriate loss tangent. Usually the absorber layers are made from composite materials, mixtures of dielectric (carbon black, aluminum flakes...) and/or soft-magnetic (ferrites, carbonyl iron) particles in some matrix; however, excellent absorbers can be made from ferrite ceramics for use at lower frequencies. Since every material has advantages and disadvantages, the selection of materials is difficult and depends on actual application.

Characterization of absorbers can be made directly with standardized measurements of reflection in free space or indirectly through measurements of constituent materials' electromagnetic properties. The latter method is greatly used in the designing phase, since in general the reflection from the absorber can be analytically calculated from known materials' characteristics and geometry /1/.

For simple one-layer absorber with metal backing the equation for reflection is:

$$R(dB) = 20 \cdot \log_{10}\left(\frac{iA\tan(kd) - 1}{iA\tan(kd) + 1}\right)$$

$$A = \sqrt{\frac{\mu}{\varepsilon}}$$

$$k = \frac{2\pi f}{c} \cdot \sqrt{\mu\varepsilon}$$

where μ and ε are complex permeability and permittivity respectively, f is the frequency of the incident EM wave, c is the speed of light in vacuum, and d is the thickness of the absorbing layer. From this we can see that the key parameters that can be varied are complex permeability and permittivity of material and thickness of layer, whereas frequency of the incident EM wave is external factor. An example of the reflection curve as a function of frequency is shown in Figure 2.

Fig. 1:   Scheme of a simple, one-layer absorber.
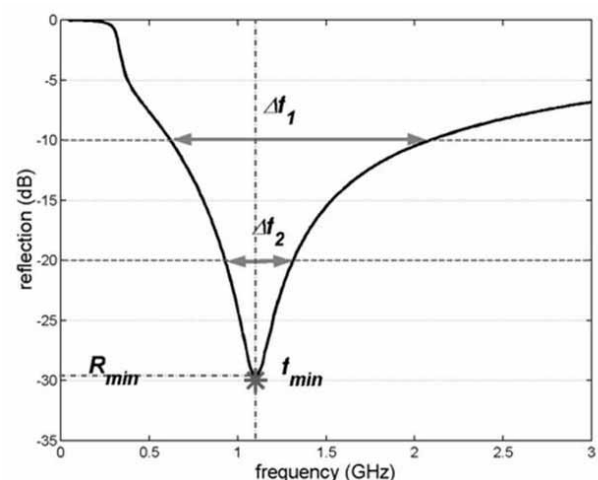
Fig. 2:   Reflection of one-layer absorber as a function of frequency. Reflection levels −10 dB and −20 dB correspond to 10% and 1% reflection of energy respectively.

In order to characterize the absorber properties three key parameters are used: width of absorption band Δf, frequency range where reflection is below some level, usually – 10 dB (10% reflection) or – 20 dB (1% reflection); frequency of minimum reflection f_{min}; and level of reflection at f_{min}, R_{min}. An evaluation of quality of the reflection curve is rather arbitrary and depends on the desired frequency range and level of absorption, which usually differ for various applications.

2. Review of existing experimental work

Electromagnetic materials are advantageous for applications of microwave and millimeter wave protection.

Many characteristic can influence on materials absorbing properties. In present article I will mention some significance evaluation of efficiency of electromagnetic absorbing materials dependent on chemical structures, concentrations, sizes, shapes and syntheses. Different characteristic of electromagnetic materials with various methods have been studied by many authors /16-21/.

Research group from India investigated the microwave absorption of M-type hexaferrite-polymer composites prepared with different ferrite ratios of 50 wt.%, 60 wt.%, 70 wt.%, 80 wt.% in polyurethane matrix. Investigated have been in 8,2-12,4 GHz frequency range. It was found that the absorption properties in the composites are greatly improved with increasing ferrite contents in the polymer matrix. The composite with 80 wt. % ferrite content has shown a minimum reflection loss of -24,5 dB at 12 GHz with a -20 dB bandwidth over the extended frequency range of 11-13 GHz in a quite thin sample with a thickness of only 1,6 mm /22/. The permittivity, permeability and absorbing properties of coatings with carbonyl-iron particles as absorber and epoxy-silicone resins as matrix was also represented. The properties were investigated with different weight concentrations in the frequency range of 2-18 GHz. The plate shape (flake) particles of a carbonyl-iron have a size of 2-5 μm and about 1 μm thicknesses. The content of carbonyl-iron particles was 50 wt.%, 55 wt.%, 60 wt.%, 65 wt.%, 70 wt.% and 75 wt.%. Both the values of the real and imaginary parts of the permittivity increase with the carbonyl-iron weight concentration. The initial permeability increased more or less linearity to 70 wt. % and rapidly increased from 70 to 75 wt. %. A minimum reflection loss value of -42,5 dB was obtained at 10,6 GHz for the containing 55 wt. % carbonyl-iron. When the coating contains 75 wt.% carbonyl-iron particles, the region of reflection loss values less then -10 dB is below 2 GHz /23/.

Lots of studied showed that the microwave properties of electromagnetic absorber materials depend on particle size, shape and granulate.

The goal of next work was investigation of absorbing properties for different shapes and aggregated states of carbonyl-iron particles dispersed in epoxy resin matrix at various volume concentrations of 0,3-0,6 vol.%. The de-aggregated flake–shaped carbonyl-iron particles have higher permeability, lower permittivity and better absorbing properties in the frequency range of 2-18 GHz then aggregated sphere-shaped particles. The flake-shaped composite for 60 vol.% has the minimum reflection loss value -12,2 dB at 4,4 GHz for a 1 mm thickness layer /24/. Spherical and monodisperse $Co_{20}Ni_{80}$ particles were prepared, in the micrometer and sub-micrometer size range. The particle are with a mean diameter 1,4 μm, a narrow size distribution, and a low degree of agglomeration. The particles of second sample are smaller with a mean diameter 0,33 μm. Particles were randomly dispersed in epoxy resin. Microwave properties of composites were measured in 0,1-18 GHz. The micrometer size particles exhibit a permeability curve with a single resonance bands. The submicrometer size particles exhibit a behavior with three resonance bands /25/.

Some studies indicate that the hexagonal strontium ferrite is also good microwave absorber /26-27/. It is more adaptable than ferrites with spinel and garnet structure in case of a high frequency. However, susceptibility of ferrites at these frequencies is low, which makes it difficult to further improve their microwave absorption property. The susceptibility of metal powder is higher /28-29/ and such materials are typically used for frequencies up to 30 GHz.

In literature we can find researchers reports that plated layer on absorbers materials can improve absorbing properties of electromagnetic radiation. Modifying the properties of one material by coating it with another type of material has been a popular approach widely documented in the literature /30-34/.

Shanghai's Jiao Tong University worked on the synthesis of anatase coated barium ferrite composite particles suitable for microwave absorption applications. They reported on core-shell (barium-anatase) structures of magnetic particles that exhibit unique magnetic properties. The results of prepared sample with 75 wt.% ferrite in epoxy resin, in the frequency range of 2-12 GHz show that the titanium coverage on barium ferrite has a great influence on its microwave properties. The maximum reflection loss was obtained at the Ti:Ba ratio of 1:10 /35/. It is found that the complex permeability of the sintered ferrite Ni_2Y (Y-type hexagonal ferrite, $Ba_2Ni_2Fe_{12}O_{22}$) is higher than that of the ferrite composite Ni_2Y. Because the ferrite composite is composed of the ferrite particles coated with non-magnetic layer, its complex permeability is decreased. The complex permeability of the ferrite absorber is dependent upon frequency, but the complex permittivity is nearly constant. In those ferrite bodies most of the loss is mainly attributed to magnetic loss, while their dielectric loss is negligible /36/. China's Shanghai University has reported that the best way to solve this problem is fabricating the composite of ferrite and metal powder efficiently. They prepared a new type of Ni-coated strontium ferrite magnetic nanosized powder (Ni/

$SrFe_{12}O_{19}$) with electroless plating enchased by ultrasonic wave at room temperature. Their results show that the powder possesses excellent microwave absorption properties. The microwave absorption properties were measured from 5 to 15 GHz. They shown that the maximum microwave loss of the composite powder reach -41,3 dB. The bandwidth with the loss above -10 dB was 8 GHz /37/.

Japan scientists already presented a NiZn ferrite spin sprayed film, 3 µm thick, as a material exhibiting strong magnetic loss (reaching 67% attenuation of magnetic field at 3 GHz) and also reflection loss weak (smaller then 7%) enough to be practically applied to noise suppressors operated up to several GHz /38/.

Development of new magnetic materials and their understanding on a smaller – nano scale is a cause of advance in many areas of materials science. For a variety of important applications show promise for future, because of its large specific surface areas and the nano particles are much less then the incident wavelength, so it can greatly reduce the reflection from the surface, which make better impedance matching /39/. Researchers from Tokyo University achieved similar results by combining reverse-micelle and sol-gel techniques to create high-performance millimeter wave (30-300 GHz) absorber composed of a series of ε-$Al_xFe_{2-x}O_3$ nanomagnets with particles size between 25 nm and 50 nm. These materials show natural resonance in the region up to 182 GHz, which is the highest frequency for magnetic materials. The absorption peaks in millimeter wave range for samples: 30 wt. % (x = 0), 26 wt. % (x = 0,06), 24 wt. % (x = 0,09), 30 wt. % (x = 0), 29 wt. % (x = 0,21), 29 wt. % (x = 0,3) and 34 wt. % (x = 0,04) were observed at 112, 125, 145, 162, 172 and 182 GHz, respectively /40/. The α-Fe/$C_{(amorphous)}$ and $Fe_3C_{(amorphous)}$ nanocomposites have been prepared. The epoxy resin compacts with 40 vol.% α-Fe/$C_{(amorphous)}$, and Fe_3C/$C_{(amorphous)}$, were characterized in frequency range of 0,05-26,5 GHz. Powders provided good electromagnetic wave absorption performances (reflection loss < -20 dB) in ranges 4,3-8,2 GHz, and 9-26,5 GHz over absorber thicknesses of 1,8-3,3 mm and 1-2,4 mm, respectively /41/.

Behave of materials and device structures whose characteristic feature sizes are on nanometer scale are reported /42/.

There are numerous electromagnetic materials on the market designed for a wide variety of applications.

This short section show that is in specified field of work many different opportunities for further investigations exist for absorbing materials.

3. Conclusion

Electromagnetic materials are becoming more and more important for our society. We can find applicability in many different fields, for example in electronics or medicine.
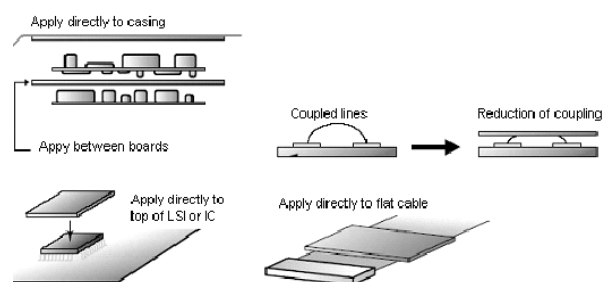
Fig. 3: *Examples of applications soft-magnetic composites for reduction of electromagnetic noise.*

Which type of electromagnetic protection should be used depends on the requirements and technical limitations.

With electromagnetic absorbing materials we can decrease the effects of EM waves on the human body and other systems.

Different scientists from around the word are looking for better and better materials with new, different properties, with higher effectiveness and efficiency.

However, as long as there is a possibility to do something better, a need for new materials and their new properties research will exist.

Literature

/1/ Bregar V.B., Žnidaršič A., Lisjak D., Drofenik M., Development and characterization of an electromagnetic absorber. Materiali in tehnologije, 2005, 39, 89-39

/2/ Committee on identification of research needs relating to potential biological or adverse health effects of wireless communications devices, National Research Council. Identification of Research Needs Relating to Potential Biological or Adverse Health Effects of Wireless Communication; National Academies Press: WA, 2008

/3/ European Pre-standard ENV 50166-2 – Human exposure to electromagnetic fields – High frequency

/4/ Microwave News, (1986, Sept./Oct.). (pp. 5, 14).

/5/ Ad ey, R.W., Bawin, F. M., & Lawrence, A.F. (1982). Effects of weak amplitude-modulated fields in calcium efflux from awake cat cerebral cortex. J. Bioelectromagnetics Soc., 3, 295-308.

/6/ Bullock, T. H. (1977). Electromagnetic sensing in fish. Neurosci. Res. Program Bull., 15, 17-22/.

/7/ Ravitz, L. J. (1982). History, measurement, and applicability of periodic changes in the electromagnetic field in health and disease. Ann. N.Y. Acad. Sci., 98, 1144-1201.

/8/ Wever, R. A. (1973). Human circadian rhythms under the influence of weak electric fields and the different aspects of these studies. Int. J. Biometeor., 17, 227-232.

/9/ Smith, C. W. (1985). Superconducting areas in living systems. In R. K. Mishra (Ed.), The living state II (pp. 404-420). Singapore: World Scientific.

/10/ Phillips, R. D. (1986, Sept.). Health effects of ELM fields: Research and communications regulation. Toronto, Int'l Utilities Symp.

/11/ Smith, C. W., Jafarg-Asl, A. H., Choy, R.Y.S., & Monro, J.A.; The emission of low-intensity electromagnetic radiation from multiple allergy patients and other biological systems. In B. Jezowska-Trzebiatowska, B. Kochel, J. Slawinski, and W. Streck (Eds.)

Proc. int'l. symp. on photon emission from biological systems (pp. 110-126), Wroclaw, Poland. Singapore: World Scientific.

/12/ Ketchenm, E. E., Porter, W. E., & Bolton, N. E. (1978). The biological effects of magnetic fields on man. J. Am. Ind. Hyg. Assoc., 39, 1-11.

/13/ Smith, C.W., & Best, S. (1989). Electromagnetic man. New York: St. Martins Press.

/14/ N. Dishovsky, M. Grigorova. On the correlation between electromagnetic waves absorption and electrical conductivity of carbon black filled polyethylenes. Mater. Res Bull 35(3), pp. 403-409 (2000)

/15/ Guan, S. Liu, Y. Duan, J. Cheng. Cement based electromagnetic shilding and absorbing building msterials. Cement & Concrete Composites 28, pp. 468-474 (2006)

/16/ Hribernik B., »Uvod v magnetne materiale«, 1. izdaja Tehniška fakulteta VTO-ERI, Maribor 1991

/17/ Hamler A., Hribernik B., »Elektrotehnični materiali«, Založniška dejavnost FERI, Tiskarna tehniških fakultet, 2005

/18/ Fiorillo F., »Measurement and characterisation of magnetic materials«, Elsevier Academic Press, 2004

/19/ Berttoti G., Hysteresis in magnetism for physicist, material scientists, and engineers, San Diego; Academic Press, cop. 1998

/20/ Wohlfarth E.P., Handbook of Magnetic Materials; Elsevier: Amsterdam, 1980; Vol.2

/21/ Committee on identification of research needs relating to potential biological or adverse health effects of wireless communications devices, National Research Council. Identification of Research Needs Relating to Potential Biological or Adverse Health Effects of Wireless Communication; National Academies Press: WA, 2008

/22/ S.M. Abbas, A.K. Dixit, R. Chatterjee, T.C. Goel. Complex permittivity, complex permeability and microwave absorption properties of ferrite-polymer composites. Journal of Magnetism and Magnetic Materials, 309 (2007)

/23/ Y. Qing, W. Zhou, F. Luo, D. Zhu. Microwave-absorbing and mechanical properties of carbonyl-iron/epoxy-silicone resin coatings. Journal of Magnetism and Magnetic Materials 321 (2009) 25-28.

/24/ B. Zhang, Y. Feng, J. Xiong, Y. Yang, H. Lu. Microwave-Absorbing Properties of De-agglomerated Flake-shaped Carbonyl-Iron Particle Composites at 2-18 GHz. IEEE Transactions on magnetics, vol. 42, No. 7 (2006).

/25/ G. Viau, F. Ravel, O. Acher, Preparation and microwave characterization of spherical and monodisperse $Co_{20}Ni_{80}$ particles. J.Appl. Phys. 76 (10), (1994).

/26/ Verma A., Mendiratta R.G., Goel T.C., Dube D.C. (2002) J. Electroceram 8:203

/27/ Fang Q.Q., Liu Y.M., Li X.G. (2001) J. Magn. Magn. Mater 234:366

/28/ Ding J., Shi Y., Chen L.F., Deng C.R., Fuh S.H., Li Y. (2002) J. Magn. Magn. Mater 247:249

/29/ Zhou P.H., Xie L.J., lang D.F., Chen L., Zhao X.Q. (2005) J Magn. Magn. Mater 292:325

/30/ Quirantes A., Plaza R., Delgado A.; J. Colloid Interface Sci. 189 (1997) 236–241

/31/ Ishikawa T., Matijevic E., Langmuir 4 (1988) 26–31

/32/ Zabetakis D., Dinderman M., Schoen P., Adv. Mater. 17 (2005) 734–738

/33/ Watson S., Beydoun D., Amal R., J. Photochem. Photobiol. A: Chem 148 (2002) 303–313

/34/ Park O.K., Kang Y.S., Colloid Surface A 257–258 (2005) 261–265

/35/ Tang X., Zhao B.Y., Tian Q., Hu K.A. Synthesis, characterization and microwave absorption properties of titania-coated barium ferrite composites. Journal of Physics and Chemistry of Solids 67 (2006) 2442–2447

/36/ J.Y.Shin, J.H.Oh, »The Microwave Absorbing Phenomena of Ferrite Microwave Absorbers«, IEEE Transaction on Electromagnetic Compatibility, vol. 29, No. 6 (1993).

/37/ Pan X., Qiu J., Gu M. Preparation and microwave absorption properties of nanosized Ni/SrFe12O19 magnetic powder. (2007) J. Mater Sci 42:2086-2089

/38/ Kondo K., Chiba T., Ono H., Yoshida S. Conducted noise suppression effect up to 3 GHz by NiZn ferrite film plated at 90 C directly onto printed circuit board. (2003) Journal of Applied Physics Vol.93, No.10, Parts 2,3.

/39/ P. Tablot, A.M. Konn, C. Brosseau, Electromagnetic characterization of fine-scalecomposite materials, J.Magn. Mater 249(3):481-5 (2002).

/40/ A. Namai, S. Sakurai, .M. Nakajima, T. Suemoto, K. Matsumoto, M. Goto, S. Sasaki, S. Ohkoshi. Synthesis of an Electromagnetic Wave Absorber for High-Speed Wireless Communication. JACS ARTICLES, Published on Web 12/30/2008

/41/ J.R.Liu, M. Itoh, T. Horikawa, E. Taguchi, H. Mori, K. Machida. Iron based carbon nanocomposites for electromagnetic wave absorber with bandwidth in GHz range. J. Appl. Phy. A 82, pp.509.513 (2006).

/42/ P. Tablot, A.M. Konn, C. Brosseau. Electromagnetic characterization of fine-scale particulate composite materials. Journal of Magnetism and Magnetic Materials, 249, pp. 481-486 (2002).

mag. Branka Mušič
Helios Domžale d.d., Količevo 2,
1230 Domžale, Slovenija
e-mail: branka.music@helios.si
Telefon: + 386 1 722 40 09; Fax: + 386 1 722 43 50

Doc. dr. Andrej Žnidaršič
Nanotesla Institut, Stegne 29, 1521 Ljubljana
e-mail: andrej.znidarsic@kolektor.com
Telefon: + 386 1 583 31 22; Fax: + 386 1 583 32 31

Doc. dr. Peter Venturini
Helios Domžale d.d., Količevo 2,
1230 Domžale, Slovenija
e-mail: peter.venturini@helios.si
Telefon: + 386 1 722 43 73; Fax: + 386 1 722 43 50

ANALYSIS OF METAMATERIAL ATTACHMENT FOR EM ABSORPTION IN HUMAN HEAD

Mohammad Rashed Iqbal Faruque[1], Mohammad Tariqul Islam [2], Norbahiah Misran[1, 2]

[1]Dept. of Electrical, Electronic and Systems Engineering, Faculty of Engineering and Built Environment, Universiti Kebangsaan Malaysia, Selangor, Malaysia.
[2]Institute of Space Science (ANGKASA), Universiti Kebangsaan Malaysia, Selangor, Malaysia.

Key words: antenna, human head model, lossy-Drude model, metamaterials, specific absorption rate (SAR).

Abstract: The reducing specific absorption rate (SAR) with metamaterials attachment is investigated in this paper. The finite-difference time-domain method with lossy-Drude model is adopted in this analysis. The technique of SAR reduction is discussed and the effects of attaching location, distance, and size of metamaterials, perfect electric conductor (PEC), and materials on the SAR reduction are investigated. Metamaterials have achieved a 41.47% reduction of the initial SAR value for the case of 1 gm SAR. These results suggest a guideline to choose various types of metamaterials with the maximum SAR reducing effect for a phone model.

Vpliv dodatka metamateriala na absorpcijo EM valovanja v človeški glavi

Kjučne besede: antena, model človeške glave, lossy-Drude model, metamateriali, specifična absorbcijska stopnja (SAR)

Izvleček: v članku opišemo zmanjšanje parametra SAR (specifična absorbcijska stopnja) z dodatkom metamateriala. Analizo smo opravili z modelom Drude in uporabo končnih diferenc v časovni domeni. Opisana je tehnika zmanjšanja parametra SAR , raziskani so vpliv lokacije, oddaljenosti in velikosti metamaterialov ter vpliv popolnega električnega prevodnika (PEC) in vrste metamaterialov na zmanjšanje SAR. Z uporabo metamaterialov smo dosegli 41,47 % zmanjšanje začetne vrednosti SAR, ki je bila 1gm SAR. Ti rezultati pomenijo neko vrsto smernic za izbiro materialov za mobilne telefone, ki najbolj zmanjšujejo parameter SAR.

1. Introduction

With the rapid and ever more widespread use of mobile phones, public concern regarding the possible health hazards has been growing, which brings an increased requirement on electromagnetic (EM) absorption for mobile phones. The basic parameter in the EM absorption is defined in terms of the specific absorption rate (SAR), or the absorbed power in unit mass of tissue /1/. The SAR is generally evaluated using either phantom measurement or computer simulation. The finite-difference time-domain (FDTD) method is currently the most widely accepted means for the SAR computations /2/. The interaction of handset antennas with the human body is a great consideration in cellular communications. The user's body, especially the head and hand, influence the antenna voltage standing wave ratio (VSWR), gain, and radiation patterns. Furthermore, thermal effects, when tissues are exposed to unlimited electromagnetic energy, can be a serious health hazard. Therefore standards organizations have set exposure limits in terms of SAR /3, 4/. SAR is a measure of the rate at which radio frequency (RF) energy is absorbed by the body when exposed to a radio-frequency electro-magnetic field. SAR is used to measure exposure to fields between 100 kHz and 10 GHz /5-8/. It is commonly used to measure power absorbed from mobile phones and during MRI scans. The value will depend on the geometry of the part of the body that is exposed to the RF energy, and on the exact location and geometry of the RF source.

Cellular phone protection and the enforcement of pertinent exposure standards are issues in the current media, and regulatory agencies are motivated to assure that compliance testing is acceptable. IEEE Standard 1528 /3/ and IEC 62209-1 specify protocols and process for the measurement of the peak spatial-average SAR induced inside a simplified model of the head of users of hand held radio transceivers (cellular phones). For example, the SAR limit specified in IEEE C95.1: 1999 is 1.6 W/kg in a SAR 1 gm averaging mass while that specified in IEEE C95.1: 2005 has been updated to 2 W/kg in a 10 gm averaging mass /4/. This new SAR limit specified in IEEE C95.1: 2005 is comparable to the limit specified in the International Commission on Non-Ionizing Radiation Protection (ICNIRP) guidelines.

The interaction of the cellular handset with the human head has been investigated by many published papers considering; first, the effect of the human head on the handset antenna performance including the feed-point impedance, gain, and efficiency /7-9/, and second, the impact of the antenna EM radiation on the user's head due to the absorbed power, which is measured by predicting the induced SAR in the head tissue /10-13/.

The most used method to solve the electromagnetic problem in this area is the finite-difference time-domain (FDTD) technique /13-14/. Although, in principle, the solution for general geometries does not require any additional effort

with respect to the standard method, the technique requires the definition of a discretized space by assigning to each cell its own electromagnetic properties, which is not an easy process /15-18/. Specifically, the problems to be solved in SAR reduction need a correct representation of the cellular phone, anatomical representation of the head, alignment of the phone and the head, and suitable design of metamaterials.

In /12/,/19/ a perfect electric conductor (PEC) reflector was placed between a human head and the driver of a folded loop antenna. The result showed that the radiation efficiency can be enhanced and the peak SAR value can be reduced. In /15/, /20/ a study on the effects of attaching conductive materials to cellular phone for SAR reduction has been presented. It is shown that the position of the shielding material is an important factor for SAR reduction effectiveness. There is a necessity to make an effort for reducing the spatial peak SAR in the design stage of the ferrite sheet because the possibility of a spatial peak SAR exceeding the recommended exposure limit cannot be completely ruled out.

Metamaterials have inspired great interest due to their unique physical properties and novel application /14/, /21/. Metamaterials denote artificially constructed materials having electromagnetic properties not generally found in nature. Two important parameters, electric permittivity and magnetic permeability determine the response of the materials and metamaterials to electromagnetic fields. The negative permittivity can be obtained by arranging the metallic thin wires periodically /22-24/. On the other hand, an array of split ring resonators (SRRS) can exhibit negative effective permeability. The designed SRRS operated at 1.8 GHz and were used to reduce the SAR value in a lossy material. In /12/, the designed SRRS operated at 1.8 GHz were used to reduce the SAR value in a lossy material. The metamaterials are designed on circuit board so it may be easily integrated to the cellular phone. Simulation of wave propagation into metamaterials was proposed in /13/. The authors utilized the FDTD method with lossy-Drude models for metamaterials simulation. This method is a helpful approach to study the wave propagation characteristics of metamaterials /25/ and has been more developed with the perfectly matched layer (PML) and extended to three-dimension problem /26/.

At first materials are placed between the antenna and a human head, and then replaced by a metamaterial. In order to study the SAR reduction of an antenna operated at the GSM 900 band, the effective medium parameter of metamaterials is set to be negative at 900 MHz Different positions, sizes, and negative medium parameters of metamaterials for SAR reduction effectiveness are also analyzed.

This paper is structured as follows. Section II describes the numerical analysis of the handset together with the SAM phantom head, and the FDTD method is used with positive meshing techniques for quick and correct analysis. will be described in Section II. The SRRS structure, design and simulation of metamaterials results are explained in Section III, Section IV concludes the paper.

2. Simulation model and numerical techniques

A. Model Description

The simulation model which includes the handset with PIFA type of antenna and the SAM phantom head provided by CST Microwave Studio® (CST MWS) is shown in Fig. 1. A complete handset model composed of the circuit board, LCD display, keypad, battery, and housing was used for simulation. The relative permittivity and conductivity of individual components were set to comply with industrial standards. In addition, definitions in /5-6/, /20/ were adopted for material parameters involved in the SAM phantom head. In order to accurately characterize the performance over a broad frequency range, dispersive models for all the dielectrics were adopted during the simulation /5/. Fig. 2 shows the dispersive permittivity of the liquid in the SAM phantom head for simulation. In Fig. 2, Eps' and Eps'' represents dielectric dispersion fit Debye 1st order and 2nd order respectively. The electrical properties of materials used for simulation are listed in Table 1. A PIFA type antenna constructed in a helical sense operating at 900 MHz for GSM application was used in the simulation model. In order to obtain a high-quality geometry approximation for such a helical structure, a predictable meshing scheme used in the FDTD method usually requires large number of hexahedrons which in turn makes it extremely challenging to get convergent results within reasonable simulation time.
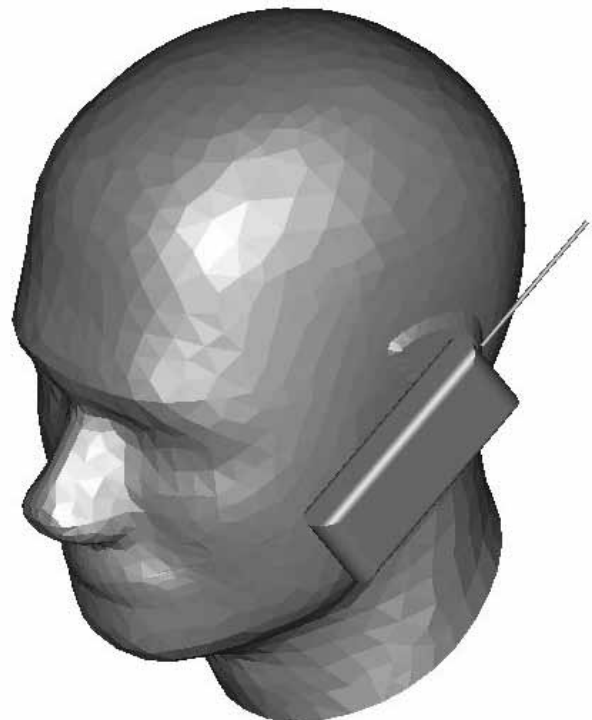
Fig. 1.   Complete model used for simulation including handset and SAM phantom head.
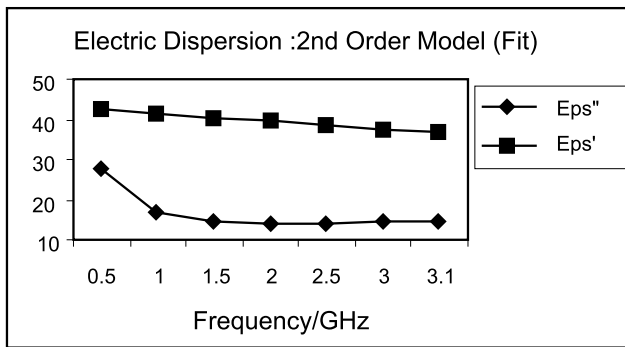
Fig. 2.   Dispersive permittivity of the liquid in the SAM phantom head used for simulation.

Table 1: Electrical properties of materials used for simulation

Phone Materials	ε_r	$\sigma(S/m)$
Circuit Board	4.4	0.05
Housing Plastic	2.5	0.005
LCD Display	3.0	0.02
Rubber	2.5	0.005
SAM Phantom Head		
Shell	3.7	0.0016
Liquid @ 900MHz	40	1.42

B.   Numerical Technique

CST MWS, based on the finite integral time-domain technique (FITD), was used as the main simulation instrument. A non-uniform meshing scheme was adopted so that the major computation endeavor was dedicated to regions along the inhomogeneous boundaries for fast and perfect analysis. Fig. 3 shows the mesh for two cut planes of the complete model indicating the area with denser meshing along the inhomogeneous boundaries. The minimum and maximum mesh sizes were 0.3 mm and 1.0 mm, respectively. A total of 2,097,152 mesh cells were generated for the complete model, and the simulation time was 1163 seconds (including mesh generation) for each run on an Intel Core™ 2 Duo E 8400 3.0 GHz CPU with 4 GB RAM system.

The analysis workflow started from the design of the antenna with complete handset model in free space. The antenna was designed such that the $S11$ response was less than -10 dB over the frequency band of interest. The SAM phantom head was then included for SAR calculation using the standard definition as /7/

$$SAR = \frac{\sigma}{2\rho} E^2.$$

where E is the induced electric field (V/m), ρ is the density of the tissue (kg/m³), and σ is the conductivity of the tissue (S/m). The resultant SAR values averaged over 1 gm and 10 gm of tissue in the head were denoted as SAR 1 gm and SAR 10 gm, respectively. These values were used as a benchmark to appraise the effectiveness in peak SAR reduction.
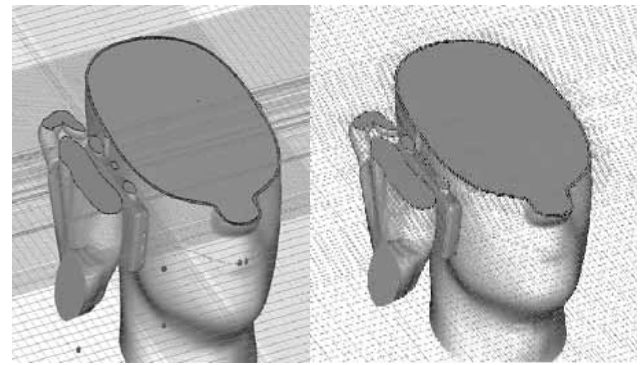
Fig. 3.   Mesh view for two cut planes of the complete model showing the non-uniform meshing scheme adopted for simulation.

Fig. 4 shows a portable telephone model at 900 MHz for the present study. It was considered to be a quarter wavelength PIFA antenna mounted on a rectangular conducting box. The conducting box was 10 cm tall, 4 cm wide, and 3 cm thick. The PIFA antenna was located at the top surface of the conducting box.
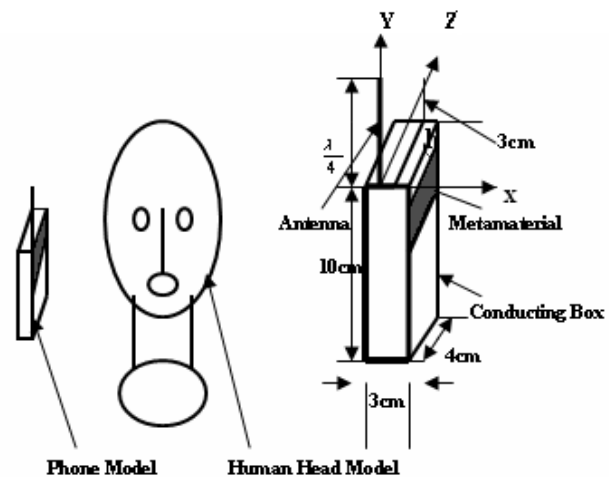
Fig. 4.   The head and antenna model for SAR calculation.

The SAM head model was considered for this research where it consists about 2,097,152 cubical cells with a resolution of 1 mm. The FDTD method was employed in the numerical analysis. Its discretized formulations were derived from the following Maxwell's time-domain equations:

$$\frac{\delta H}{\delta t} = -\frac{1}{\mu_0 \mu_r'} \left(\nabla \times E \right) - \frac{\sigma^*}{\mu_0 \mu_r'} H. \tag{1}$$

$$\frac{\delta E}{\delta t} = -\frac{1}{\varepsilon_0 \varepsilon_r'} \left(\nabla \times H \right) - \frac{\sigma}{\varepsilon_0 \varepsilon_r'} E. \tag{2}$$

where $\sigma^* = \omega \mu_0 \mu_r'$ and $\sigma = \omega \varepsilon_0 \varepsilon_r''$ were added for treating magnetically and electrically lossy materials, respectively. A space domain enclosing the human head and the phone model is also shown in Fig. 5. The time step was set to $\frac{\delta}{\sqrt{3}c}$, where c

is the speed of light, to guarantee the numerical stability. The time-stepping was performed for about eight sinusoidal cycles in order to reach a steady state. To absorb the outgoing scattered waves, the second order Mur absorbing boundaries acting on electric fields were used. An antenna excitation was introduced by specifying a sinusoidal voltage across the one-cell gap between the helix and the top surface of the conducting box.

The antenna output power is defined as

$$\mathrm{P}_{out} = \mathrm{P}_{abs} + \mathrm{P}_{ferr} + \mathrm{P}_{rad}$$

$$= \frac{1}{2}\int_{Vh}\sigma\left|E\right|^2 \mathrm{dv} + \frac{1}{2}\int_{Vf}(\sigma\left|E\right|^2 + \sigma^*\left|H\right|^2)\,\mathrm{dv}$$

$$+ \frac{1}{2}\,\mathrm{Re}\,(\int_s E \times H^*.\vec{n}.\mathrm{ds})$$

(3)

where P_{abs} is the power absorbed in the head with a volume of V_h, P_{ferr} is the power dissipated in the ferrite sheet with a volume of V_f, and $P_{rad..}$ is the power radiated to the far-field, which can be calculated by integrating the normal component of the Pointing vector E x H^* over a surface S completely surrounding the head/phone model configuration.

3. Reduction of sar using metamaterial

The SAR in the head can be reduced by placing a metamaterial between the antenna and the human head. The metamaterial is on a scale less than the operating wavelength. The structures are resonant due to internal capacitance and inductance. The stop band can be designed at the operation bands of cellular phone radiation. The metamaterial are designed on a printed circuit board so it may be easily integrated to the cellular phone. By arranging sub-wavelength resonators periodically we get the metamaterial structure.

A. SRRS Structure

We establish that metamaterials can be used to reduce the peak SAR 1 gm and SAR 10 gm in the head from the FDTD analysis. In this section, metamaterials operated at the 900 and 1800 MHz bands of the cellular phone were considered. The metamaterials can be attained by arranging SRRS periodically. The SRRS structure consists of two concentric rings of conductive material. There is a gap on each ring, and each ring is situated opposite to the gap on the other ring. The schematics of the SRRS structure that we used in this study as shown in Fig. 6. The significant frequency of the SRRS can be varied toward a higher or lower frequency band by appropriately choosing these structure parameters.

B. SRRS Design

To construct the metamaterial for SAR reduction, we proposed one model of resonators namely the SRRS as shown in Fig. 6. We design the resonators for operation at the 900 MHz bands. The SRRS contains two square

rings, each with gaps appearing on the opposite sides /14/. The SRRS was introduced by Pendry et al. in 1999 /16/ and subsequently used by Smith et al. for synthesis of the first left-handed artificial medium /21/. A lot of effort worldwide has been spent studying single negative metamaterials (SNMs), double negative metamaterials (DNMs), their properties /5-7/, /21/, applications in antennas /7/, /21–22/, and other microwave devices /21– 23/. In Fig. 6, the structures of resonators are defined by the following structure parameters: the ring thickness *c*, the ring gap *d*, the square ring size *l*, the split gap *g,* and c_0 is the speed of light in free space. The resonant frequency *f* is very sensitive to small changes in the structure dimensions of the SRRS. The frequency response can be scaled to higher or lower frequency by properly choosing these geometry parameters. After an extensive simulation study, we have found out a closed-form formula for the resonant frequencies of the SRRS:

$$\mathrm{f}_{SRRS} = \mathrm{k}_1 \frac{c_0}{2[4(2r_{ext}-c)-g]\varepsilon_r^{1/2}}$$

(4)

The SRRS is resonating at approximately half the guided-wavelength of the resonant frequency. There are two resonances from the split rings. We have given the formula for the resonance of the outer split ring, which has a lower resonance frequency.
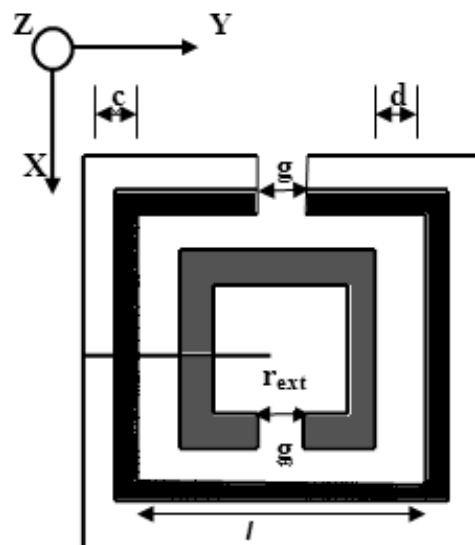
Fig. 6.   The structure of the SRRS.

Numerical simulations that predict the transmission properties depend on the various structure parameters of this system. Simulations of this complex structure are performed with the FDTD method. To construct the resonators for SAR reduction, let us assume that the resonators lie in the *xz* plane, as shown in Fig. 7. The EM wave propagates along the *y* direction. The electric polarization is kept along the *z*-axis and magnetic field polarization is kept along *x* axis. Periodic boundary conditions are used to reduce the computational domain and an absorbing boundary condition is used at the propagation regions. The total-field/scatter-field formulation is used to excite the plane wave. The regions

inside of the computational domain and outside of the SRRS were assumed to be vacuum.
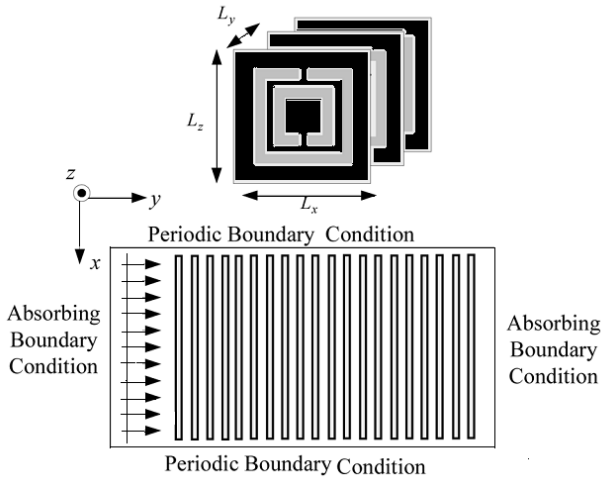
Fig. 7   Top view of a plane wave incident on the periodic (SRRS).

From this study, it is found that both of the two incident polarizations can produce a stop band. As shown in /23-26/, the stop band corresponds to a region where either the permittivity or permeability is negative. When the magnetic field is polarized along the split ring axes, it will produce a magnetic field that may either oppose or enhance the incident field. A large capacitance in the region between the rings will be generated and the electric field will be powerfully concentrated. There is strong field coupling between the SRRS and the permeability of the medium will be negative at the stop band. Because the magnetic field is parallel to the plane of SRRS, we imagine the magnetic effects are small, and that permeability is small, positive, and slowly varying. In this condition, these structures can be viewed as arranging the metallic wires periodically.

The stop bands of the SRRS are designed to be at 900 MHz and 1800 MHz. The periodicity along x, y, z axes are L_x = 63 mm, L_y = 1.5 mm, and L_z = 63 mm respectively. On the other hand, to obtain a stop band at 1800 MHz, the parameters of the SRRS are chosen as c = 1.8 mm, d = 0.6 mm, g = 0.6 mm, and r = 12.9 mm. The periodicity along the x, y, z axes are L_x = 50 mm, L_y = 1.5 mm, and L_z = 50 mm, respectively. Both the thickness and dielectric constant of the circuit boards for 900 MHz and 1800 MHz are 0.508 mm and 3.38 mm respectively. After properly choosing geometry parameters, the SRRS medium can display a stop band around 900 MHz and 1800 MHz. SRRS producing a good stop band and size are large. Therefore, SRRS are suitable for mobile phones as per size and recital point of view.

We have tried to use a high impedance surface configuration /22/ to reduce the peak SAR. However, we found that when these structures operate at 900 MHz, the sizes of these structures are too large for cellular phone application. A negative permittivity medium can also be constructed by arranging the metallic thin wires periodically /24/. However,

we found that when the thin wires operate at 900 MHz, the size is also too large for practical application. Because the SRRS structures are significant due to internal capacitance and inductance, they are on a scale less than the wavelength of radiation. In this study, it is established that the SRRS can be designed at 900 MHz while the size is similar to that of a cellular phone.

Table 3: Comparisons of peak sar at 900 mhz without metamaterial

Tissue	SAR value (W/kg)
SAR value for /7/	2.17
SAR value for /14/	2.43
SAR value for /20/	2.28
SAR value this work for 1 gm	2.002
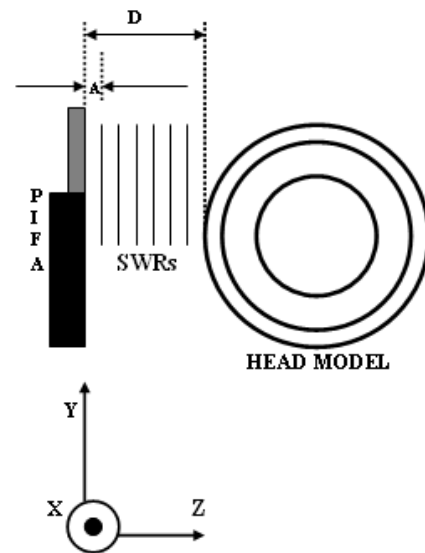
Fig. 8.   The antenna, metamaterials, and head model for SAR reduction.

C.   Results

The designed SRRS were placed between the antenna and the human head. Fig. 8 shows the head used in SAR simulation. The antenna was arranged parallel to the head axis. The distance between the antenna and head surface was 20 mm. The SAR value was calculated for an antenna output power equal to 600 mW. The calculated peak SAR 1 gm without metamaterials was 2.002 W/kg. The SAR simulation is compared with the results in /7/, /14/, /20/ for validation, as shown in Table III. The distance between the antenna feeding point and edge of the metamaterials was A= 3 mm. The size of the metamaterials in the *xz* plane was 48 mm × 48 mm and the thickness was 6 mm. The SAR value and antenna performance with the metamaterial were analyzed. To evaluate the power radiated from the antenna, the source impedance (Z_S) was assumed to be equal to the complex conjugate of the free space radiation impedance (Z_S= 102.14+ j83.78Ω). The source voltage (V_S) was chosen to obtain a radiated power in free space equal to 600 mW ($V_S = \sqrt{0.6.8.R_{R0}}$). When analyzing the effect of

the metamaterials and the human head on the antenna performance, the source impedance and source voltage were fixed at the Z_S and V_S values. The power radiated from the antenna was evaluated by comparing the radiation impedance in this situation ($Z_R = R_R + jX_R$) and used the following /19/ equation:

$$P_R = \frac{1}{2} V_S{}^2 \frac{R_R}{\left|Z_R + Z_S\right|^2}$$

(5)

The total power absorbed in the head was calculated by

$$P_{abs} = \frac{1}{2} \int_V \sigma \left|E\right|^2 dv$$

(6)

Table 4: Effects of metamaterial on antenna performances and sar reduction at 900 mhz

	$Z_R (\Omega)$	P_R (mW)	P_{abs} (mW)	SAR 1 gm (W/Kg)
Without material	63.39+j94.53	600	268.83	2.002
$\mu = 1$, $\varepsilon = -3$	51.93+j99.79	514.6	211.95	1.0897
$\mu = 1$, $\varepsilon = -5$	54.12+j95.25	532.8	238.45	1.5635
$\mu = 1$, $\varepsilon = -7$	59.25+j96.14	541.9	251.34	1.732

Different negative medium parameters for SAR reduction effectiveness were analyzed. We placed negative permittivity mediums between the antenna and the human head. First, the plasma frequencies of the mediums were set to be $\omega_{pe} = 9.309 \times 10^9$ rad/s, which give mediums with $\mu = 1$ and $\varepsilon = -3$ at 900 MHz. The mediums with larger negative permittivity $\mu = 1$, and $\varepsilon = -5$; $\mu = 1$, and $\varepsilon = -7$ were also analyzed. We set $\Gamma_e = 1.2 \times 10^8$ rad/s, suggesting the mediums have losses. Numerical results of SAR value and antenna performance are given in Table IV. The peak SAR 1 gm becomes 1.0897 W/kg with $\mu = 1$ and $\varepsilon = -3$ mediums. Compared to the condition without metamaterials, the radiated power is reduced by 13.9% while the SAR is reduced by 53.35%. With the use of and mediums, the SAR reduction effectiveness is decreased. However, the radiated power from the antenna is less affected. Comparisons of the SAR reduction effectiveness with different positions and sizes of metamaterials were analyzed. Simulation results are shown in Table V. In case 1, the distance between the antenna and metamaterial was changed from 3 mm to 6 mm. In case 2, the metamaterial thickness was reduced from 6 mm to 3 mm. It is found that both the peak SAR 1 gm and power absorbed by the head increase with the increase of distance or the decrease of thickness. In case 3, the size of the metamaterial was increased from 48 mm X 48 mm to 56 mm X 56 mm. It can be noted that the peak SAR 1 gm is reduced significantly while the dreadful conditions on the radiated power due to metamaterial is insignificant. To further examine whether the metamaterial affected the antenna performance or not, the radiation pattern of the PIFA antenna with the $\mu = 1$ and $\varepsilon = -3$ metamaterial was analyzed.

The use of metamaterials was also compared with other SAR reduction techniques. A PEC reflector and a ferrite material are commonly used in SAR reduction. The PEC

Table 5: Effects of sizes and positions of metamaterial on antenna performances and sar values

	$Z_R (\Omega)$	P_R (mW)	P_{abs} (mW)	SAR 1 gm (W/Kg)
Without material	63.39+j94.53	600	268.83	2.002
$\mu = 1$, $\varepsilon = -3$	51.93+j99.79	514.6	211.95	1.0897
Case 1	58.37+j95.35	539.4	253.53	1.6105
Case 2	62.19+j96.86	557.2	258.74	1.6893
Case 3	69.15+j107.38	573.33	216.83	1.2346

reflector and ferrite sheet were analyzed. The relative permittivity and permeability of the ferrite sheet were $\varepsilon = 7.0-j0.58$ and $\mu = 2.83-j3.25$, respectively. Numerical results are shown in Table VI. A PEC placed between the human head and the antenna is studied. It can be found that the peak SAR 1 gm is increased with the use of a PEC reflector. This is because the EM wave can be induced in the neighbor of a PEC reflector due to scattering. When the size of PEC sheet is small compared to the human head, the head will absorb more EM energy. Similar results of peak SAR increase with PEC placement were also reported in /14/. The use of a ferrite sheet can reduce the peak SAR 1 gm effectively. However, the degradation on radiated power from the antenna is also significant. In addition, compared to the use of a ferrite sheet, the metamaterials can be designed on the circuit board so they may be easily integrated to the cellular phone.

Table 6: Comparisons of sar reduction techniques with different materials

	$Z_R (\Omega)$	P_R (mW)	SAR 1 gm (W/Kg)
$\mu = 1$, $\varepsilon = -3$	51.93+j99.79	514.6	1.0897
PEC reflector	66.83+j32.23	509.3	4.6803
Ferrite sheet	169.33+j153.69	519.3	1.043

To study the effect of SAR reduction with the use of metamaterials, the radiated power from the PIFA antenna with $\mu = 1$ and $\varepsilon = -3$ mediums was fixed at 600 mW. Numerical results are shown in Table VII. It is found that calculated SAR value at 900 MHz, without the metamaterial, is 2.002 W/kg for SAR 1 gm and with the metamaterial, the reduction of the SAR 1 gm value is 1.1917 W/kg. The reduction is 41.47%.

Table 7: Effects of comparisons with metamaterials on sar reduction ($p_r = 0.5$ w for 900 mhz)

	900MHz	
	Without material	$\mu = 1$, $\varepsilon = -3$
SAR 1 gm value for /14/ SAR 1 gm value in this work	2.43 2.002	1.89 1.1917

From simulation results, the metamaterials can reduce peak SAR effectively and the antenna performance can be less affected. The metamaterials are resonant due to internal capacitance and inductance. The mediums will display a stop band with a single negative medium parameter. Besides, we need to be more careful in taking the square root of negative

μ and ε of metamaterial. For example, instead of writing, ε = -3 we write ε = 3 exp (iπ). When the mediums with μ = 1 and ε = -3 are studied, the propagation constant becomes

$$\beta = \omega\sqrt{\mu\varepsilon\mu_0\varepsilon_0} = \omega\sqrt{3\mu_0\varepsilon_0} \times \exp(i\pi/2) = \omega\sqrt{3\mu_0\varepsilon_0} \quad (7)$$

The propagation constant is imaginary and the fields inside the metamaterials will fall off exponentially with the distance from the surface. Fig. 9 shows the simulated SAR distribution for an optimal metamaterial.
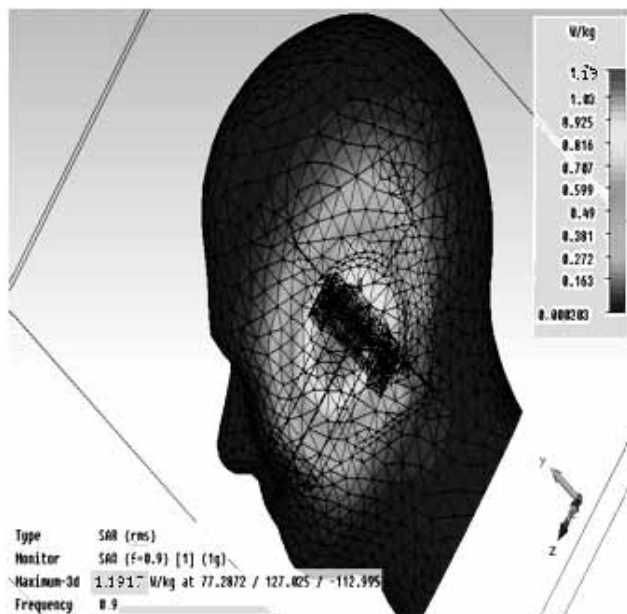
Fig. 9.   SAR distributions after reduction using the metamaterial.

This work has achieved 41.47% of SAR reduction whereas the design reported in /14/ achieved 22.63% respectively. This is achieved due to the consideration of different density, different antenna, different size of metamaterial, different type of conductivity and it is because the electromagnetic source is being moved away from the head.

4.   Conclusions

The EM absorption between an antenna and the human head with metamaterials has been discussed in this paper. Utilizing metamaterial in the phone model a SAR value is achieved of about 0.693 W/kg for SAR 10 gm and 1.1917 W/kg for SAR 1 gm is achieved. Based on the 3-D FDTD method with lossy-Drude model, it is found that for the both cases of peak SAR 1 gm and SAR 10 gm of the head can be reduced by placing metamaterials between the antenna and the human head. Numerical results can provide useful information in designing communication equipment for safety compliance.

Acknowledgement

References

/1/   Report of Telecommunications Technology Council for the ministry of Posts and Telecommunications, Deliberation no. 89, "Radio-Radiation Protection Guidelines for Human Exposure to Electromagnetic Fields," Tokyo, 1997.

/2/   K. S. Kunz and R. J. Luebbers, "The finite difference time domain method for electromagnetic," Boca Raton, FL, CRC, 1993.

/3/   IEEE C95.1-2005. "IEEE Standards for safety levels with respect to Human Exposure to Radio Frequency Electromagnetic fields,3KHz to 300GHz," Institute of Electrical and Electronics Engineers, Inc. New York, NY 2005.

/4/   International Non-Ionizing Radiation Committee of the International Radiation Protection Association, "Guidelines on Limits on exposure to radio frequency electromagnetic fields in the frequency range from 100KHz to 300GHz," Health Physics, vol.54 no. 1, pp. 115-123, 1988.

/5/   A. Hirata, T. Adachi, and T. Shiozawa, "Folded loop antenna with a reflector for mobile handsets at 2.0 GHz," Microwave Opt. Technol, Lett., vol.40, no.4, pp. 272-275, Feb. 2004.

/6/   A. Erentok, P. L. Luljak, and R. W. Ziolkowski, "Characterization of a volumetric metamaterial realization of an arti cial magnetic conductor for antenna applications," IEEE Trans. Antennas Propag., vol. 53, pp. 160–172, Jan. 2005.

/7/   J. Wang and O. Fujiwara, "FDTD computation of temperature rise in the human head for portable telephones," IEEE Trans. Microwave Theory Tech., vol. 47, no. 8, pp. 1528-1534, Aug.1999.

/8/   S. Curto, P. McEvoy, X. L. Bao, and M. J. Ammann, "Compact patch antenna for electromagnetic interaction with human tissue at 434 MHz," IEEE Trans. on Antennas and Propagation, vol. 57, no. 9, Sep. 2009.

/9/   J. Wang and O. Fujiwara, "Reduction of electromagnetic absorption in the human head for portable telephones by a ferrite sheet attachment," IEICE Trans. Commun., vol. E80b, no. 12, pp. 1810-1815, Dec. 1997.

/10/   K Kiminami, T Iyama, T Onishi, and S Uebayashi, "Novel specific absorption rate (SAR) estimation method based on 2-D scanned electric fields," IEEE Trans. on Electromagnetic Compatibility., vol. 50, no. 4, Nov. 2008.

/11/   R. G. Vaughan, and N. L. Scott, "Evaluation of Antenna Configurations for Reduced Power Absorption in the Head," IEEE Trans. On Vehicular Technology, vol. 48, no. 5, Sep. 1999

/12/   C. H. Li, N. Chavannes, and N. Kuster, "Effects of hand phantom on mobile phone antenna performance," IEEE Trans. On Antennas and Propagation, vol. 57, no. 9, Sep. 2009.

/13/   O. Kiverkas, J. Ollikainen, T. Lehtiniemi, and P. Vainikainen, "Bandwidth, SAR, and efficiency of internal mobile phone antennas," IEEE Trans. on Electromagnetic Compatibility., vol. 46, no. 1, Feb. 2004.

/14/   J. N. Hawang and Fu-chiarng chen. "Reduction of the peak SAR in the Human Head with Metamaterials" IEEE Trans. on antenna and propagation vol. 54 (12) 3763-3770, Dec. 2006.

/15/   L. C. Fung, S. W. Leung, and K. H. Chan, "Experimental study of SAR reduction on commercial products and shielding materials in mobile phone applications," Microwave and Optical Technology Letters, vol. 36, no. 6, pp. 419-422, March. 2003.

/16/   J. B. Pendry, A. J. Holen, D. J. Robbins, and W. J. Stewart, "Magnetism from conductors and enhanced nonlinear phenomena," IEEE Trans. Microwave Theory Tech., vol. 47, no. 11, pp. 2075–2084, Nov. 1999.

/17/   D. R .Smith, et al, "Composite medium with simultaneously negative permeability and permittivity," phys. Rev. Lett., vol. 84, no. 18, 4184-4187. , 2000.

/18/ G.F. Pedersen and J.B. Andersen, "Integrated antennas for hand-held telephones with low absorption", Proc. 44th IEEE Veh. Tech. Conf., Stockholm, Sweden, June. 1994, pp. 1537-1541.

/19/ R. Y. S. Tay, Q. Balzano and N. Kuster, "Dipole configuration with strongly improved radiation efficiency for hand-held transceivers", IEEE Trans. Antennas Propagat., vo1. 46, no. 6, pp. 798-806, June. 1998.

/20/ C .M .Kuo. and C. W. Kuo, "SAR distribution and temperature increase in the human head for mobile communication," in IEEE-APS Int. Symp. Dig., Columbus, OH, 2003, pp. 1025-1028

/21/ R. W. Ziolkowski, "Design, fabrication, and testing of double negative metamaterials," IEEE Trans. Antennas Propag., vol. 51, no. 7, pp. 1516–1529, Jul. 2003

/22/ D. R. Smith, D, R and Kroll, N. "Negative refractive index in left handed materials," phys. Rev. Lett., 85-14, 2933-2936, 2000

/23/ B. B. Beard, W. Kainz, T. Onishi, T. Iyama, S. Watanabe, O. Fujiwara, J. Wang, G. Bit-Babik, A. Faraone, J. Wiart, A. Christ, N.Kuster, A. Lee, H. Kroeze, M. Siegbahn, J. Keshvari, H. Abrishamkar, W. Simon, D. Manteuffel, and N. Nikoloski, " Comparisons of computed mobile phone induced SAR in the SAM phantom to that anatomically corrects model of the human head," IEEE Transaction on Electromagnetic Compatibility, vol. 48, no.2, pp 397-407, 2006.

/24/ M. M. Sigalalas ,C. T. Chan ,K .M. Ho ,and Soukoulis, "Metallic photonic band gap materials," Phys. Rev. B.,vol.52, no.16, pp. 11744-11760.

/25/ N. Engheta and R. W. Ziolkowski, "A positive future for double-negative metamaterials," IEEE Trans. Microwave Theory Tech., vol. 53, no. 4, pp. 1535-1556, Apr. 2005.

/26/ D. Correia and J. M. Jin, "3-D-FDTD-PML analysis of left-handed metamaterials," Microwave Optical Technol. Lett., vol. 40, no. 3, pp. 201-205, Feb. 2004.

Mohammad Rashed Iqbal Faruque[1],
Mohammad Tariqul Islam[2],
Norbahiah Misran[1, 2]

[1]Dept. of Electrical, Electronic and Systems Engineering, Faculty of Engineering and Built Environment, Universiti Kebangsaan Malaysia, 43600 UKM, Bangi, Selangor, Malaysia.

[2]Institute of Space Science (ANGKASA), Universiti Kebangsaan Malaysia, 43600 UKM, Bangi, Selangor, Malaysia.

rashedgen@yahoo.com,
titareq@yahoo.com,
bahiah@vlsi.eng.ukm.my

DESIGN AND DEVELOPMENT OF COMPACT MICROSTRIP ANTENNAS FOR PORTABLE DEVICE APPLICATIONS

[1]Ahmed Toaha Mobashsher, [2]Mohammad Tariqul Islam, [1]Norbahiah Misran

[1]Dept. of Electrical, Electronic and Systems Engineering, Universiti Kebangsaan Malaysia, Bangi, Selangor, Malaysia
[2]Institute of Space Science (ANGKASA), Universiti Kebangsaan Malaysia, Bangi, Selangor, Malaysia

Key words: HCASA, SSA, COMPACT ANTENNA, portable device applications

Abstract: During the last decade, wireless communication system developments have been a major motivator of compact antenna research, most particularly for portable device applications. This paper addresses to a development procedure of designing compact antennas. By a careful observation at the current distribution and folding of slots after calculating the resonating slot length, the compactness of microstrip antenna can be achieved. Two compact slot antennas, namely hollow central annular slot antenna (HCASA) and spiral slot antenna (SSA) are designed and prototyped for validation, where the experimental result agrees well the simulation. The overall volume of these antennas are respectively $0.11\lambda_o \times 0.11\lambda_o \times 0.005\lambda_o$ and $0.08\lambda_o \times 0.08\lambda_o \times 0.005\lambda_o$ where λ_o is the free space operating wavelength, that concludes the reduction of 75 and 86.2% of antenna volume comparing that of an ordinary annular slot antenna operating at the same frequency.

Načrtovanje in razvoj kompaktnih mikrostrip anten za uporabo v prenosnih napravah

Kjučne besede: HCASA, SSA, kompaktna antena, uporaba za prenosne naprave

Izvleček: Razvoj brezžičnih komunikacijskih sistemov je v zadnjem desetletju bil glavna gonilna sila razvoja kompaktnih anten večinoma za uporabo v prenosnih naprav. V članku je opisan postopek razvoja načrtovanja kompaktnih anten do katerih pridemo z analizo tokovne porazdelitve ter rezonančne dolžine in položaja rež. Načrtali in probali smo dva tipa kompaktnih anten z režami, kjer se simulacije ujemajo z eksperimentalnimi rezultati: HCASA – antena s sredinskim obročem in SSA – spiralna antena.

Prostornini teh anten so $0.11\lambda_o \times 0.11\lambda_o \times 0.005\lambda_o$ in $0.08\lambda_o \times 0.08\lambda_o \times 0.005\lambda_o$, kjer λ_o predstavlja valovno dolžino v vakumu; to pomeni zmanjšanje za 75% in 86,2 % volumna navadnih anten, ki delujejo na enaki frekvenci.

1. Introduction

In modern mobile and wireless communications systems, there is a increasing demand for compact antennas that can be easily integrated into the portable devices. In this regard, microstrip antennas are highly preferred because of their characteristics such as ease of fabrication and integration, compactness and low profile. Basically the compactness of the antenna is a trade-off between the size and the performance of the antenna due to the fact that antenna performance is bound with the fundamental limits based on the size of the antenna. This is especially true in the field of radio communications, where reducing the size of an antenna leads to smaller and light-weight systems, thereby enhancing portability and minimizing electromagnetic interference with other electronic devices.

One way for miniaturization is to alter the geometry of the antenna, such that the electrical length of the current path is increased /1/. Nevertheless, the size of microstrip patch antenna can be reduced with a dielectric of the high relative dielectric constant. But the dielectric caused the degradation of gain and radiation efficiency, thus we need to develop methods for miniaturization through the structural change of the patch.

There are some methods reported to minimize the antenna resonating at some lower frequencies. It has been shown that resonant patch antennas can be miniaturized using artificial magneto dielectrics /2/. Further compactness of these antennas has also been achieved through loading, using dielectrics, resistors, shorting pins, or meandering microstrip lines /3/. However, such loadings can increase their loss, complication or fabrication cost. In portable devices there is PIFA, IFA and printed monopole or loop antennas are very promising and widely used as compact antennas /4-6/.

However, such internal mobile antennas usually excite large surface currents on the system ground plane of the mobile phone, which functions as an effective radiation portion. An isolation distance of about $7mm$ or larger between the antenna and the nearby conducting elements or electronic components in the mobile phone is usually required to avoid large degradation effects on the performances of the internal antenna, due to the large excited surface currents

Informacije MIDEM 41(2011)2, str. 105-113

A. T. Mobashsher, M. T. Islam, N. Misran:
Design and Development of Compact Microstrip Antennas for ...

on the system ground plane, especially in the region near the internal antenna /7,8/.This is a big limitation for the portable devices.

In this paper, a design procedure of compact antennas is proposed which is based on calculating the resonating slot length. The process starts from a conventional annular ring slot antenna and ends with two proposed compact antennas. All of the antennas are designed for operation at 920 MHz. On the basis of the current distribution, it has been shown that the antenna slots can also be folded or coiled in spiral to produce lower frequencies in a low profile by maintaining almost the same slot length. However some impedance matching measures has to be taken to optimize the antennas in desired low frequencies. From the view of simplicity and compactness, these miniaturized antennas are also very prognosticating as they do not need big ground planes to provide good radiation patterns.

2. Theoretical evaluation

Slot antennas are attractive because they are easy to analyze, design and fabricate. Their radiation pattern can be bidirectional or unidirectional and is possible to have radiation at low elevation angles for an annular slot of the geometry shown in the co-ordinate system of Figure 1 in an infinite and perfectly conducting ground plane, magnetic surface current of the annular distribution can be given by

$$\vec{M}(\rho,\phi') = \vec{E}_a(\rho,\phi').\hat{n}$$

where E_a is the aperture electric field and $\hat{n}$ is the unit vector normal to the aperture.

The general equations for the-far electric field components E_θ and E_ϕ can be written as /9/

$$E_\theta = \frac{-jk}{4\pi}\frac{e^{-jkR}}{R}\int_0^{2\pi}\int_a^{a+W}\{M(\rho)\sin(\phi'-\phi) +$$

$$+ M(\phi'-\phi)\}.e^{j\rho k\sin\theta\cos(\phi'-\phi)}.\rho d\rho d\phi'$$

$$E_\phi = \frac{jk}{4\pi}\frac{e^{-jkR}}{R}.\cos\theta.\int_0^{2\pi}\int_a^{a+W}\{M(\rho)\cos(\phi'-\phi) +$$

$$+ M(\phi')\sin(\phi'-\phi)\}.e^{j\rho k\sin\theta\cos(\phi'-\phi)}.\rho d\rho d\phi'$$

where k is the free space propagation constant.

Let us consider the point of observation P is represented in the co-ordinate by R, Θ and ϕ; the inner radius of the annular slot as a; the width of the slot as W and

$$\vec{M}(\rho,\phi') = -E_\phi\,\hat{\rho} + E_\rho\,\hat{\phi}$$

where E_ϕ and E_ρ are respectively the slot electric field components in ϕ and Θ directions. For a narrow (W <<λ_0) and fixed annular slot the field component equations can be solved as
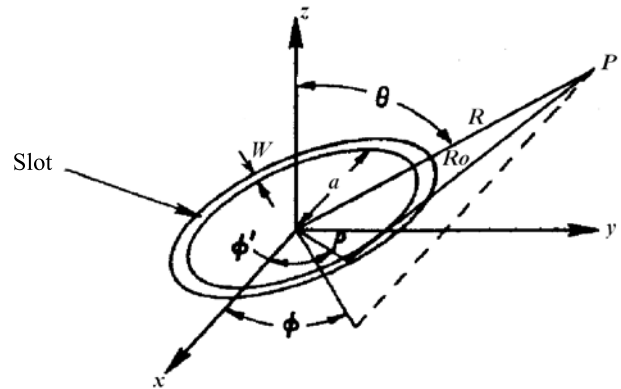
Fig. 1. Annular-slot Geometry

$$E_\theta = -j^n E_o a\frac{kW}{2}\frac{e^{-jkR}}{R}\cos n\phi.J_n'(ak\sin\theta)$$

$$E_\phi = j^n nE_o a\frac{W}{2}\frac{e^{-jkR}}{R}\sin n\phi.\cot\theta.J_n(ak\sin\theta)$$

where $J_n'(ak\sin\theta) = \dfrac{d}{d(ak\sin\theta)}J_n(ak\sin\theta)$

However, for a constant slot width and when $0.0015 \le w/\lambda_0 \le 0.075$ and $3.8 \le \varepsilon_r \le 9.8$ an approximation can be provided to obtain the guided wavelength of the resonance by using Bessel functions as /10/

$$\lambda_g = \lambda_o\left[0.9217 - 0.277\ln(\varepsilon_r) + 0.0322\left(\frac{w}{h}\right)\left(\frac{\varepsilon_r}{\frac{w}{h}+0.453}\right)^{0.5} - \right.$$

$$\left. - 0.01\ln\left(\frac{h}{\lambda_o}\right)\left\{4.6 - \frac{3.65}{\varepsilon_r^2\sqrt{w/\lambda_o}\left(9.06 - 100 w/\lambda_o\right)}\right\}\right]$$

Nevertheless, the dominant TM_{n1} mode resonant frequency, f_n of the slot antenna is determined by

$$f_n = \frac{nc}{2\pi\sqrt{\varepsilon_{eff}}\left(R_m/2\right)}$$

Here, R_m is the mean radius of the annular ring slot, n is the mode number of resonance, ε_{eff} is the relative efficiency of the slot line and c is the speed of light in free space. Usually, the resonant frequencies are mainly determined by the mean radius of the annular slot. The mean radius can be defined by $R_m = (R_i + R_0)/2$ where, R_i is the inner radius and R_0 is the outer radius of the annular ring slot.

3. Antenna miniaturization

In order to explain the miniaturization technique of the microstrip antenna using current distribution trace, a conventional annular ring slot microstrip antenna has been discussed with a center frequency of 920MHz, shown in Figure 2. The antenna is designed on FR4 substrate of ε_r = 4.4 and $tan\delta$ =0.02. The antenna dimensions are tabulated

A. T. Mobashsher, M. T. Islam, N. Misran:
Design and Development of Compact Microstrip Antennas for ...

Informacije MIDEM 41(2011)2, str. 105-113

in Table I. A symmetrical external 50Ω microstrip feeding is introduced to provide impedance matching and excite the conventional annular ring slot. As the fundamental TM$_{11}$ mode is excited the corresponding equation to determine resonance can be found as

$$f = \frac{c}{2\pi \sqrt{\varepsilon_{eff}} \left(\frac{R_o + R_i}{2} \right)}$$

It is noted that this equation is valid as long as a thin substrate is used for the annular ring antenna.

Table 1 Design parameters of the conventional annular slot antenna

L	W	R$_o$	R$_i$	SW	FW	FL	FD
70	70	33	30	3	3	16	35

(a)

b)

c)
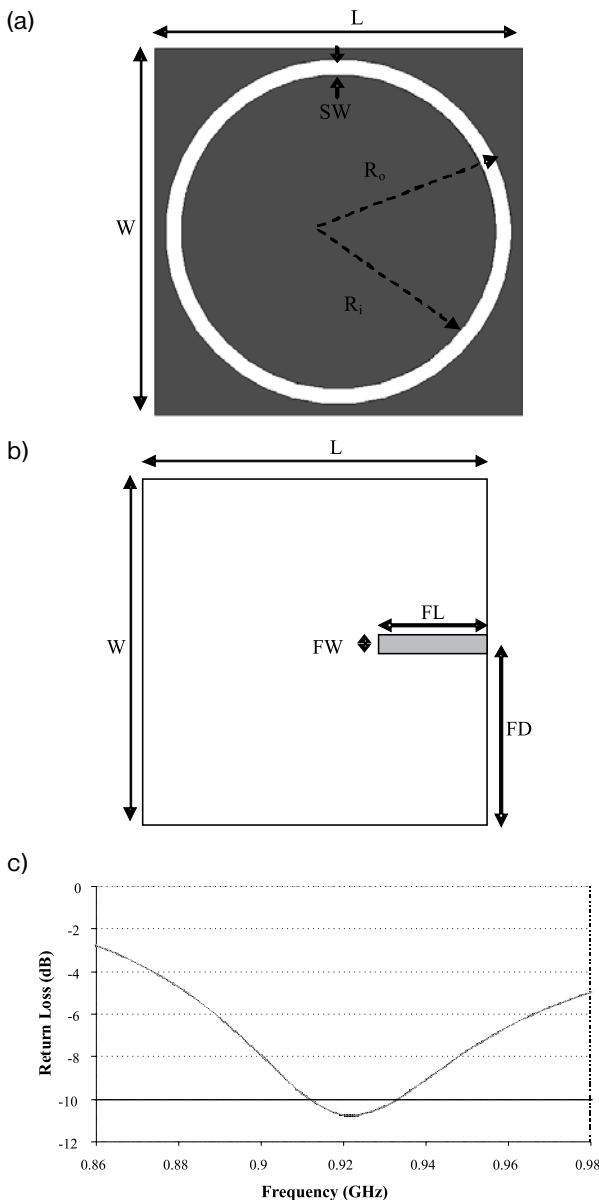
Fig. 2.   The (a) top view, (b) bottom view and (c) return loss of conventional annular slot antenna

(a)

b)
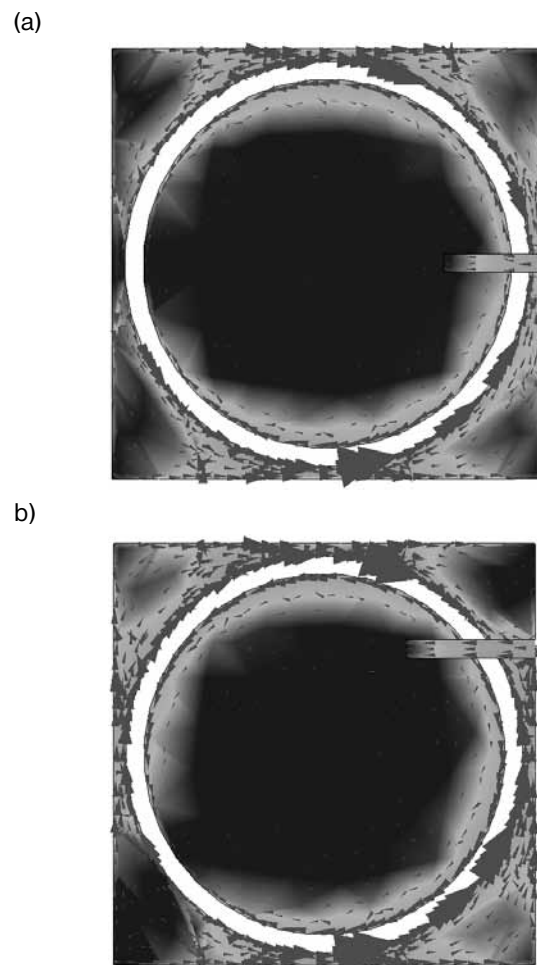
Fig. 3.   Current distribution at 920MHz of (a) conventional annular ring slot antenna and (b) annular ring slot antenna with side feeding

As presented in Figure 2(b), the antenna shows a -10 dB bandwidth of 18.2 MHz having central frequency of 920 MHz. In order to understand the effect of the antenna feeding position, the feeding is displaced from the middle to FD = 52.5 *mm*. Providing proper impedance matching by varying the feeding length, the modified antenna achieves resonance at 920MHz. As seen from the current distribution pattern of the antennas in Figure 3, at resonance frequency, the current densely flows at the edges of the annular slots, while in middle portions of the circular disks the currents are null. The current flows toward the microstrip feeding at the outside portion of the slot and at the inside portion of the slot the current traces flows from the feeding. These two traces produce null current at mean slot length of about $2\pi R_m/2 \approx 0.5\lambda_g$ where guided wavelength at resonance frequency, $\lambda_g = \lambda / \sqrt{\varepsilon_{eff}}$ and effective dielectric constant $\varepsilon_{eff} \approx \frac{(\varepsilon_r + 1)}{2} = 2.7$; which makes the current paths symmetrical to the microstrip feeding line /11/.

Shifting the antenna feeding line in the upper portion of the antenna increases current density in that region. This introduces the initial step of miniaturization, by cutting the modified antenna in the middle and taking the high

Informacije MIDEM 41(2011)2, str. 105-113

A. T. Mobashsher, M. T. Islam, N. Misran:
Design and Development of Compact Microstrip Antennas for ...

(a)   b)

c)
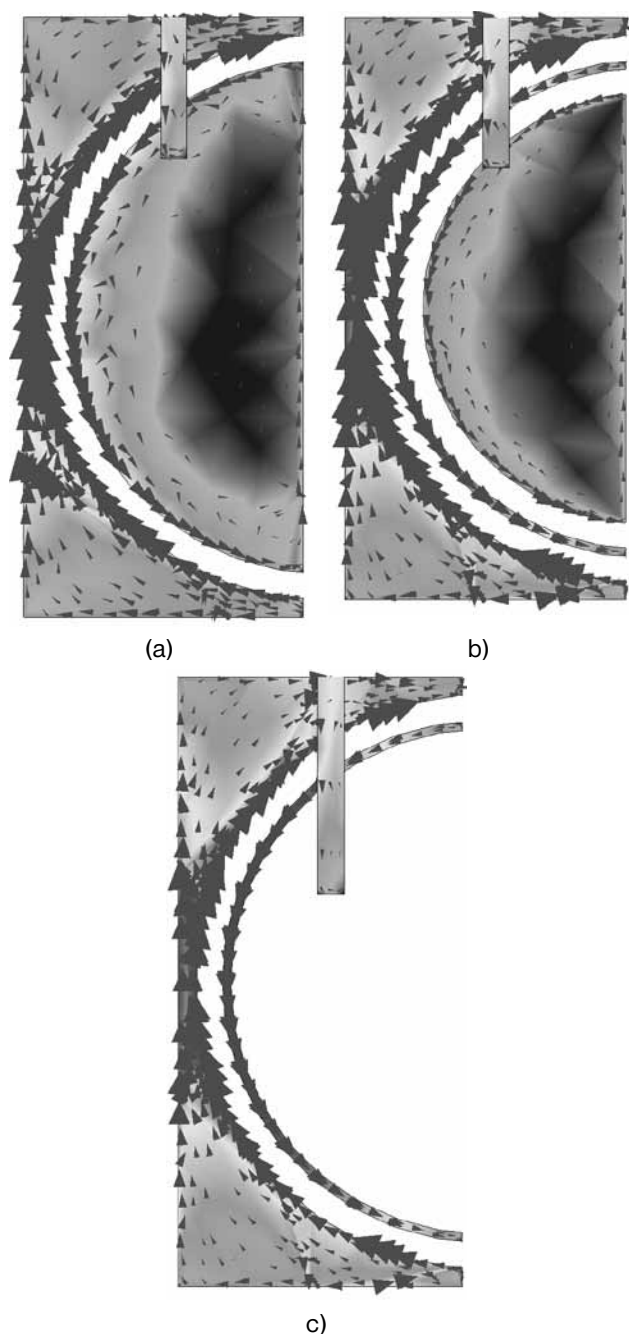
Fig. 4.   *Current distribution at 920MHz of (a) half annular ring slot antenna (b) half double annular ring slot antenna and (c) half double annular ring slot antenna without central disk*

current density portion into account, which is pictured in Figure 4(a). Moreover, in order to match the impedance accurately 2.5mm width is shorten from the half circular antenna, which makes the mean circumference of the antenna $\approx (2 \cdot \pi \cdot 31.5)/2 - 2 \cdot 2.5 \approx 0.47\lambda_g$ where λ_g is the wavelength at the slot at the resonance frequency. This resolves that the minimized slot antenna fed by a microstrip transmission line radiates as a magnetic dipole /12/. Nevertheless, it is exhibited that the current density largely flows on the two edges of the dipole like slot and in the central portion of the antenna current strength gradually decreases. So as the next step of miniaturization, shown

in Figure 4(b), another half ring slot of 2*mm* is cut on the ground plane providing 1*mm* distance between the slots. This half double annular ring slot antenna (HDARSA) also resonates at the desired frequency of 920MHz. However, this also shows null current traces in the central portion of the disk. So for the sake of miniaturization, in the next step, depicted in Figure 4(c), the half circular disk is etched from the ground and it was observed that the current distribution remains almost similar. However, the length of feeding line is extended for better impedance matching in the resonating frequency. In the following sections two miniaturized antennas are proposed and their optimization process is presented and discussed.

4.   Proposed geometry description

The configurations of the two compact microstrip slot antennas are illustrated in Figure 5. Both of the antennas are designed on a low cost substrate, FR4 of height $h_s = h_c$ =1.6*mm* with relative permittivity ε_r = 4.4 and loss tangent $tan\delta$ =0.02. The first antenna is a hollow central annular slot antenna (HCASA), which consists of an annular slot with the central portion etched out from the ground of antenna. And second spiral slot antenna (SSA) having an optimized spiral slot in the ground plane. Both of the antennas are fed by 50Ω microstrip lines, which give suitability for the antennas to embed with the circuit boards. The antenna design parameters of the microstrip-fed miniaturized antennas are given in Table II. In Table III the comparative volume of the miniaturized antennas are also mentioned.

(a)   b)

(c)   d)
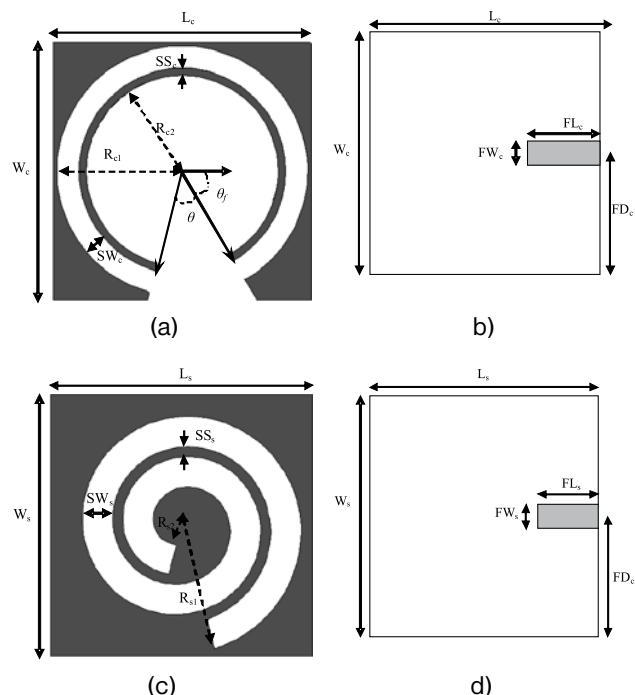
Fig. 5.   *Structure of proposed hollow central annular slot antenna (HCASA) top and side view (a & b), spiral slot antenna (SSA) top and side view (c & d)*

A. T. Mobashsher, M. T. Islam, N. Misran:
Design and Development of Compact Microstrip Antennas for ...

Informacije MIDEM 41(2011)2, str. 105-113

Table 2: Design parameters of the miniaturized antennas

Hollow Central Annular Slot Antenna (HCASA)	L_c	W_c	R_{c1}	R_{c2}	SW_c	SS_c	FW_c	FL_c	FD_c	θ	θ_f
	35	35	17	14	3	1	3	10	17.5	45	60

Spiral Slot Antenna (SSA)	L_s	W_s	R_{s1}	R_{s2}	SW_s	SS_s	FW_s	FL_s	FD_c
	26	26	11.7	2	3	1	3	7	13

Table 3: Comparative volume of the miniaturized antennas

	Hollow Central Annular Slot Antenna (HCASA)	Spiral Slot Antenna (SSA)
Antenna Volume (mm)	35×35×1.6	26×26×1.6
Antenna Volume Relative to the Free Space Operating Wavelength (λ_o)	0.11 λ_o ×0.11 λ_o ×0.005 λ_o	0.08 λ_o ×0.08 λ_o ×0.005 λ_o

5. Analytical study & optimization

The goal of the performed analytical parametric studies is to facilitate more elaboration of the design procedures and optimization processes for miniaturized antennas. Various parameters are investigated to examine the effects of the antenna parameters on resonant frequency, return loss as well as the impedance bandwidth of the antenna. This study covers the formulation of the antenna design, influences of varying the slot lengths on resonant frequency and return loss, the implication of choosing the separation angle for the design, the consequence of changing the offset angle for achieving the best optimized minimized antennas. For better convenience of the effect on the performance of the antenna upon changing the parameters, only one parameter is changed at a time, while keeping others unchanged.

5.1. HCASA

The mean circumference of the HCASA slot can be illustrated as, $C(\Theta) = 2\pi \cdot r - \Theta \cdot r$

Applying this equation for the designed antenna we get, for $\Theta = \pi/8$ and r = 15.5, the length $C(\Theta) = 91$. The length of the circular slot is approximately $0.46\lambda_g$, where λ_g is the wavelength at the slot at the resonance frequency. This properly corresponds to the miniaturized half circular antennas discussed previously discussed. Nevertheless, the angles for the two ends of the slots are optimized to achieve proper impedance matching for the best performance of the antenna.

Figure 6 shows the relationship between the angle of separation, Θ between the two edges of the slot with the resonant frequency and return loss at the respective frequency. It is seen that the resonant point of the antenna increases almost linearly when the angle, Θ is increased gradually. In the same time, the respective return loss does not behave so monotonously. This is because of the impedance matching of the antenna with feeding strip. In spite of the ripples we can derive a merely straight line for the relation of Θ and return loss. However it is also observed

(not shown in graph) that the bandwidth of the antenna increases with increase of the angle. The reason for this phenomenon can be attributed to the relatively electrically large aperture of the antenna as the resonance frequency also increases, having the physical dimensions of the overall patch remaining almost the same. In this design, the angle, $\Theta = 45°$ is taken as the optimized one for attaining the resonance frequency of 920MHz.
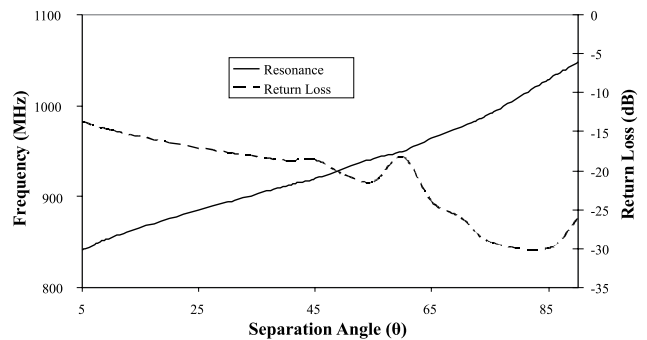
Fig. 6.   The effect of different separation angel, Θ on resonant frequency and return loss
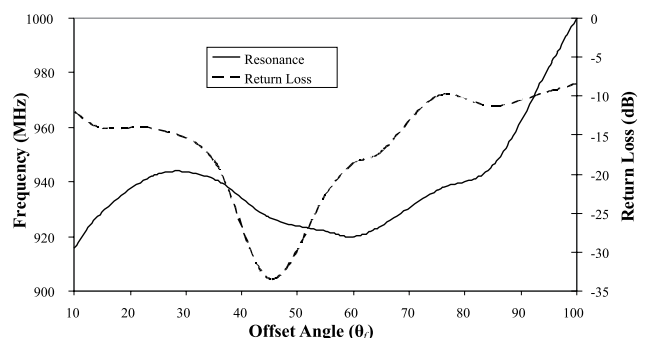
Fig. 7.   The relationship between the offset angle, Θ_f with resonance and return loss

The offset angle of the slot edge, Θ_f from the line of feeding affects the impedance matching and the resonance frequency dramatically, which is verified by the exhibited graphs of Figure 7 with different values of Θ_f angle providing other shapes and parameters unchanged. Figure 9 shows

Informacije MIDEM 41(2011)2, str. 105-113

A. T. Mobashsher, M. T. Islam, N. Misran:
Design and Development of Compact Microstrip Antennas for ...

that the antenna meets the desired resonance frequency 920MHz when $\Theta_f \approx 10°$ with a low return loss, which implies a defective impedance matching of the antenna. However the best impedance matching is achieved when $\Theta_f = 45°$ but the resonating frequency is over 920MHz. When $\Theta_f = 60°$, the resonance falls once again at 920MHz with a better impedance matching and this is taken as the optimized parameter. Nevertheless, with the increasing of when Θ_f, the resonance point still goes to higher frequencies with a gloomy return loss.

5.2. SSA

Spiral arm can be represented as /13/, $r(\varphi) = a\ \varphi + r_a$, $(\varphi_s < \varphi < \varphi_e)$

Here, $r(\varphi)$ is the radial distance from the origin to the arbitrary point on the centre line of the spiral, a is the spiral constant, φ is the winding angle, φ_s is the spiral start angle, φ_e is the spiral end angle, and r_a is the radial distance from the origin to the initial point of the spiral line.

The mean arc length of the Archimedean spiral $C(\varphi_s, \varphi_e)$ in polar coordinates between φ_s and φ_e is:

$$C(\varphi_s, \varphi_e) = a \int_{\varphi_s}^{\varphi_e} \sqrt{1 + \varphi^2}\, d\varphi \tag{1}$$

However, from calculus formula, for the simplification of a variable φ representing the angle in radians staring from $\varphi = 0$ radians and wrapping counter clockwise around pole until angle $\varphi = \varphi_e$ radians it can be derived:

$$\int_{\varphi_s}^{\varphi_e} \sqrt{1 + \varphi^2}\, d\varphi = \frac{1}{2}\left[\varphi\sqrt{1+\varphi} + \ln\left(\varphi + \sqrt{1+\varphi^2}\right) \right]_{\varphi_s}^{\varphi_e}$$

It reveals equation (1) as follows:

$$C(\varphi_s, \varphi_e) = \frac{1}{2}\left[\varphi\sqrt{1+\varphi} + \ln\left(\varphi + \sqrt{1+\varphi^2}\right) \right]_{\varphi_s}^{\varphi_e} \tag{2}$$

Where, for the proposed Archimedean spiral antenna, $\varphi_s = 1.17\pi$ and $\varphi_e = 2.56\varpi$. Solving equation (2), the length of the arc is attained as $90.91 mm$. This is also approximately corresponds to $0.046\lambda_g$, where λ_g is the guided wavelength at 920MHz. This proves that the proposed miniaturized spiral antenna slot acts like a magnetic dipole for the resonating frequency. In the next section the effect of the mean spiral length is discussed for the better understanding of the antenna geometry.

Figure 8 exhibits the relationship between the mean slot length with the resonant frequency and input impedance of the antenna. It is seen from Figure 8 that resonant frequency is a linear function of the slot length until the spiral slot meets the edge of the antenna. When the slot length crosses over 109mm, the slot can not be confined in the antenna surface; it cuts the edge of the antenna, which introduces a discontinuity to the return path of current components and acts like a monopole slot antenna and resonates at a lower frequency. However the impedance bandwidth of the antenna decreases due to the relatively low profile of the antenna at that frequency. The input impedance characteristics of the antenna are not so linear; but also do not vary rapidly as the slot length is increased. On the other hand as the Archimedean spiral slot length decreases the antenna resonance point increases following the $\approx 0.46\ \lambda_g$ approximation. In this case, the resistance of the real part and capacitive effect of the imaginary portion of the input impedance increases; which also reduces the return loss and impedance bandwidth of the antenna. The characteristics of the antenna with the varying slot length are summarized in Table V. When the slot length is about 92mm then the antenna resonates at 920MHz and shows the best impedance matching where the input reactance exhibits the highest inductance. This also results the highest -10dB bandwidth for the proposed spiral slot antenna /14/.

Table 4: Characteristics of the antenna with varying slot length

Slot Length (mm)	Resonant Frequency (MHz)	Antenna length or width (26mm) relative to free space wavelength (λ_o)	Return Loss (dB)	Bandwidth with below -10dB (MHz)	Input Impedance	
					Real (ohm)	Imaginary (moh)
77.68	1116	0.097 λ_o	-6.8	-	85.5	-57.2
79.55	1084	0.094 λ_o	-9.29	-	84.4	-32.4
81.39	1052	0.091 λ_o	-13	3	70.13	-17.81
83.24	1023	0.089 λ_o	-17.62	3.7	63.4	-6.34
85.12	994	0.086 λ_o	-26.26	4.71	55.1	-0.2
87	968	0.084 λ_o	-38.62	9.25	49.2	0.85
88.92	943	0.082 λ_o	-24.6	9.3	48.8	2.1
90.91	*920*	*0.080 λ_o*	*-16.2*	*11.2*	*46.2*	*14.5*
92.87	892	0.077 λ_o	-18.4	9.1	40.14	3.88
94.87	865	0.075 λ_o	-17.1	8.93	38.2	3.22
96.88	841	0.073 λ_o	-16.4	8.87	36.94	1.88
98.9	821	0.071 λ_o	-15.77	8.6	36.1	1.54
100.93	804	0.070 λ_o	-15.51	8.3	15	0.07
102.93	788	0.068 λ_o	-15.1	8.1	36.3	6.25
104.98	772	0.067 λ_o	-15.1	7.9	35.53	3.59
106.98	757	0.065 λ_o	-15.1	7.8	35.95	5.55
109.05	560	0.049λ_o	-24.52	6.2	45.23	-2.97
111.05	560	0.049 λ_o	-22.23	6	47.3	7.02
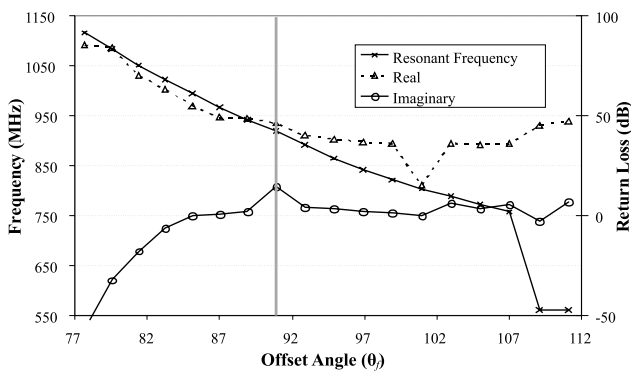
Fig. 8.   The effects of various slot lengths on
   resonant frequency and input impedance
           (real & imaginary) of SSA

6.   Results & discussions

The proposed hollow central annular slot antenna (HCASA) and spiral slot antenna (SSA) are prototyped for the verification and measured using Agilent E9362C network analyzer. It was seen that the measured results agrees the simulated results. The prototypes are shown in figure 9.

Fig. 9.   Fabricated Prototype of the designed
           antennas shown in Figure 5

The measured and simulated return losses of the proposed hollow central annular slot antenna (HCASA) and spiral slot antenna (SSA) are illustrated in Figure 10. The measured return loss curve shows that both of the proposed antennas are excited at 920MHz. HCAS antenna shows a −10 dB return-loss bandwidth of 16.2MHz (910–930 MHz) and SS antenna exhibits an impedance bandwidth of 11.2MHz (909–927GHz). The maximum return loss of -22dB and -19.5dB is obtained at the resonant frequencies of HCASA and SSA respectively. The slight degradations of bandwidth are in accordance with the well known classical fundamental limits of electrically small antennas /15/.

The E and H plane radiation patterns of the proposed HCASA and SSA at 920MHz has been shown in Figure 11. Both of the antennas produce omni-directional radiation patterns. For HCASA, in E and H-plane the cross-polarization value is below *24dBi*, while for SSA it increases to *15dBi*. This is due to the extremely low volume of the antenna with
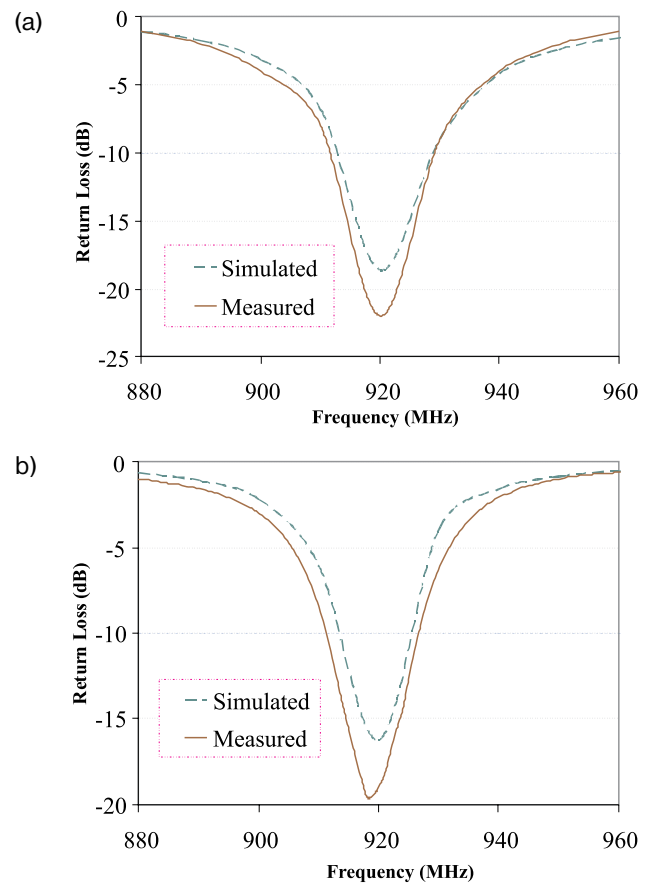
Fig. 10.   The return losses of (a) HCASA and (b) SSA
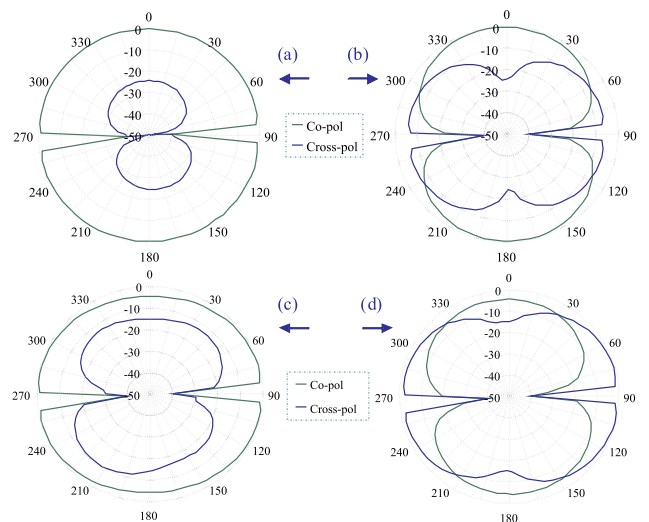
Fig. 11.   The radiation patterns of HCASA (a) E-plane,
           (b) H-plane, and SSA (c) E-plane, (d) H-plane

respect to the frequency 920MHz. For the same frequency as width, *Ws* is reduced maintaining same h_s value, W_s/h_s is increased. This results in greater surface wave to produce diffraction at the dielectric's edge, contributing to higher cross-polarization levels /16/. It can be realized that the antenna produces almost symmetrical radiation pattern. One of the significant advantages of symmetrical radiation pattern is that the maximum power direction would always be at the boresight direction and would not shift to different

Informacije MIDEM 41(2011)2, str. 105-113

A. T. Mobashsher, M. T. Islam, N. Misran:
Design and Development of Compact Microstrip Antennas for ...

directions at different frequencies. This is why the antenna is greatly suitable for portable omni-directional applications and services.
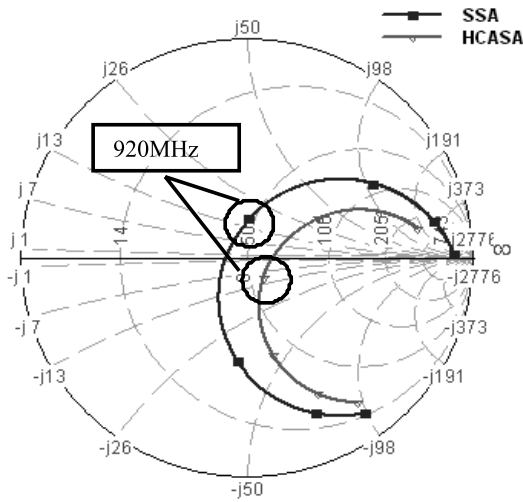
Fig. 12. *The input impedance of the miniaturized proposed antennas*

(a)   (b)
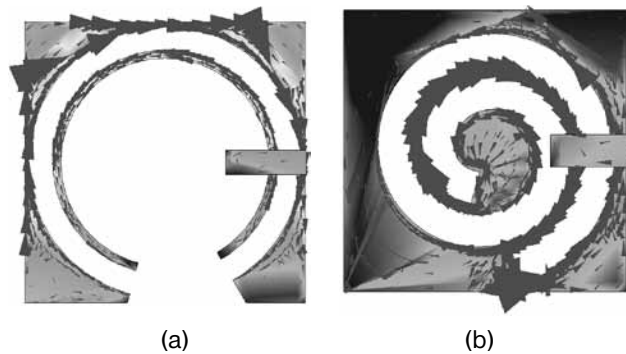
Fig. 13. *The current distribution at 920MHz of proposed (a) HCASA and (b) SSA*

The input impedance plots of the microstrip-fed minimized hollow central annular slot antenna (HCASA) and spiral slot antenna (SSA) are depicted in Figure 12. The input

impedance curves change smoothly over the operating frequency. For HCASA, at the resonance the input resistance is about 10Ω more than the SSA. However for SSA the input reactance is mainly inductive. This is for the reason of the spiral slot which acts less capacitive and provides more inductance to the antenna.

The simulated surface current distributions of the compact antennas are illustrated in Figure 13. Arrows show the direction of the current direction. As anticipated from the previous current distributions shown in Figures 3 & 4, critical current flow is observed at the edges of the annular and spiral slots. However it was observed that the current components turn into the reversed direction at the resonant frequencies than lower non-resonating frequencies. The current distributions for the lower non-resonating frequencies are not shown to reduce ingemination and complexity Moreover, at the opposite edges of the slots the currents are in contra-direction to each other.

Finally comparative characteristics of the miniaturized antennas with respect to the conventional reference antenna are provided in Table V. It is obvious from the table that the half circular antennas provide the widest -10dB bandwidths, but the antenna minimization factor is just 53.6%. On the other hand, the reduction factor of finally minimized hollow central annular slot antenna (HCASA) and spiral slot antenna (SSA) are 75 and 86.2%, which makes the antennas extremely compact with respect to the operating frequencies.

7.   Conclusion

Increasing demand for smaller size in mobile devices results in a need for effective antenna miniaturization. A technique for miniaturization of slot antennas is presented in this paper. The technique is based on the combination of two different miniaturization techniques: folding of slots and optimizing of the slots keeping the same slot length. Using these techniques, two miniaturized slot antennas, namely hollow central annular slot antenna (HCASA) and spiral slot antenna (SSA) are designed that reduces the volume up to 75 and 86.2% comparing that of an ordinary annular slot

Table 5: Comparison with conventional annular slot antenna and miniaturized antennas

Antenna	Frequency	Return Loss	-10dB return loss bandwidth (MHz)	Dielectric Constant ε_r	Area of the Antenna (mm)	Reduction of antenna area (%)
Conventional Annular Ring Slot Antenna		-10.7	18.2		70×70	Ref. (0%)
Annular Ring Slot Antenna with Side Feeding		-11.5	24.4		70×70	0%
Half Annular Ring Slot Antenna		-18.5	31.7		32.5×70	53.6
Half Double Annular Ring Slot Antenna	920MHz	-20	32.8	4.4	32.5×70	53.6
Half Double Annular Ring Slot Antenna Without Central Disk		-23.5	34.3		32.5×70	53.6
Hollow Central Annular Slot Antenna		-22	20		35×35	75
Spiral Antenna		-19.5	18		26×26	86.2

* Shaded blocks represent measured values

antenna operating at the same frequency. Considering the overall volume of the miniaturized antennas are relatively $0.11\lambda_o \times 0.11\lambda_o \times 0.005\lambda_o$ and $0.08\lambda_o \times 0.08\lambda_o \times 0.005\lambda_o$ where λ_o is the free space operating wavelength. However it is obvious from the analytical parametric study that the antenna can achieve lower frequencies with the same volume which makes the antenna more compact relatively with the resonating wavelength. It was also seen that the compact antennas provides suitable radiation patterns for portable device applications.

References

/1/ Wong, K. L., *Planar antennas for wireless communications*, Hoboken, NJ: J. Wiley and Sons, 2003.

/2/ Karkkakainen, M., and P. Ikonen, "Patch Antenna with Stacked Split-Ring Resonators as an Artificial Magneto-Dielectric Material," *Microwave and Optical Technology Letters*, Vol. 46, 554-556, 2005.

/3/ Wong, K.-L., *Compact and broadband microstrip antennas*, John Wiley & Sons, New York, 2002.

/4/ Bhatti, R.A., Y.-T. Im, and S.-O. Park, "Compact PIFA for Mobile Terminals Supporting Multiple Cellular and Non-Cellular Standards," *IEEE Transactions on Antennas and Propagation,* Vol. 57, No. 9, 2534 - 2540, 2009.

/5/ Wong, K.-L., and C.-H. Huang, "Printed Loop Antenna With a Perpendicular Feed for Penta-Band Mobile Phone Application," *IEEE Transactions on Antennas and Propagation*, Vol. 56, No. 7, 2138 – 2141, 2008.

/6/ Liu, H.-W., and C.-F. Yang, "Miniature PIFA without empty space for 2.4 GHz ISM band applications," *Electronics Letters*, Vol. 46, No. 2, 113 – 115, 2010.

/7/ Wong, K. L., S. W. Su, C. L. Tang, and S. H. Yeh, "Internal shorted patch antenna for a UMTS folder-type mobile phone," IEEE Trans. Antennas Propag., vol. 53, pp. 3391–3394, Oct. 2005.

/8/ Su, S. W. K. L. Wong, C. L. Tang, and S. H. Yeh, "Wideband monopole antenna integrated within the front-end module package," IEEE Trans. Antennas Propag., vol. 54, pp. 1888–1891, Jun. 2006

/9/ James, J.R., and P.S. Hall, *Handbook of microstrip antennas*, London, IEE - Peter Peregrinus, Ltd., 1989.

/10/ Chang, K., and L.-H. Hsieh, *Microwave Ring Circuits and Antennas*, New York: Wiley, 1996.

/11/ Zaker, R., C. Ghobadi, and J. Nourinia, "Bandwidth Enhancement of Novel Compact Single and Dual Band-Notched Printed Monopole Antenna With a Pair of L-Shaped Slots," *IEEE Transactions on Antennas and Propagation*, Vol. 57, No. 12, 3978 – 3983, 2009.

/12/ Behdad, N., and K., Sarabandi, "Slot antenna miniaturization using distributed inductive loading," *IEEE Antennas and Propagation Society International Symposium*, Vol. 1, 308 – 311, 2003.

/13/ Kim, M., H. Choo, and I. Park, "Two-arm microstrip spiral antenna for multi-beam pattern control" *Electronics Letters*, Vol. 41, No. 11, 627 – 629, 2005.

/14/ Mirza, I.O., S. Shi, C. Fazi, J.N. Mait, and D.W. Prather, "A study of loop antenna miniaturization using split ring resonators," *IEEE Antennas and Propagation Society International Symposium*, 1865 – 1868, 2007.

/15/ Delafield, C., and S. Sufyar, "A miniaturization technique of a compact omnidirectional antenna" *3rd European Conference on Antennas and Propagation*, 384 – 388, 2009.

/16/ Chen, I-F., and C.-M. Peng, "A novel reduced size edge-shorted patch antenna for UHF band applications," *IEEE Antennas and Wireless Propagation Letters*, Vol. 8, 475 – 477, 2009.

Ahmed Toaha Mobashsher, Norbahiah Misran

Dept. of Electrical, Electronic and Systems Engineering
Universiti Kebangsaan Malaysia
Bangi, Selangor, Malaysia

Mohammad Tariqul Islam

Institute of Space Science (ANGKASA)
Universiti Kebangsaan Malaysia
Bangi, Selangor, Malaysia

DUAL POLARIZED MICROSTRIP PATCH ANTENNA FOR KU-BAND APPLICATION

[1]Rezaul Azim, [2]Mohammad Tariqul Islam and [3]Norbahiah Misran

[1,3]Department of Electrical, Electronic and Systems Engineering
[2,3]Institute of Space Science (ANGKASA), Faculty of Engineering and Built Environment, Universiti Kebangsaan Malaysia, Selangor, Malaysia.

Key words: Dual-polarization, microstrip patch antenna, Ku-band, high-isolation.

Abstract: A dual polarized microstrip patch antenna is proposed for Ku-band applications. The corner chopped square patch with four bent slots is adopted in this design. The antenna has a compact structure and the total size is 15 mm × 15 mm. The result shows that the impedance bandwidth (VSWR ≤ 2) of the proposed antenna is 950 MHz (7.76%). The antenna with reduced size is also able to achieve the stable radiation performance with a maximum gain of 7.6 dBi in the operating band of 11.76 GHz to 12.71 GHz and the gain variation is about 0.8 dBi. The present design provides a maximum of -26 dB isolation level between the two ports and a stable low cross polarization level for both E- and H-planes. Details of the proposed antenna design and results are presented and discussed. The patch shows a high matching level in Ku-band and isolation elements that makes it suitable for wireless and satellite communication.

Dvojno polarizirana mikrostrip antena za Ku-frekvenčni pas

Kjučne besede: dvojna polarizacija, mikrotrakasta antena, Ku-frekvenčni pas, visoka izolacija

Izvleček: V prispevku opišemo mikrotrakasto anteno z dvojno polarizacijo za uporabo na Ku-frekvenčnem pasu. Antena ima kompaktno strukturo in je velika 15 mm x 15 mm. Rezultati kažejo pasovno širino (VSWR ≤ 2) 950 MHz (7.76%). Tako zmanjšana antena zmore stabilno sevanje z maksimalno ojačitvijo 7.6 dBi znotraj pasovne širine med 11.76 GHz do 12.71 GHz in stabilnostjo ojačitve znotraj 0.8 dBi. Trenutna zasnova omogoča maksimalno izolacijo med stopnjama -26dB in stabilno nizko križno polarizacijo med E in H ravnijo. V članku so opisane podrobnosti in rezultati predlagane zasnove antene.

1.   Introduction

Dual polarized microstrip patch antennas excite two orthogonal modes, which generate vertically polarized electric field and horizontally polarized electric field. Therefore, dual polarized antennas added information by providing two co-polarizations and two cross-polarizations. These antennas reduce side effects of multi-path fading and increase channel capacity per frequency in many applications. Microstrip patch antennas have good potential for making dual-polarized antennas due to their several attractive features including low profile, light weight, low cost and compatibility with integrated circuit technology. Microstrip patch antennas have been widely used in high performance satellite and wireless communication. Several works have been reported to overcome drawbacks of the conventional microstrip antenna such as low efficiency and narrow bandwidth. The main problem of the dual polarized antenna is that two input ports may be coupled to each other to an undesired level. This coupling affects the performance of the antenna and may reduce the impedance bandwidth and deteriorate the radiation patterns for each polarization. The task is more complicated when it is required to achieve wide bandwidth with highly isolated dually polarized antennas. Several solutions have been proposed to achieve the dual polarized antenna with wide bandwidth, high isolation, and low cross polarization level. One of the most common solu-

tions consists of using off-set slots /1-2/. Other solutions using two feeding points in one or two slots and crossing slots /3/ or having crossing slots and lines in different layers /4/ have been reported. The various feeding techniques include mixture of the aperture coupled feed and capacitive coupled probe feed /5-7/, proximity coupled feed /8/ and L-shape probe feed without shorted patch /9-10/, all of which have been proposed to improve the isolation of the dual-polarized antenna with wide bandwidth. Chiou *et al.* demonstrated a high isolation patch antenna at L-band by utilizing two in-phase aperture-coupled feeds at port 1 and two out-of-phase gap-coupled probe feeds at port 2. Chiou and Wong /6/ demonstrated an isolation of 40 dB between the two ports. Haneishi *et al.* presented better than 30 dB port isolation performances at 5 GHz using dog-bone slots /11/. The antenna proposed by Mariano Barba /12/ achieved a bandwidth of 24% with a port isolation of 36 dB. Despite the excellent performances, however, these structures require multi-layer structures which increase the complexity. In this work, a simple feeding structure for a planar patch antenna is presented by employing a coaxial probe feed.

In general, the design of a patch having high isolation results in antennas with narrow bands or high values for return losses (RL). For example, the antennas presented by Ghorbani and Waterhouse /4/ shows high values of

matching level (RL< -10dB) and isolation. This matching level is useful for many applications such as wireless communication and airborne-based synthetic aperture radar. Besides, the solution proposed in /4/ uses two layers for the input signals, while the antenna has the input lines in the same layer of the same board. The use of two layers increases the complexity and mainly the cost since, it is know, RF substrates and etching drive to ones of the most important contributions in the antenna cost.

In this paper, we demonstrate that a slot-loaded microstrip patch antenna with a group of four symmetrical bent slots can perform excellent dual-polarized radiation, while the antenna size is signi cantly reduced. The four symmetrical triangular slots are aligned in parallel with the patch's diagonal for obtaining 0^0 and 90^0 polarizations, and the two polarizations are excited by using two probe feeds. Due to the perturbation of the bent slots, the excited patch surface current paths are meandered, which results in the same lowering of the operating frequencies for the two polarizations. That is, dual-polarized radiation can be obtained with a reduced antenna size at a xed operating frequency. The square patch is chosen due to its simplicity of fabrication. The coaxial probe feed is used because it is easy to match impedance and has low spurious radiation.

2. Antenna design

The geometry of the proposed dual polarized bent slot corner chopped square microstrip patch antenna is shown in fig.1.
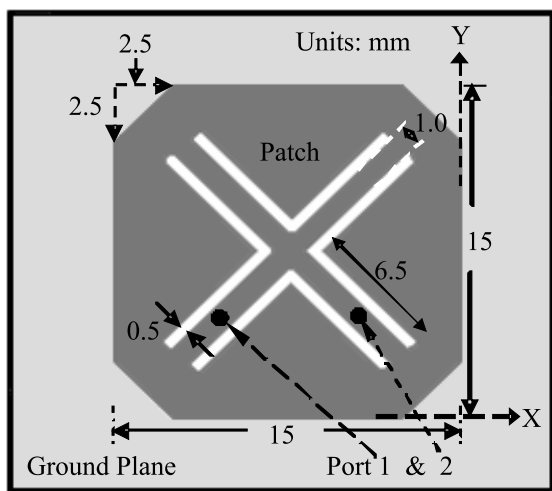

Fig.1: Geometry of the proposed antenna

The design procedure starts with the determination of sidelength of the patch using the classical equations /13/:

$$W = \frac{c}{2f_o}\sqrt{\frac{\varepsilon_r + 1}{2}}$$

(1)

$$L = \frac{c}{2f_o\sqrt{\varepsilon_e}} - 2\Delta l$$

(2)

where W is the width and L is the length of the patch, f_o is the center target frequency, c is the speed of light in vacuum. The effective dielectric constant can be calculated by the equation

$$\varepsilon_e = \frac{1}{2}(\varepsilon_r + 1) + \frac{1}{2}(\varepsilon_r + 1)\sqrt{\left(1 + \frac{10h}{W}\right)}$$

(3)

where ε_r is the relative dielectric constant and h is the thickness of the substrate. Due to the fringing field around the periphery of the patch, the antenna electrically looks larger than its physical dimensions. The increment to the length, Δl due to fringing field can be express as:

$$\Delta l = 0.412h \frac{(\varepsilon_e + 0.3)\left[\frac{w}{h} + 0.8\right]}{(\varepsilon_e - 0.258)\left[\frac{w}{h} + 0.8\right]}$$

(4)

Considering the requirements of design such as bandwidth and dielectric constant, the antenna is initially designed to operate in Ku band and consequently optimized to obtain the most efficient size of the patch using method of moments based full wave electromagnetic simulator IE3D.

The whole radiating element of the proposed dual-polarized corner chopped square patch microstrip antenna is centered on the top of a ground plane of 40mm × 40mm. The patch has a side length of 15mm and is directly printed on RT 5880 microwave substrate material of thickness 1.5748mm, relative permittivity 2.2 and tangent loss 0.009 to reduce the cost. The radiating patch is truncated with a truncation of 2.5 mm × 2.5 mm at each corner to enhance the bandwidth. The truncated patch produces additional degenerating modes necessary for widening the bandwidth. Since a dual polarized with the same requirements is sought, the patches are squared. The four bent slots have the same dimensions and have a narrow width of 0.5mm with a length 6.5mm is parallel to the patch's diagonal. The spacing between two adjacent bent slots is 1mm. The two copper coaxial probe feeds with radius 0.2 mm for the two feeding ports are located at a distance of 6.0 mm from the patch centre and radiates ± 45^0 slanted linearly polarized waves.

The above specific shape patch for the bent slots and corner chopped square shaped patch configuration allow us to obtain a satisfactory 50 Ω impedance matching across the frequency band of interest.

3. Results

The performance of the proposed antenna has been analyzed and optimized by using commercially available method of moments based full wave electromagnetic simulator IE3D package version 12.0/14/. The simulated return loss of the proposed antenna is shown in Fig. 2. From the plot, it can be observed that the return loss of the proposed antenna is less than -10dB over frequency ranges of 11.76 -12.71

GHz (7.76%), which is in the Ku-band region. The above impedance bandwidth of 950 MHz is obtained due to proper matching and introduction of four bent slots on the design, which is higher than corresponding dual polarized microstrip antennas /15/. It resonates at 12.2 GHz. Fig. 3 shows the isolation of the proposed antenna. From the figure it is seen that, the minimum isolation is about -22.6 dB and the isolation is better than -33 dB at 13.3 GHz. At the resonance frequency of 12.2 GHz the isolation is about -22.6 dB. It can be observed that at lower and higher frequencies, the isolation is higher but the isolation at middle frequencies has a little degradation. However, throughout the frequency range from 11.76 to 12.71 GHz, the isolation is still better than -22.6 dB. The return loss and high port isolation characteristics of this dual-polarized patch antenna are very suitable for being used in many practical applications such as wireless communication.
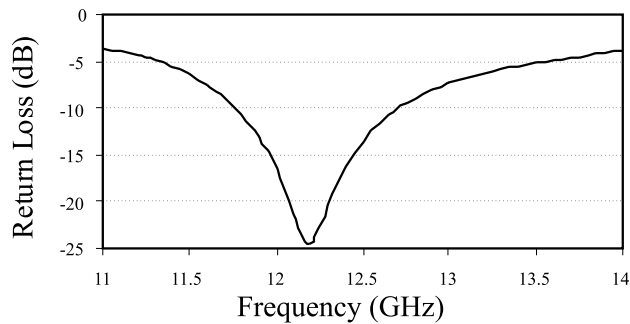
Fig.2:   *Return loss of the proposed antenna*
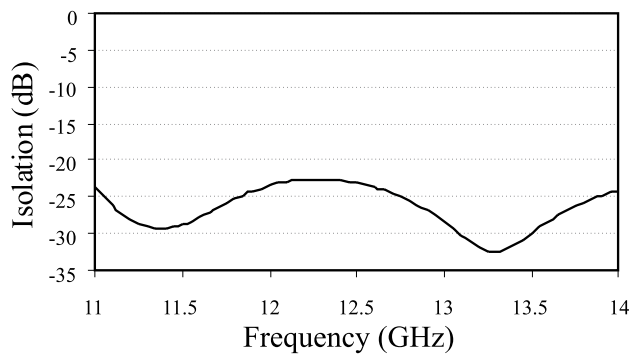
Fig.3:   *Port isolation of the proposed antenna*

The maximum gain and maximum directivity of the antenna are shown in the fig. 4 and fig. 5 respectively. The antenna exhibits the gain of more than 6.15 dB_i over the band of 11.76-12.71 GHz with a peak gain of 7.6 dB_i at 12 GHz. At resonance frequency of 12.2 GHz the observed gain is 7.58 dB_i and the gain variation across the operating band is about 0.8 dBi. Although the size of proposed antenna is reduced by 75%, the gain is remain higher compared to that of the corresponding unslotted dual polarized antennas.

The directivity of the proposed antenna varies from 7.78 to 9.36 dB_i which has a value of 9.32 dB_i at the center frequency of 12.5 GHz.

Figure 6a and b show the radiation pattern for E-plane and H-plane of the proposed antenna at resonance frequency of
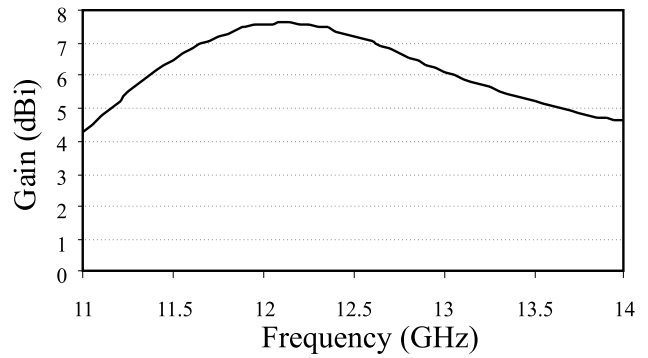
Fig. 4:   *Gain of the proposed antenna*
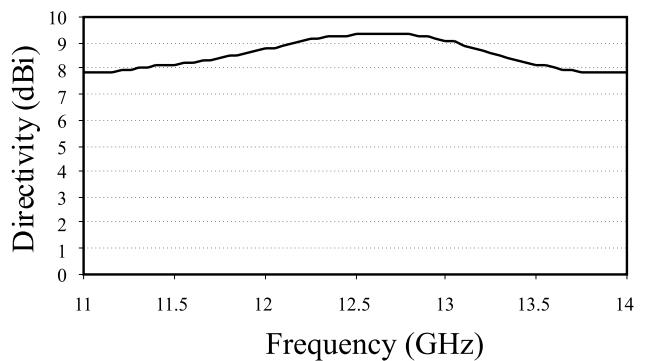
Fig. 5:   *Directivity of the proposed antenna*

12.2 GHz. The co-polarization patterns are symmetric and the cross-polarization levels in E- and H-plane are better than -12 dB and -18 dB respectively. Broad beam width is observed in the main beam of co-polarization (E-Plane). The beamwidth of 3-dB is more than 65⁰. It can be easily observed from the radiation pattern that the designed antenna produces bidirectional radiation and almost stable radiation pattern throughout the whole operating band with low cross polarization. There are some significant advantages if a patch antenna has a stable and symmetrical radiation pattern. One of the major advantages is that during construction of an antenna array, the radiation pattern would be more stable across the operating bandwidth.

The current distribution on the patch at resonance frequency of 12.2 GHz is depicted in fig. 7. Arrow sign indicates the direction of current. From the current distribution display, it is observed that the electric current strongly flows at the edge of the bent slots especially near the feeding probes of the patch. This indicates that the slots dominate the antenna performance. The current flow is restricted due to the bent slots which leads the reduction of cross-polarization level. However, the current distribution at different part of the patch is almost regular.

4.   Conclusions

Dual polarized microstrip patch antenna coupled to a coaxial probe feed has been demonstrated in this paper. The corner chopped square patch with bent slots and dual feeding technique makes it possible to have a bandwidth
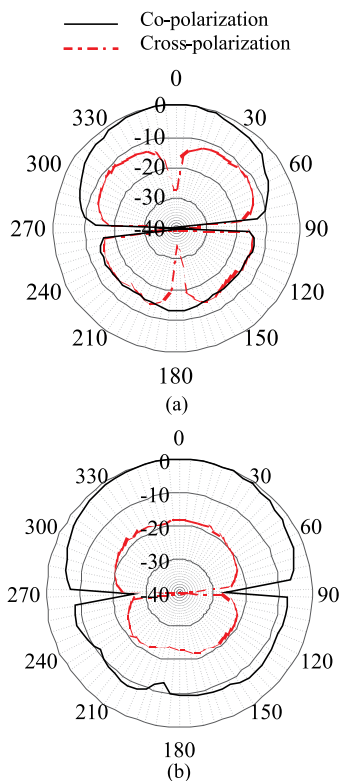
Fig.6: *Radiation pattern of the proposed antenna at 12.2 GHz (a) E-plane (b) H-plane.*
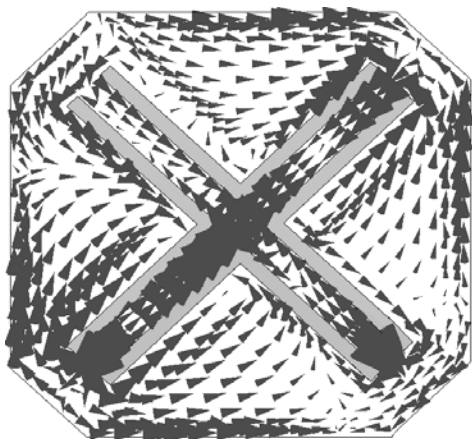
Fig.7: *Current distribution on the patch surface at 12.2 GHz.*

of 950 MHz (7.76 %) and radiation pattern at Ku-band. It covers the frequency ranges from 11.76 GHz to 12.71 GHz and provides a good isolation level between the two ports with low cross polarization levels. This antenna can be easily fabricated on substrate material due to its small size and thickness. The dual polarized patch antenna can be used for wireless and satellite communication.

Acknowledgment

References

/1/ Gao, S. C., Li, L. Wei., Leong, M. S., and Yeo, T. S., 2003. Dual-polarized slot- coupled planar antenna with wide bandwidth. IEEE Trans. Antennas Propag., 51(3): 441–448.

/2/ Padhi, S. D., Kamakar, N. C. Law, C. L. and Aditya, S., 2003. A dual polarized aperture coupled circular patch antenna using a C-shaped coupling slot. IEEE Trans. Antennas Propag., 51(12),3295–3298.

/3/ LindMark, B., 1997. A novel dual polarized aperture coupled patch element with a single layer feed network and high isolation. in Proc. IEEE Antennas Propag. Soc. Int. Symp., 4: 2190–2193.

/4/ Ghorbani, K. And Waterhouse, R. B., 2004. Dual polarized wideband aperture stacked patch antennas. IEEE Trans. Antennas Propag., 52(8): 2171– 2174.

/5/ Chiou ,T. W., Tung , H.C., and Wong, K.L., 2000. A dual-polarization wideband circular patch antenna with hybrid feeds. Microwave and Optical Technology Letters, 26(1): 37-39.

/6/ Chiou, T.W. and Wong, K.L., 2002. Broadband Dual-Polarized Single Microstrip Patch Antenna With High Isolation and Low Cross Polarization. IEEE Trans. Antennas Propagat., 50: 399-401.

/7/ Wong, K.L. and Chiou, T.W., 2002. Broad-Band Dual-Polarized Patch Antennas Fed by Capacitively Coupled Feed and Slot-Coupled Feed. IEEE Trans. Antennas Propagat., 50(3): 346-351.

/8/ Gao, S. and Sambell, A., 2005. Broadband dual-polarized proximity coupled circular patch antenna. Microwave and Optical letters, 47(3): 298-302.

/9/ Wong, H., Lau, K.L. and Luk, K.M., 2004. Design of Dual Polarized L- Probe Patch Antenna Arrays With High Isolation. IEEE Trans. Antennas Propagat., 52(1): 45-52.

/10/ Guo, Y.X., Khoo, K.W., and Ong, L.C., 2007. Wideband Dual-Polarized Patch Antenna With Broadband Baluns. IEEE Trans. Antennas Propagat., 55(1): 78-83.

/11/ Hanseishi, M. and Konno, M., 2006. Dual-polarized planar antenna fed by dog-bone slots. IEICE Transactions on Electronics, E89-C(9): 1345-1347.

/12/ Barba, Mariano, 2008. A High-Isolation, Wideband and Dual-Linear Polarization Patch antenna. IEEE Trans. Antennas Propagat., 56(5): 78-83.

/13/ Garg, R., Bhartia, P., Bahl, I. and Ittipiboon, A., 2001. Microstrip Antenna Design Handbook. Boston - London: Artech House, Inc. ISBN 0-89006-513-6.

/14/ IE3D version 12, 2006. Zeland Software, Inc., Fremont, CA, USA.

/15/ Row, J.-S., Yeh, S.-H. and Wong, K.–L., 2000. Compact Dual-Polarized Microstrip Antennas. Microwave and Optical Technol. Lett., 27(4): 284-287.

[1]Rezaul Azim, [2]Mohammad Tariqul Islam and [3]Norbahiah Misran

[1,3]Department of Electrical, Electronic and Systems Engineering
[2,3]Institute of Space Science (ANGKASA)
Faculty of Engineering and Built Environment, Universiti Kebangsaan Malaysia, 43600 UKM, Bangi, Selangor, Malaysia.
[1]rezaulazim@yahoo.com

TEMPORAL MODELING OF HUMAN ACTIVITY IN SMART HOMES

Muhammad Raisul Alam[1], Mamun Bin Ibne Reaz[2], Mohd. Alauddin Mohd. Ali[2], Salina Abdul Samad[2]

[1]Institute of Microengineering and Nanoelectronics, Universiti Kebangsaan Malaysia, Bangi, Selangor, Malaysia.
[2]Department of Electrical, Electronic and Systems Engineering, Universiti Kebangsaan Malaysia, Bangi, Selangor, Malaysia.

Key words: Smart home, Pattern recognition, Activities of daily living (ADL), Temporal Modeling.

Abstract: Recognition of human activity is a potential challenge to design an effective smart home. The paper proposed a novel algorithm to recognize activities of daily living (ADL) of the resident. It provides analysis and mathematical modeling of temporal intervals of the event. The opposite entity states are used to extract the pattern of event sequence. Each extracted episode represents a distinct task of the resident. Result shows that, the algorithm can successfully identify 135 unique tasks of different lengths with temporal characteristics. The analysis confirms that temporal pattern follows normal distribution which can be modeled by Gaussian function.

Modeliranje človeškega obnašanja v pametnih hišah

Kjučne besede: pametni dom, prepoznava vzorca, dnevne aktivnosti, časovno modeliranje

Izvleček: Prepoznava človeške aktivnosti je potencialni izziv za načrtovanje pametnih domov in hiš. Članek predstavi nov algoritem za prepoznavanje dnevnih življenjskih aktivnosti prebivalca. Omogoča analizo in matematično modeliranje časovnih intervalov posameznih dogodkov. S pomočjo posebnih algoritmov ugotavljamo časovni vzorec posameznih dogodkov. Vsak ugotovljen dogodek predstavlja specifično nalogo prebivalca. Rezultati so pokazali, da algoritem lahko uspešno prepozna 135 edinstvenih dogodkov, ki so različno dolgi. Analiza potrjuje, da časovni vzorec sledi normalni razdelitvi, ki jo lahko oblikujemo po vzoru Gaussove funkcije.

1. Introduction

Smart home research requires understanding of human behavior and reorganization of the patterns of the activities of daily living (ADL). Early projects in this area hardly try to understand psychosomatic nature of human. Those projects simply employed intelligence to the household appliance without considering psychological understanding. Projects by Mozer /1/, Vainio *et al.* /2/, Adlam *et al.* /3/, Das *et al.* /4/ suffer from these types of limitation.

Previous trends of smart home failed to achieve anticipated improvement. Recently, researchers realized that the study of human behavior should be the initial step to conduct smart home research. Current trends show that most of the recent projects are involved in identification of ADL. The House_n group at MIT developed PlaceLab to study human activities in ubiquitous environment /5/. To acquire user information, the house is occupied with numerous wire, light, pressure, temperature, water and gas sensors. The project used video and audio retrieval devices to create vast amount of real life data. The goal of the project is to study human behavior, influence of technology on the people and how technology can be utilized to simplify user interaction with the environment.

Noguchi *et al.* used a summarization algorithm to track the resident by segmenting sensory data /6/. Segments are classified by room states and summarized for activity detection. Isoda *et al.* applied C4.5 algorithm to build spatiotemporal context of the user /7/. The system used sensors and RFID tag to define task models and user behavioral pattern at any moment that is matched with the recently detected states.

Ma *et al.* utilized Case Based Reasoning (CBR) to make a context aware system /8/. CBR uses previous activities and interactions to provide the solution of current problem. De Silva *et al.* applied multimedia technology to implement an audiovisual retrieval and summarization system /9/. They used a large number of cameras to create personalized video clips by hierarchical audio clustering and video handover. The system can track people, extract key frame, localize sound source and detect lighting change.

Zheng *et al.* used self-adaptive neural network (SANN) to classify activities of daily living /10/. For the purpose, they proposed a Growing Self-Organizing Map (GSOM) based on Kohonen self-organizing map with adaptive architecture. Virone *et al.* applied statistical predictive algorithms to model circadian activity rhythms (CARs) and their deviation /11/. Zhang *et al.* proposed snow-flake data model to classify ADL from the observed pattern and temporal information /12/. The model utilized probabilistic distribution and applicable for multiple inhabitants.

```
initialize episode_database:= null
initialize window:= null
initialize window_length:= desired_episode_length

loop
        wait for the next event e
        add e to the window
        if length(window) = window_length
                If window[1]= on state and window[window_length]=opposite state of window[1] event
                        add window to the episode_database or update frequency count
                        add time interval between the states to the episode_ database
                remove window[1] and update window index
forever
```

Fig. 1:   Pseudocode of the proposed algorithm

Park *et al.* combined computer vision and RFID sensors to recognize ADL at multiple levels of detail /13/. The system builds a dynamic Bayesian network and can identify coarse-level and fine-level ADL. In 2008, Rashidi *et al.* developed CASAS at Washington State University /14/. It uses Frequent and Periodic activity miner algorithm to discover frequent and periodic activity patterns. Lu *et al.* built CoreLab, a location aware activity recognition system /15/. Instead of using simple sensors, CoreLab employs ambient-intelligence compliant objects (AICO) to detect contact, pressure, power usage and motion. It can cluster ADL by utilizing an enhanced version of naive Bayes classification method.

The major problem related to data classification algorithm is deciding the exact starting and ending point. Researchers try to solve the problem using time frame. But there is a chance to count noisy information because the time frame doesn't consider actual data flow. Others try to implement LZ78 data compression rule but it also has the same short fall. The proposed algorithm solely considers appliance states which can accurately identify ADL and temporal characteristics.

2.   Methodology

Human activity is a collection of well defined tasks. The tasks can be as simple as coffee making activity, cooking sequence, watching TV or reading books. Some consist of complex long patterns like using the kitchen, toilet and so on. Classification of the task and event according to temporal and location information is an important prerequisite to develop a reliable and sustainable smart home.

Task isolation process requires accurate clustering of unique episode. For the purpose, the actual stating point and ending point of the activities should be properly defined. In the proposed algorithm, a novel clustering method has been developed based on opposite state modeling.

Suppose, we need to identify the living room activities. The activity may be started with the turning ON of the living room light. Then the resident switched ON the TV. After watching the TV program for a while, he turned it OFF. The activity

is ended by switching OFF the living room light. Therefore, there is a specific starting point and ending point of the living room activity which are turning the living room light ON and OFF respectively. If we consider cooking activities, there also has a starting point which is turning ON the cooker. And the ending point is the OFF states of the cooker. Similarly, we can classify each and every activities of the resident by considering the ON-OFF states of home appliances.

Fig. 1 shows the pseudocode of the algorithm. It maintains a window to track the events according to the sequence of occurrence. The window is a fixed length array which is defined by the programmer according to desired episode length. The first event of the window is compared with the current event to determine the pattern. If they represent the
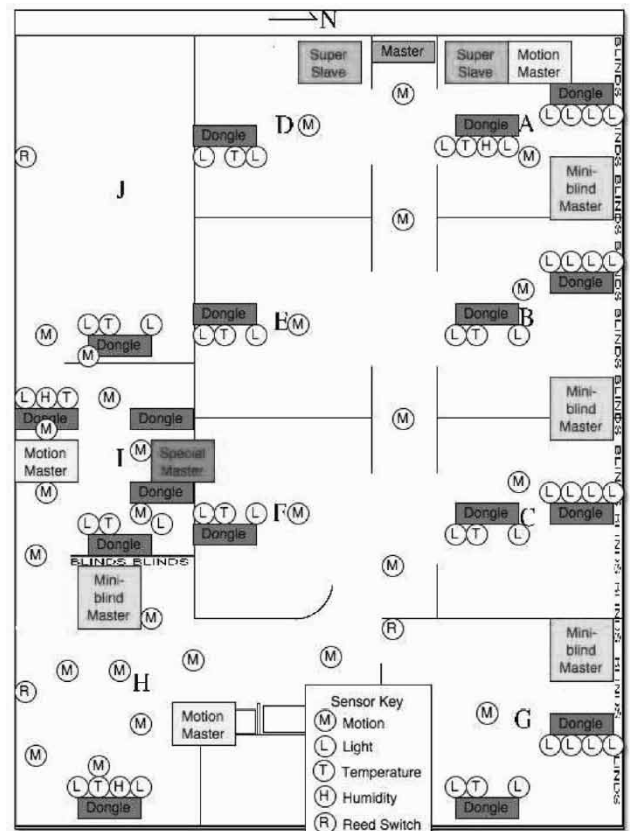

Fig. 2:   MavLab interior map and sensor locations.

opposite state of the same entity, then the whole window is added to the episode_database. In case of existing episode, the algorithm updates the frequency count. It also stores the time interval between the states into the database. The episode_database provides the classified episodes, number of their occurrence and a series of temporal intervals.

3. Results and discussion

To evaluate the algorithm, we used practical smart home date from MavHome project /16/. The project used X10 based devices for home appliance control. There are more than 60 X10 appliances which are divided into 16 zones and identified by a unique id number. Fig. 2 shows MavLab interior map and sensor locations.
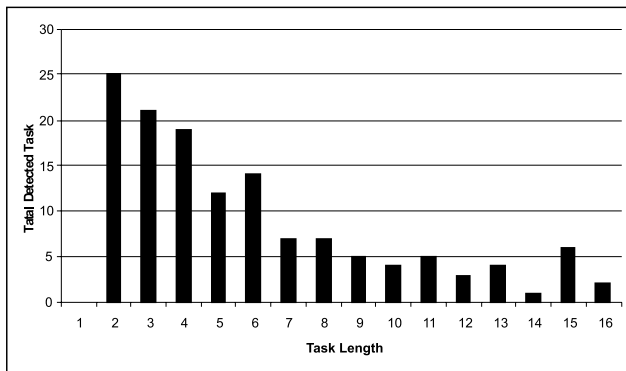

Fig. 3:   Total number of activities according to episode length.

Table 1: Temporal Analysis of Events

Event Id	Mean(s)	Median(s)	Mode(s)	Standard Deviation (s)
Event-1	60	60	60	0
Event-2	386	240	180	311
Event-3	72	60	60	27
Event-4	570	300	240	514
Event-5	600	540	none	275

The information from the X10 device has been fed into the algorithm as input and it successfully identified activities of various lengths. The lower pattern length indicates simple task and higher length represents complex activities. Fig. 3 illustrates identified patterns for various lengths. The algorithm has identified total 135 tasks. Small length activities are frequent and more than long tasks. For 2, 3,4,5,6 length episode, the algorithm can classify 25,21,19,12 and 14 distinct activities respectively. The number of total tasks reduced to less than 10 if the episode length exceeds 6 events. For example, if the episode consists of 10 events than the total activities reduce to 4. Results show that, the proposed algorithm can identify different length of activity pattern utilizing opposite state episode boundary.

The algorithm stores the temporal intervals of the event in the *episode_database*. The same event takes different duration of time. To measure central tendency of the temporal intervals, we calculated mean, median and mode of the durations. Standard deviation shows the deviation from the mean value. Table I gives an idea about temporal characteristics of the event intervals.

Temporal duration of smart home events follows normal distribution and it can be described by using Gaussian distribution function (eq. 1).

$$\varphi(x) = \frac{1}{\sigma\sqrt{2\pi}} e^{-\left[\frac{(x-\mu)^2}{2\sigma^2}\right]}$$

(1)

Here, $\varphi(x)$ is the probability density function, σ = standard deviation and μ is the mean of observed temporal data. Fig. 4 illustrates an event with σ =0.45 minute and μ =1.2 minute.
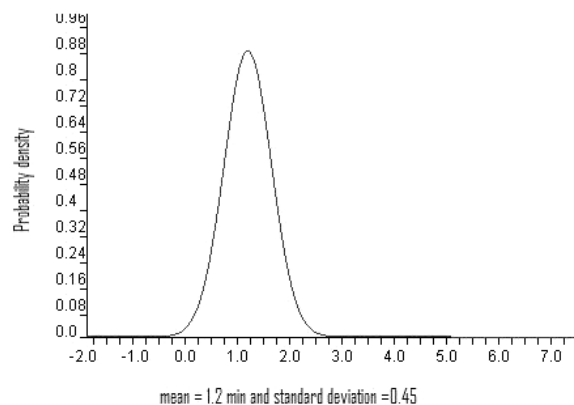
Fig. 4:   Total Temporal intervals follow normal distribution

4. Conclusions

The paper presents an innovative method to detect activities of daily living. Unlike other methods, it is based on dual state entity extraction which considers the common data flow of smart home event sequence. Result proves that, it can successfully classify 135 activities of various lengths. It provides temporal analysis and modeling of smart home user activities. Event duration follows normal distribution which can be modeled by the Gaussian function. The model can be used to predict temporal behavior of the resident.

References

/1/   Mozer, M.C. (1998) The neural network house: an environment that's adapts to its inhabitants. Proceedings of AAAI Spring Symposium on Intelligent Environments, March 23-25. Stanford University.

/2/   Vainio, A.-M., Valtonen, M. and Vanhala, J. (2008) Proactive Fuzzy Control and Adaptation Methods for Smart Homes. IEEE Intelligent System. 23(2):42 – 49.

/3/ Adlam, T., Faulker, R., Orpwood, R., Jones, K., Macijauskiene, J. and Budraitiene, A. (2004) The installation and support of internationally distributed equipment for people with dementia. IEEE Transactions Information Technology in Biomedicine. 8(3): 253–257.

/4/ Das, S.K., Cook, D.J., Battacharya, A., Heierman III, E.O. and Lin, T.-Y. (2002) The role of prediction algorithms in the MavHome smart home architecture. IEEE Wireless Communication. 9(6): 77 – 84.

/5/ Intille, S. S., Larson, K., Beaudin, J. S., Nawyn, J., Tapia, E. M. and Kaushik, P. (2005) A living laboratory for the design and evaluation of ubiquitous computing interfaces. Extended Abstracts of the 2005 Conference on Human Factors in Computing Systems, April 2-7. Portland, Oregon, USA.

/6/ Noguchi, H., Mori, T. and Sato, T. (2002) Construction of network system and the first step of summarization for human daily action in the sensing room. Proceedings of IEEE Workshop on Knowledge Media Networking.

/7/ Isoda, Y., Kurakake, S. and Nakano, H. (2004) Ubiquitous sensors based human behavior modeling and recognition using a spatio-temporal representation of user states. Proceedings of the 18th International Conference on Advanced Information Networking and Application, March 29-31. Fukuoka, Japan.

/8/ Ma, T., Kim, Y.D., Ma, Q., Tang, M. and Zhou, W. (2005) Context-aware implementation based on CBR for smart home. Proceedings of International Conference on Wireless and Mobile Computing Networking and Communications (WMOB'2005), July 28- August 01. Montreal, Canada.

/9/ De Silva, G.C., Yamasaki, T. and Aizawa, K. (2007) An Interactive Multimedia Diary for the Home. Computer. 40(5): 52 – 59.

/10/ Zheng, H., Wang, H. and Black, N. (2008) Human Activity Detection in Smart Home Environment with Self-Adaptive Neural Networks. Proceedings of IEEE International Conference on Networking, Sensing and Control, April 6-8. China.

/11/ Virone, G., Alwan, M., Dalal, S., Kell, S.W., Turner, B., Stankovic, J. A. and Felder, R. (2008) Behavioural Patterns of Older Adults in Assisted Living. IEEE Transactions on Information Technology in Biomedicine.12 (3): 387 – 398.

/12/ Zhang, S., McClean, S., Scotney, B., Hong, X., Nugent, C. and Mulvenna, M. (2008) Decision Support for Alzheimer's Patients in Smart Homes. Proceedings of 21st IEEE International Symposium on Computer-Based Medical Systems, June 17-19. Finland.

/13/ Park, S. and Kautz, H. (2008) Hierarchical recognition of activities of daily living using multi-scale, multi-perspective vision and RFID. Proceedings of IET 4th International Conference on Intelligent Environments, July 21-22. Seattle, USA.

/14/ Rashidi, P. and Cook, D.J. (2008) Keeping the intelligent environment resident in the loop. Proceedings of 4th International Conference on Intelligent Environments, July 21-22. Seattle, USA.

/15/ Lu, C.-H., and Fu, L.-C. (2009) Robust Location-Aware Activity Recognition Using Wireless Sensor Network in an Attentive Home," IEEE Transactions on Automation Science and Engineering. 6(4): 598-609.

/16/ Youngblood, G.M. and Cook, D.J. (2007) Data Mining for Hierarchical Model Creation. IEEE Transactions on Systems, Man, Cybernetics, Part C (Application and Reviews). 37(4): 561 – 572.

Muhammad Raisul Alam

Institute of Microengineering and Nanoelectronics, Universiti Kebangsaan Malaysia, Bangi, Selangor, Malaysia.

Mamun Bin Ibne Reaz, Mohd. Alauddin Mohd. Ali, Salina Abdul Samad

Department of Electrical, Electronic and Systems Engineering, Universiti Kebangsaan Malaysia, Bangi, Selangor, Malaysia.
Email: {raisul,mamun,mama,salina}@eng.ukm.my

DESIGN AND IMPLEMENTATION OF RAPID CONTROL PROTOTYPING SYSTEM WITH MATLAB/SIMULINK

Nikolaj Semenič[1], Andrej Sarjaš[2], Rajko Svečko[2], Amor Chowdhury[1]

[1]Margento R&D, Maribor, Slovenia
[2]FERI, Maribor, Slovenia

Key words: Rapid control prototyping, Real time workshop, DSP, TMS320F28335, Matlab, Simulink, State space control, inverted pendulum

Abstract: This paper presents the development and implementation of a Rapid Control Prototyping (RCP) System. Key features of RCP are working with simulink block sets, automation of code generation and automatic downloading of executable code to the target DSP. In such manner, control algorithms can be rapidly integrated or adapted in no time. Simulink integrated with DSP TMS320F28335 provides a useful development tool for design verification of control algorithms, suitable for different plants. Through the use of RTW (Real Time Workshop) functionality, different modules on custom made DSP board are developed, which are needed to create an environment that is suitable for processing execution. Software has been developed with the use of Simulink block sets. Some of them have been provided from TIC2000 library. More complex blocks have been developed with the use of S-functions and TLC, target language compiler.

Design and realization of regulation algorithms for stabilization of rotary inverted pendulum are presented.

Načrtovanje in implementacija RCP sistema v okolju Matlab/Simulink

Kjučne besede: RCP, RTW, DSP, TMS320F28335, Matlab, Simulink, Prostor stanj, inverzno nihalo

Izvleček: V delu predstavljamo razvoj in implementacijo sistema, ki omogoča hitro in zanesljivo integracijo in verifikacijo algoritmov vodenja na realnih objektih. Ena izmed bistvenih prednosti takšnega sistema je, da ga zgradimo s pomočjo blokovnih objektov v Simulinku. Ti pa se samodejno prevedejo v ustrezno izvršno datoteko, ki se naloži na DSP. V takšnem smislu sistem omogoča enostavnejšo implementacijo algoritmov in hkrati njihovo lažjo prilagodljivost. Z uporabo Simulinkove knjižnice RTW je moč razviti različne module za podporo različnih funkcionalnosti na digitalnem signalem procesorju. Sistem smo razvili s pomočjo osnovnih blokov, ki jih najdemo v knjižnici TIC2000. Kompleksnejše funkcionalnosti pa smo zagotovili z razvojem lastnih, naprednejših blokov, s pomočjo izgradnje S-funkcij in z ustrezno korekcijo prevajalnika TLC.

Predstavljamo r*azvoj algoritmov vodenja za stabilizacijo rotacijskega inverznega nihala.*

1. Introduction

With the fast development of digital signal processors, they not only became less expensive but also faster and more complex. Tools for planning and development of embeded-systems are developing in a similar fashion as well. Development of embeded systems is such a complex task that it demands from an engineer a precise knowledge of the DSP architecture and the periphery, as well as programing tools for planning of process systems. The knowledge of suitable program languages is necessary as well. In spite of the fact that many manufacturers of developing program equipment invest a lot of energy in the development of efficient compilers, sometimes it is neccessary to use the assambly language to optimize specific processes in DSP.,. Even more with the complex systems, the probability of an error is high, despite the experience and appropriate expertise of the developer. Thus, an industrial manufacturing leans towards a smaller number of errors during the production as well as to decrease the time needed to develop the product and all the related costs. With that intent, the rapid control prototyping (RCP) has started to develop. In that way, various algorithms can be tested in real time on real plants through use of the circuit boards, which have been especially developed for that purpose. That way, there is

no need to develop any hardware parts and it is not necessary for the designer to deal with possible mistakes that would come along. It would be logical that the developer focuses only on the development of algorithms. A way of programing is set in a way of blocks that assemble in complex block models. A way of rapid prototyping is offered through the MathWorks' Matlab or Simulink. With the built in real time workshop (RTW) library or precisely TIC2000, Simulink offers the possibility to develop the embeded block model system along with blocks that are offered by other libraries. Through RTW mechanism Simulink block model is converted to the project in the DSP software developing environment Code Composer Studio (CCS), in a form of files (.c and .h), it generates an executable file (.out) and loads it onto the DSP. TIC2000 library enables the development of the Texas instruments' DSPs from C2000 family. The RTW offers support for custum circuit boards as well.It si also posible to implement circuit board with DSPs which are not found in the library. Although this procedure is a bit more complex.

In previous work, with the use of Simulink, the researchers have been involved with rapid prototyping in the control systems. Some of them have only used the basic blocks, which are found in the TIC2000 library /1-5/. In part /6/,

the development of custom Simulink blocks is discussed with S-functions in the sense of adding the functionality in a form of a C language program . In such form there is not possible to add additional assebly commands or to support additional hardware moduls. Some of them broadened a basic block recruitment with the development of additional, more complex hardware moduls. In this case, a more efficient custom circuit board is used which has been created independently /7,8/.

Development of rapid prototyping sytem using Simulink environment and a custom circuit board based on floating point DSP TMS320F28335 is presented in this work, . To take into account that we have not used any of the expected circuit boards from the TIC2000 library, but developed it independently, it has also been necessary to develop specific blocks that have been more complex than the basic ones. The more complex modules or drivers have been developed through use of S-functions and the TLC (Target Language Compiler). Our rapid prototyping system is more usable since it has, in comparison to the circuit boards from the TIC2000 library, some extended hardware peripherals. The system is tested with the stabilization of the rotary inverted pendulum in which we use different control algorithms that are designed with the help of Matlab functions.

System for rapid prototyping designed with Matlab/Simulink is Presented in the section two. The third section describes, in detail, a circuit board and the modules that are necessary to obtain measured quantities. The fourth section describes the procedures of implementation of simple and more complex blocks. The fifth section offers a detailed description of the controled plant or the rotary inverted pendulum and the measured quantitiy. The base and the working of stabilization system of the rotary inverted pendulum is explained in the sixth section . In the seventh, design of regulators is summarized. The resaults wich proove the success of implementation of the system for rapid prototyping with the Matlab/Simulink are presented at the end.

2. Rapid Control Prototyping with Matlab/Simulink

Simulink, with the RTW tool, and the TIC2000 library, that offers support to all of the DSPs from the C2000 family, with the development software Code Composer Studio, presents a basis of rapid prototyping. Before the Simulink is capable to translate and load the block model onto the DSP through the use of the CCS, it is necessary to take care of the DSP's fundamental settings. That is done through the block F28335 eZdsp from the TIC2000 library. Despite the fact that our circuit board differs from the expected F28335 eZdsp board, that is not an obstacle in assuring the basic functionality of the DSP. This block takes care for an appropriate setting of the memory map and chooses desired functionalities at the DSP pins. In the RTW system, it is also necessary to set a suitable System target file, Make command and a Template makefile. The first one is set in a

relationship to the DSP, however in the case of other two, the default settings are suitable. /9/

Procedure to the executable file is a complex process (Figure 2.1). Models in the Simulink scheme are translated into objects (.rtw). The TLC translates these objectcs into appropriate files (.c and .h) and while at it, adds the system files. It can add custom files as well. Template makefile (.tmf), with the generation of the appropriate Makefile (.mk), links together a file into the executable file (.out) (Figure 2.2). The system of generating a code into the RTW can
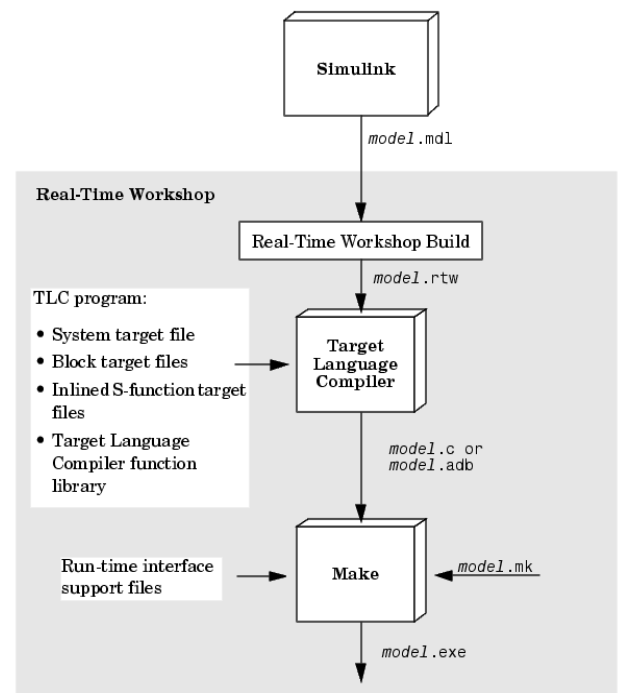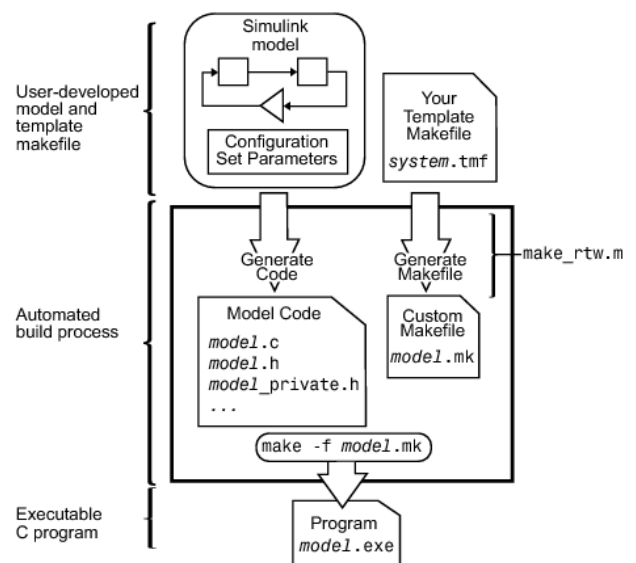

Fig. 2.1: Process of creating a code/9/

Fig. 2.2: Process of creating an exe file /9/

be adapted with the help of the RTW. With an appropriate adaptation of the TLC, inlined S-functions can be created.

Informacije MIDEM 41(2011)2, str. 122-131

N. Semenič, A. Sarjaš, R. Svečko, A. Chowdhury:
Design and Implementation of Rapid Control Prototyping System ...

Through use of TLC and wrapper or inlined S-functions we can add not only the individual functions in the form of C code, but also the adaptations in the assembly language or hardware instructions. /9/ In that way, individual drivers can be implemented to extend the functionality of the circuit board in the Simulink.

3. Hardware architecture and software implementation considerations

Circuit board, based on DSP TMS320F28335, was developed with the purpose to establish the system for verification of the control algorithms used in various control plants (Figure 3.1). Individual modules are enabled and executed on the DSP, which ensure gathering and processing of the measured quantities as well as signals for driving actuators.

DSP belongs among a 32-bit microcontrollers intended for applications in real time. DSP TMS320F28335 has a capacity to operate with the floating point. A good number of functionalities are built-in, which can be used in different applications. /10/
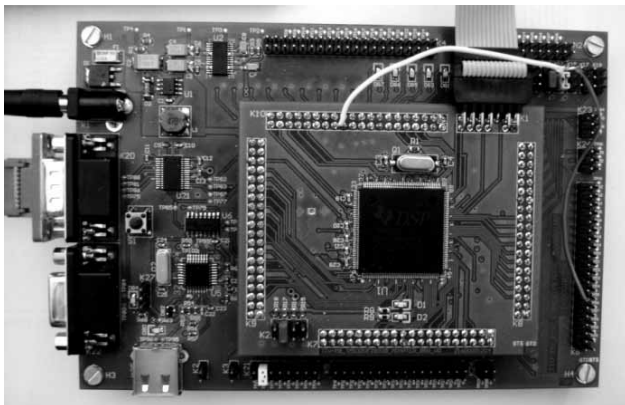

Fig. 3.1: Custom made circuit board

Characteristics of the DSP are:

- Highly efficient 32-bit CPU (IEEE-754 Single-Precision Floating-Point Unit (FPU), 16 x 16 Dual MAC)
- Six channel DMA controller (for ADC, SARAM, …)
- 16-bit or 23-bit external memory interface
- Integrated memory (F28335/F28235: 512KB Flash, 68 KB SARAM, 2 KB OTP ROM)
- Pins from GPIO0 to GPIO63 can be connected to one of the eight external interrapts
- Up to eight PWM outputs
- Three 32-bit CPU Timers
- Serial ports (up to two CAN modules, up to three SCI (UART) modules, up to two McBSP modules (set as SPI), one SPI module, one integrated I2C Bus)
- 12-Bit, 16 channels
- Module for an event count and a modul for encoder support

- Up to 88 multiplex GPIO pins with the input filters

In comparison to the circuit board from the TIC2000 library eZdsp F28335, our circuit board has a number of important advantages:

- On the circuit board, there is a 22-bit four channel external AD converter ADS1213,
- external flash 8Mb, M25PE80,
- external 512 kW RAM ISSI IS61LV51216,
- external EEPROM 128 kb, M95128,
- Converter from RS232 to USB for the communication with the personal computer.

External AD converter enables a higher quality gathering of measurements than the built-in one. Difficulties with lackage of memory are taken over by large external memories such as RAM, Flash and EEPROM. Because of high capacity of memory, the circuit board enables development of very complex systems as well. A similar circuit board is used in the mobile payment system /14/.

With the help of the block from the TIC2000 library and an additional block that extends the basic functionality, a modul for an encoder support was developed on the circuit board. Custom made blockfor the support of the external AD converter was developed independently, with an additional driver and SPI communication-bus.

3.1. Encoder support modul

Encoder support module (eQEP) in the DSP is designed for linear or rotational incremental encoders for measuring position, direction of rotation, and speed. The counter clockwise rotation is defined at the time when QEPA signal outpasses the QEPB signal (Figure 3.2). A frequency of QEPA and QEPB signals alters in relationship to the speed of the motor. That way, the speed is calculated with the QEPA and QEPB event count or by measuring the time between two events.
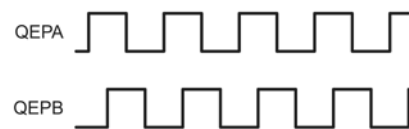
Fig. 3.2: Signals scheme from encoder

The speed can be calculated in two different ways:

$$v(k) \approx \frac{x(k) - x(k-1)}{T} = \frac{\Delta X}{T} \quad /9/ \qquad (3.1)$$

$$v(k) \approx \frac{X}{t(k) - t(k-1)} = \frac{X}{\Delta T} \quad /9/ \qquad (3.2)$$

Equation (3.1) represents a number of pulses that are perceived by the DSP in a defined period of time. DSP can be set in a way that it counts positive and negative fronts of the QEPA and QEPB signals. That way twice the amount of events is obtained in return.

N. Semenič, A. Sarjaš, R. Svečko, A. Chowdhury:
Design and Implementation of Rapid Control Prototyping System ...

Informacije MIDEM 41(2011)2, str. 122-131

A unit period is set to scan time value , in which the DSP counts the events. A unit period is set in the QUPRD registry where the end number, up to which the counter reaches, is written. The amount of one time quantum is inversely proportional with the frequency of the processor core, which is 150 MHz. Upon the expiration of the time period, the register position (QPOSLAT) is copied, with the number of events, which are perceived by the DSP in the period unit. This type of measuring and calculating the speed is suitable for higher speeds, since with the large number of counted events, the counting error is less noticable.

A more suitable way for lower speeds is offered in the equation (3.2). In that case the time between the two events is measured. Performed path between the two events presents an inverse of a maximum number of events in one turn. In that case the error of the time counter is smaller, the longer is the time duration between two events. The timer value, which measures the QCTMR time, is saved into the QCPRD register when the second event occurs.

Encoder support module was executed with the help of block from the TIC2000 library. Direction of rotation and values of registers QPOSLAT and QCPRD were chosen as output values of the module. To that block, one more was added, which was developed independetly with the help of S-function. In that module, both algorithms for speed measuring were executed. Further the system that increases the robustness of measurings was added. An algorithm (3.1) is used to measure higher speeds and an algorithm (3.2) for lower speeds.

A boundary that defines which speed has a lower error is defined with the calculation of relative speed errors. That way, there is a relatively low error in wide range of speed measuring optaned.
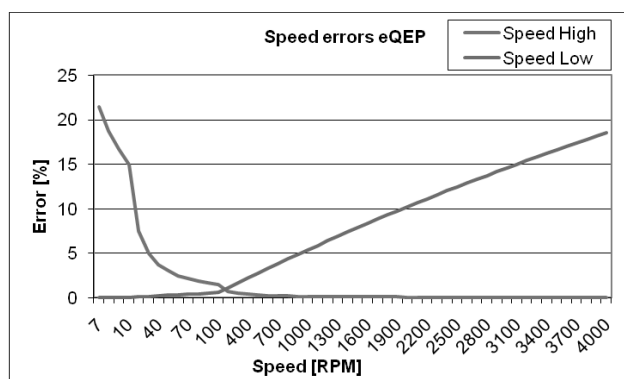

Fig. 3.3: Algorithm errors

As it is seen, (3.2) algorithm has lower error for the speeds up to 240 turns per minute. For higher speeds (3.1) algorithm is more accurate.

3.2. External AD conversion through the SPI bus

Conversion from the notebook or an analog world to a discret or digital world is one of the frequent procedures that are part of the everyday, when it comes to control systems.

External AD converter ADS1213 is located on the circuit board and is a 22-bit delta sigma AD converter with the 20-bit resolution at 10Hz and a 16-bit resolution at sampling rate of 1kHz. It has four chanels at the input which are, via multiplexer, connected onto the diferential input. It also has an integrated amplifier for small signals and it has a support for SPI or I2C communication. It is connected to the DSP through the SPI communication bus and it enables gathering of data with a frequency of up to 6,25 kHz. The chip has integrated special callibration mechanisms that offer a precise set up of the measuring range and of the initial offset. It also has its own built-in micro controller that manages instructional, command and data registers as well as two callibration registers. The way something is written in these registers is through the SPI bus.

One of the main advantages of this converter is the built-in digital filter. Its function is decimation of the current measurements that are offered by the delta sigma modulator. A number of resaults that the filter decimates depends on the decimation ratio that is set in the command registry. Turbo mode influences the frequency of the modulator. This means that those two factors indirectly influence the calculation speed and the delivery of data into the data register. /11/

The speed of output data is determined by the following relation:

$$f_{podatki} = \frac{f_{XIN} \cdot Turbo\ Mode}{128 \cdot (Decimation\ Ratio + 1)} \tag{3.3}$$

Where:

$f_{podatki}$ - frequency of output data

f_{XIN} - frequency of the input oscilator is 2 MHz

Because we want an even more precise measurings, that way we want an even higher decimation ration. That can be reached with the highest setting of the turbo mode.

It is necessary to enter Turbo Mode, Decimation Ration and many other parameters in appropriate addreses in the command registry. The measuring range of the input signl is from -5 to +5 V, with the selection of inside amplification.

The communication between the AD converter and the DSP was realized through the SPI, serial peripheral interface. The type of communication is in a form of master to slave, in which the DSP is the master and the AD converter is a slave. This means that the AD converter only responses to a demand of the DSP. Communication is functions in a way that it is necessary to send the content of the instructional registry to the AD converter first, with which AD receives the name of the appropriate registry and the information if DSP will write out of it or read from it. Since DSP manages the SPI clock, there is a need to detect when the data is ready to be received from the AD converter. AD reports that through an external pin. External pin triggers external interrupt in which DSP processes received information.

The external AD converter is used because of the higher quality of measurements in the system. As we have seen,

it has a built-in digital filter that averages in our case 2499 measurements. One more advantage is that the AD converter is completelly autonomous and works independently from the DSP. Therefore a good amount of processing time is saved for the DSP.

Modul that enables gathering of measurements from the external AD converter was developed in Simulink, independently, in a form of a block. Due to the complexity, the communication system was not able to be built with the basic blocks from the TIC2000 library.

3.3. Connection to the computer

Serial Communication Interface (SCI), also known as UART, is a two-wire asynchronous bus that is used for communication with other DSPs or devices. It is made out of seperate units for sending and receiving which enables half-duplex or full-duplex transfer of data.

UART is used for the communication with personal computers. In such way the measurements are received from the DSP. The reverse communication, from personal computer to the DSP, was also realized.

Communication of data was realized according to the idle-line,, because there are not more than two participants in the communication. Measuring resaults are sent in the core of the main programe without disturbing time-deterministic programe interrupts.

That model was also developed on our part. In such way it was simpler to realize the measuring of time necessary to send the data to the personal computer. The time duration of programe routines were measured with CPU-timer by its activation at the beginning of selected programe routine and its determination at the end of programe routine.

3.4. Pulse width modulation

The DSP supports six PWM modules that enable, on each of the external pins, two different pulse width modulated signals. Every modul enables an optional selection of the most different properties at the exit of the generated signal. PWM signals have a wide use in the telecommunication, to manage different elektromechanical sections, as well as to supply systems in the alternative circuit.

The necessary moduls have been enabled with the help of blocks from the Simulink library.

4. Implementation of program units into the Matlab/Simulink

Individual programe units on the circuit board were developed with the Simulink programe, real time workshop (RTW) tool. Matlab 7.4, respectively, the Simulnk TIC2000 library with the DSP support TMS320F28335 was used for the implementation of modules. The library supports all basic models that are provided by the DSP. In com-

parison with the previous versions of Matlab, this library is wealthier. Modules are more comprehensive and enable more precise registery settings. For example, a comparison between an encoder modul for TMS320F2812 and TMS320F28335 is noticable. (Figure 4.1 and Figure 4.2). As it can be seen, the difference is considerable. We are very limited with the older version. In the mean time, with the newer version, we can reach for more demanding settings of the DSP hardware modul, which enables a more demanding and more universal use of the modules. Matlab 7.4, in comparison to its previous versions is reacher for newer platforms. A functionality to control interrupt routines in a form of Hardware interrupt and Software interrupt blocks was added.
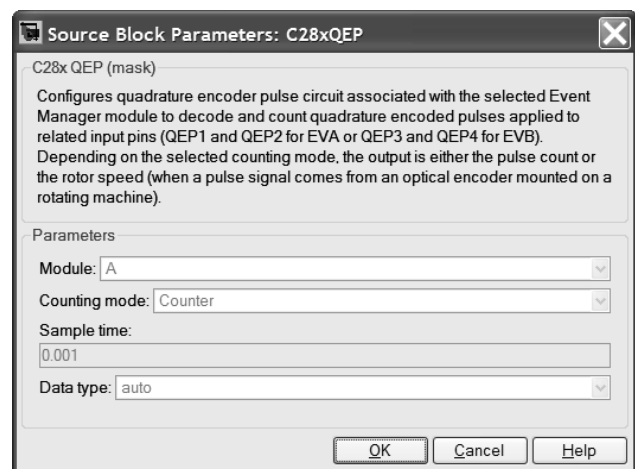
Fig. 4.1: Block for encoder support in Matlab 7.1
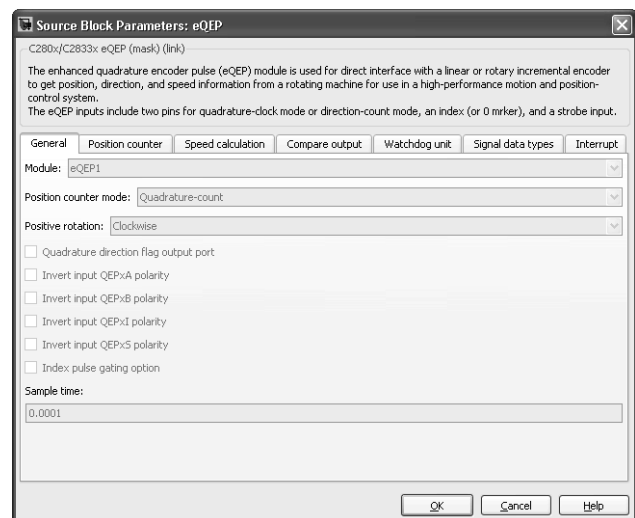
Fig. 4.2: Block for encoder support in Matlab 7.4

4.1. Set of Moduls in TIC2000

In the TIC2000 library, which is designed for hardware support of the texas' DSPs, the following blocks can be found; block for AD converter support, digital inputs and outputs, PWM block, encoder block, block for an event count, Watchdog, support for SCI, SPI, CAN, I2C communication, idle task block as well as a support block for

hardware interrupts and software interrupts. In the library, next to those, are also blocks To RTDX and From RTDX. Those blocks are used to reestablish the connection between CCS and Matlab programe, which enables transfer of data in real time.

Out of those blocks, folowing blocks were used; for the actuator PWM block drive, encoder support block, block for hardware interrupt as well as the idle task block. The hardware interrupt block enables control over triggering hardware interrupt service routines for external AD converter and encoder. The idle task block was used for independent functioning of communication system with the personal computer in a way that it does not distrub carrying out of time deterministic interrupt routines (Figure 5.1). Blocks To and From RTDX were used to reestablish the connection between CCS and Matlab software. That way, the executable file can be downloaded and run onto the DSP out of Matlab's workspace. This tool is also suitable for exchange of optional variables between the DSP and Matlab's workspace. In spite of the fact that we were able to establish a connection through a single channel and to qualify the transfer of one variable, we noticed large irregularities by the transfer of more variables through more channels. That kind of working could be expected due to a poor J-Tag equipment. By the work J-Tag XDS510 was used. Better J-Tags (XDS560) promise more robust transfer of data and higher data rates (up to 2 MB/s) through the use of the Hi Speed RTDX functionality. Because of unespacted functioning of RTDX, the transfer of data was conducted via serial bus SCI, respectively UART.

The basic framework programe, built by the Simulink in the CCS tool programe, is built in the form of a CpuTimer0 timer interrupt routine in a way that the blocks in the basic Simulink scheme are carried out with a specified sampling time. Therefore we have to be careful by choosing the sampling time. In order to assure a time deterministic system, the sampling time has to be longer than the carrying out of a system in the preemption. In case we want a certain part of the system to be carried out in the background, so it does not disturb high priority interrupts, an idle task has to be used. In idle task block can be specified whether the preemption is preemptible or non-preemptible.

4.2. Development of additional blocks with S-function

S-function is a tool that enables integration of custom functionality in the form of a program language C or Matlab's script language. That way a custom block, with a specific functionality, can be created. There are three different ways to integrate program codes in Simulink, Noninlined S-functions, Wrapper S-functions and Fully Inlined S-functions. Noninlined S-function does not require any of the additional tasks such as code adaptation in TLC. They can be created with tools that enable an automatic creation of S-functions or they can be written individually. In the last case, we have to be deeply engaged in the building of a function as well as

to master the syntax. Taking into an account that the syntax of S-functions is unique, this work, specialy with complex functions, may take a good amount of our valuable time. That type of building of S-functions does not prove to be the best in the case when we want to integrate a code into Simulink. For example, in the program language C, which is a widespread way of programming especially among embeded systems programers. The integration of the code can be done with the Wrapper S-function. In that case it is not necessary to integrate an entire code manually in the S-function, but only a call to the assigned routine can be added. Ony the basic model of S-function can be used, therefore we do not have to occupy ourselves with the in-depth knowledge of S-functions. The above mentioned procedures are only suitable for the integration of a C programe language and that way they are not suitable for the development of drives, that require hardware instructions syntax for access to registers and the assignment of their evaluations. Fully Inlined S-function means that the algorithm is integrated with the TLC functionality. In that case, a more precise knowledge of TLC syntax is necessary. This case of S-function is suitable for development of drivers, since an optional code, or hardware instructions, can be added into the TLC file. Or appropriate instructions can be added to the TLC, which can add suitable hardware instruction files (.c or .h) to the CCS project.

Matlab 7.4 version is reacher for quite appliable tool, Code Legacy Tool /9/, which provides automated creation of Wrapper or Fully Inlined S-functions. Matlab 7.1 does not support that tool. That way, an integration of the programe code written in the C language is now faster and a lot simpler. A code that we want to implement in the form of S-function has to be written in the form of a function based on C language. It is needed to remodel input and output function variables. With mentioned tool, we were able to develop custom blocks in the C language. Also, through this procedure an outline for development of drives was also developed.

4.3. Increase of encoder robustness

A block for encoder support, from the TIC2000 library is used to gather position and rotation speed measurements. The block is adjusted to the appropriate settings. On the output of the block, an information on the rotation direction and the value on the event count in sampling time and the number of time quantums between two events can be obtained. With this information, the position and the rotation speed in every sampling time can be determined. During testing of functionality of the modul, was found that in specific situations it came to an irregular calculation of values. A block or S-function, which eliminates the occured difficulties, was added to increase the robustness of operating of the modul.

When the encoder modul counts a full event, it means that the encoder modul measured the change of the position exactly for one turn. The encoder modul is designed in a

Informacije MIDEM 41(2011)2, str. 122-131

N. Semenič, A. Sarjaš, R. Svečko, A. Chowdhury:
Design and Implementation of Rapid Control Prototyping System ...

way that when it counts a full event, the encoder counter is set to 0. In case of the opposite rotation, when it counts to 0-th events, the values are set to the maximum number of events in one turn. Most of the time, the difficulties with the measuring had occured exactly at the turn of 0., the maximum number of events and when the rotation direction suddenly had changed. Difficulties had appeared when the position had to be determined and with the calculation of speed through an algorithm for higher speeds (Equation 3.1). From an equation 3.1, it follows that the position and the rotation speed are usually measured with the difference between the current number of events and the number of previous events. Scheme on how the position and speed are determined is presented in Figure 4.3. The beginning of the arrow represents the number of previous events, the end of the arrow the number of current events. Arrows are designed to schematically illustrate posible occasions of two successive events and they do not proportionaly represent events of real values. In a real example, the proportions among values of previous and current events are diminishing, they depend on the rotation speed.

In example A, the difference between the number of current and previous number of events is higher than the half of the maximum number of events (Half-event). A difference upon which the new position and speed can be calculated is defined with:

difference = -(*full-event* - (current_eve -previous_eve)); abs_position += difference; where the position is reduced with an actual difference, which is negative

In the example B, difference is defined with:

difference = current_eve - previous_eve;

abs _position += difference; where the position is increased for an actual difference.

In the example C, difference is defined with:

difference = (*full-event* + current_eve - previous_eve); abs _position += difference; where the position is increased for an actual difference

In the example D, difference is defined with:

difference= current_eve - previous_eve;

abs _position += difference; where the position is decreased for an actual difference
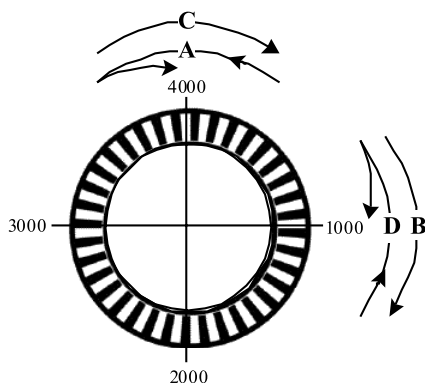

Fig. 4.3: Scheme of the encoder events and the principle calculation of speed and position

A suggested algorithm is suitable for both directions of rotation, since it considers actual shifts, regardless of direction of rotation. It also fixes incorrect calculations that occur around 0-th or full event. Operating of the module improves and the measurements robustness increases.

4.4. Realization of drivers in the Simulink

As it has been already mentioned, the Code Legacy Tool enables an automated procedure of code integration written in C. In this way, an outline of more complex blocks were created, which also include manipulations with registers and hardware instructions. A custom block was developed to receive values from the external AD converter through the SPI communication bus and a block for communication with the personal computer. For the development of complex blocks, that also contain drivers, we used the following algorithms:

- A compiler with the command mex(„-setup') is set in Matlab

- In the custom C function, input and output values are appropriately adapted just like Code Legacy Tool requires. Input and output function values represent inputs and outputs of the block. The function can also contain instructions. It can also contain calls of other functions from other files as well as macroes or lists.

- In the custom C function it is necessary to coment all calls to other functions, macroes, hardware instructions, registry manipulations. The purpose of the Code Legacy Tool is only the development of C-MEX S-function, which can be integrated as Simulink's S-function block.

- C-MEX S-function and the TLC file is created with the use of Code Legacy Tool.

- To the TLC file, required source or header files (.c or .h) containing hardware instructions are added. Source files (.c) can be added with the instruction %<LibAddToModelSources(„SPI")>, header files (.h) can be added with the instruction %<LibAddToCommonIncludes(„Device.h")>. Instructions have to be added in the core of BlockTypeSetup function in TLC file. Calls to initialization routines of hardware moduls can be added to the function start. In the function outputs, function call to the custom C function can be noticed, which is a result of previous C-MEX S-function generation.

- The model is loaded in Simulink. A project with source and header files in CCS is generated. We look for a custom C function file in the project and uncomment the commented parts of code.

- Added part of the code can be debuged as well and in that way the success of operation of the added module can be prooved in the CCS

After the mentioned algorithm, a modul that receives values from an external AD converter and a modul for communication with a personal computer were added. Modul for AD conversion was developed, since that kind of system was

N. Semenič, A. Sarjaš, R. Svečko, A. Chowdhury:
Design and Implementation of Rapid Control Prototyping System ...

Informacije MIDEM 41(2011)2, str. 122-131

not possible to realize with basic blocks, mainly because of the complexity of communication through the SPI bus. Modul for communication with a personal computer enables an easier supervision over the sent and received data, since a duration time needed for the execution of the specific part of code can be exactly measured with the CPU timer in the DSP.

5. Example of test plant control

A test plant consists of a mechanical framework, pendulum, electrical motor, feeder and a processor with the adapted electrical circuit.

The concept of stabilization of an invert pendulum presents a mounted arm on an electrical motor, where at the end, on the bearings, a pendulum is mounted. With a suitable control of the electrical motor, we can affect the position of the arm and indirectly so, the position of the pendulum.

State space controller have been designed to achieve stabilization. That way we need the information on all of the internal states od the system. These are the speed and angle of the pendulum and the speed and position of the arm. The speed of pendulum is calculated on the basis of pendulum angle change. Position and speed of the arm is measured with the encoder.

Potentiometer is set behind the bearing of the pendulum and it is supplied by voltage of 5 V. The signal in the frame of 0-5 V presents the position of the pendulum 0-360 °. Due to the nonlinearity of the potentiometer, it is possible to measure in a range of 0-340 ° with ± 3 ° of tolerance.

Encoder modul enables measuring of the position and the speed of the arm with event signals received from encoder. Event represents every positive or negative front of the encoder output QEPA or QEPB signals, that are dislocated

among each other by 90 ° (Figure 3.1). Encoder has 1000 lines. Taking that in consideration, due the possibility to register positive and negative fronts, it can be registered 4000 events in one turn.

An electrical circuit is located on the external circuit board, which adapts levels of voltage supply between the processor and the motor as well as between the processor and the sensores.

On the ecternal circuit board, there is a H-bridge that provides up to 6 A of current for the motor. H-bridge is controled by the processor by the principle of pulse width modulation (PWM).

6. Design of the core program for stabilization of the inverted pendulum

A row of hardware interrupts were realized in the DSP. Every interrupt has its own specific time deterministic task. In the center portion of the program core, which is presented by an infinite while loop, functions are carried out that take care of sending the measuring resaults to the personal computer.

Synchronization of the external AD converter with the DSP, is carried out through an external interrupt. When AD has the current measured data available in the memory data registry, the external pin DRDY falls to 0. This happens exactly evey 0,01 s, which is the sampling time. This event triggers the hardware interrupt in which, through the SPI bus, value of the data register of AD converter is obtained. In that interrupt, the value of the register QUTMR of encoder module is adapted as well. That is the encoder modul timer which is responsible for triggering of the encoder interrupt,. that is also triggered every 0,01 s, respectively the sampling time. With the adaptation of the encoder timer, the synchronization of the encoder interrupt routine with the interrupt of the AD converter is reached. In the interrupt of the AD converter, with the appropriate setting of CpuTimer0 value, the synchronization with the system interrupt is also performed. Through the proper synchronization encoder interrupt occures just before the interrupt of AD converter. System interrupt of Simulink follows both interrupts. The position and the speed of the arm is obtained during the interrupt of the encoder. In the interrupt of the AD converter, the information on the position of a pendulum is obtained, the speed of the pendulum is calculated on the basis of the change of the pendulum position. In the system interrupt, the chosen regulator is calculated and an adequate PWM exit is set (Figure 5.1)

The system is designed so that the interrupt of AD converter has a priority over the encoder interrupt.
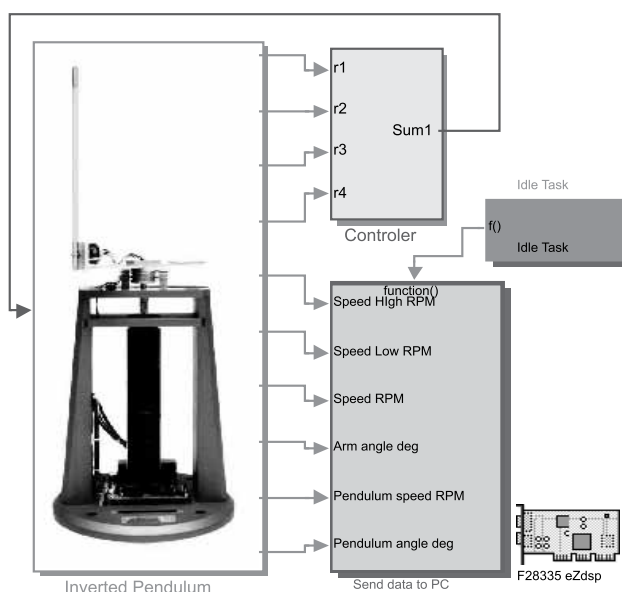

Fig. 5.1: RCP for inverse rotation pendulum

Informacije MIDEM 41(2011)2, str. 122-131

N. Semenič, A. Sarjaš, R. Svečko, A. Chowdhury:
Design and Implementation of Rapid Control Prototyping System ...

7. Designing the state space controllers

For the control system, inverted pendulum two type of state space controllers were designed. The first type of state space controller was designed through pole placement technique (PPT) and the second type with optimization of the quadratic continuous-time cost functional (LQR). A mathematical model of third and fourth order was used for design of controllers. Model was adapted from work /12/. Pole placement controller was designed with the closed-loop poles assignment and Matlab command »acker«. LQR controller was designed with the expression »lqr« and the appropriate weightening (Q and R) matrices.

Taking into consideration that the controllers were designed for a linear system and tested on a nonlinear model in Simulink, where was checked whether the solutions suit the stability criteria. With the simulations, we could also test until which point the system was stable, if pendulum had deviated.

8. Resaults

During the design of PPT controllers, a third order model was used, since the control upon the position of the arm is not significant for the stabilization of the pendulum. During the realization of the controller with the setpoint, a fourth order model and the position of the arm was used as a reference signal. LQR controller was designed with the systems of third and fourth order.

As results show, the best designed controllers are those, which are designed with the third order system. That is to say, the controllers do not demand the stabilization of pendulum in exact defined point of the position of the arm. If we compare these two controllers to the controller with the setpoint, it is established that in the maximal deviation of angle of the pendulm, it swings almost twice the amount. It is comprehensive that by the setpoint controller considerations not only about the angle of the pendulum but also the position of the arm like setpoint is taken into account.
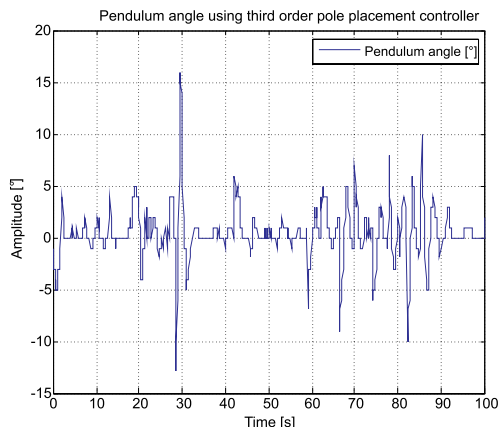

Fig. 8.1: Pole placement controller
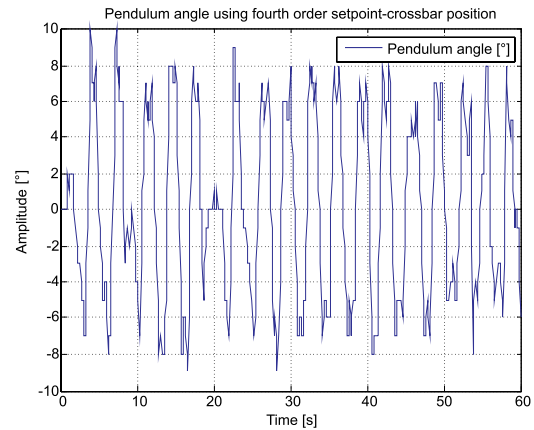
Fig. 8.2: Controller with the setpoint-crossbar position
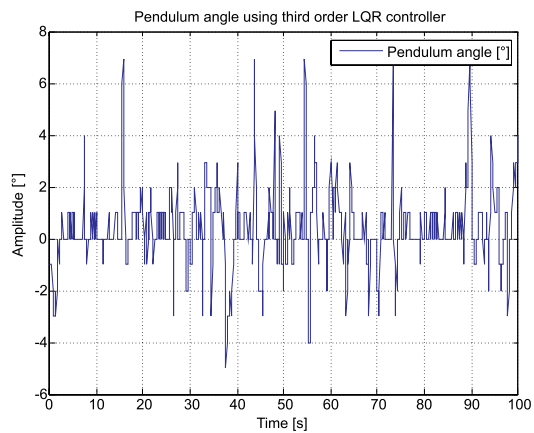
Fig. 8.3: Third order LQR controller
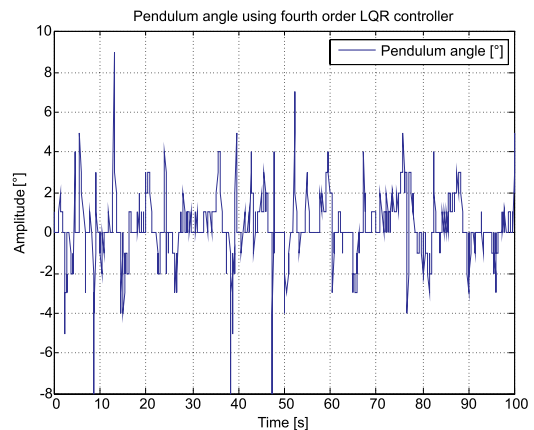
Fig. 8.4: Fourth order LQR controller

Two linear quadratic controllers were calculated. A third order system was used to design the first one. With the second one, a fourth order system and the position of the arm as a reference position were used. If we compare the measurements with previously mentioned controllers, it is visible at first sight that both positions of the pendulum were steadier. If we compare the strenghtening of both regulators with the ones before, it is stated that they are much more sensitive to the position of the pendulum.

9. Conclusion

The goal of our work was to carry out the system for rapid prototyping in the Matlab/Simulink environment. It is confirmed that the newer version of Matlab has numerous advantages with the development of Code Legacy Tool modules and the expanded set of TIC2000 library. Individual basic moduls in the library are more complex and enable more precise hardware settings, that are very welcomed since they enable improved functionality. With that, an in-depth knowledge of hardware DSP moduls is neccessary. The system of rapid prototyping, with rich library collection in Simulink, presents a simpler and faster way of adaptation of algorithms that are in the form of block models and a simplified algorithm testing on real plants. The system of rapid prototyping was successfully tested with the stabilization of the rotary inverted pendulum.

10. Acknowledgment

References

/1/ L. Baotai, Z. Rongxiang, Rapid Control Prototype Design of the DC/DC Converter for Fuel Cell Electric Vehicles, Power and Energy Engineering Conference, 2009. APPEEC 2009. Asia-Pacific.

/2/ R. Duma, P. Dobra, M. Abrudean, M.Dobra, Rapid Prototyping of Control Systems using Embedded Target for TI C2000 DSP, Mediterranean Conference on Control and Automation, July 27-29, 2007, Athens.

/3/ W.S. Gan, Y.K. Chong, W. Gong, W.T. Tan, Rapid Prototyping System for Teaching Real-Time Digital Signal Processing, IEEE transactions on education, vol. 43, no. 1, february 2000.

/4/ A. Rubaai, M.J. Castro-Sitiriche, A.R. Ofoli, Design and Implementation of Parallel Fuzzy PID Controller for High-Performance Brushless Motor Drives: An Integrated Environment for Rapid Control Prototyping, IEEE transactions on industry applications, vol.44, no.4, July/August, 2008.

/5/ S.H. Seo, S.W. Lee, S.H. Hwang, J.W. Jeon, Development of Platform for Rapid Control Prototyping Technique, SICE-ICASE International Joint Conference, October 18-21, Busan, 2006.

/6/ K.H. Hong, W.S. Gan, Y.K. Chong, K.K. Chew, C.M. Lee, T.Y. Koh, An Integrated environment for rapid prototyping of DSP Algorithms using MATLAB and Texas instruments' TMS320C30, Microprocessors and Microsystems 24, 349-363, 2000.

/7/ Z. Fang, Y. Qi, Q. Zhang, T. Chai, Design and Implementation of a Low Cost DSP Based Rapid Control Prototyping System, Industrial Electronics and Applications, ICIEA 2009.

/8/ Z. Fang, N. Song, L. Wang, Design and Implementation of a Novel Fuzzy Controller with DSP for Rotary Inverted Pendulum, Control and Decision Conference, 2009.

/9/ Real-Time Workshop, User's Guide Version 7.4, 2009.

/10/ Texas Instruments, Incorporated, *Reference Guide, TMS320x2833x, 2823x Enhanced Quadrature Encoder Pusle (eQEP) Module*, SPRUG05A, avgust 2008.

/11/ Texas Instrumets, Incorporated, *Data Manual*, *TMS320F28335, TMS320F28334, TMS320F28332, TMS320F28235, TMS320F28234, TMS320F28232, Digital Signal Controllers (DSCs)*, SPRS439F, junij 2007.

/12/ Burr Brown Corporation, *ADS1212*, *ADS1213, 22Bit analog to digital converter,* USA, april 1998.

/13/ Tan Kok Chye, Teo Chun Sang, *Rotary inverted pendulum*, Scool of electrical and electronic engineering, 1999.

/14/ Zdenko Mezgec, Andrej Medved, Amor Chowdhury, Rajko Svečko,. Mobile payments - design of new terminal = Mobilno plačevanje - razvoj sodobnega terminala. Inf. MIDEM, mar. 2008, letn. 38, št. 1(125), str. 53-60.

Nikolaj Semenič[1], Andrej Sarjaš[2], Rajko Svečko[2], Amor Chowdhury[1]

[1]Margento R&D, Gosposvetska c. 84, 2000 Maribor
[2]FERI, Smetanova ul. 17, 2000 Maribor
E-pošta: nikolaj.semenic@margento.com

AEWSN: ACADEMIC EDUCATIONAL WIRELESS SENSOR NETWORK

Karl Benkič, Marko Malajner, Žarko Čučej

Fakulteta za elektrotehniko, računalništvo in informatiko Maribor, Maribor, Slovenia

Key words: Wireless sensor networks, AeWSN, modeling, simulating, evaluating

Abstract: Wireless sensor network (WSN) is a collection of wireless sensor nodes with wireless communication capability which is often used for military application, real-time surveillance, and similar time-critical applications. This article offers an overview of a wireless sensor network system called AeWSN. AeWSN is a custom designed WSN with software and hardware support. The proposed system was developed as a byproduct of PhD studies and is intended for use as an academic wireless sensor research platform, offering some sort of a framework for higher (level 3 or higher) ISO/OSI layer development in WSN. It offers network and protocol modeling, developing, simulating and experimental testing as well as evaluating it. Finally we demonstrate AeWSN on a simple application.

AeWSN: akademsko izobraževalno brezžično senzorsko omrežje

Kjučne besede: Brezžična senzorska omrežja, AeWSN, modeliranje, simuliranje, ocenjevanje

Izvleček: Brezžična senzorska omrežja (BSO) so postala zanimivo raziskovalno področje v preteklih nekaj letih. Zaradi določenih razlik s podobnimi tipi omrežij (Ad-hoc, MANET) raziskave potekajo dejansko na vseh plasteh referenčnega ISO/OSI modela.

Za testiranje ali razvoj novih algoritmov za uporabo v brezžičnih senzorskih omrežjih je ključnega pomena, da le te najprej simuliramo v simulacijskem okolju, kasneje pa še ovrednotimo in testiramo na realnem brezžičnem senzorskem omrežju. V ta namen je potrebno najprej izbrati dobro simulacijsko okolje in znotraj le tega razviti ustrezen model brezžičnega vozlišča. Obstaja več simulacijskih orodij za simuliranje brezžičnih senzorskih omrežij (OMNET++, OPNET, GloMoSim,…), vsako od njih pa ponuja določene pozitivne in negativne lastnosti. Kljub razširjenosti simulacijskih orodij v bistvu ne obstaja nobena širša študija, ki bi opredelila uporabnost ali prevlado enega od teh. Med izbiro simulatorja za BSO smo najprej izbrali dva potencialno nam najbolj priročna orodja: OPNET in OMNET++. Izbiri OPNET-a je so botrovale izkušnje, ki jih z orodjem imamo in dejstvo, da OPNET ponuja (sicer zaprti) model senzorskega vozlišča ZigBee tehnologije. Za razvoj svoje lastne platforme smo se odločili predvsem zaradi preprostega spreminjanja strojne opreme po potrebi in zaradi pridobivanja znanja in izkušenj, ki ga to delo prinaša. Razvito senzorsko vozlišče SPaRCMosquito med drugim omogoča tudi zamenjavo strojne programske opreme na daljavo, kar velja za eno najbolj priročnih lastnosti vozlišča. Kljub veliki ponudbi programske opreme pa smo zasledili pomanjkanje take, ki omogoča modeliranje BSO in povezovanje sistemov v celoto. Tako je nastala AeWSN (Academic education wireless sensor network) platforma, ki združuje programsko in strojno opremo ter model simulatorja.

AeWSN je sestavljen iz treh glavnih sklopov: Strojne opreme (SPaRCMosquito), programske opreme (SPaRCSoft) in simulacijskega modela (SPaRCSimMod).

SPaRCMosquito senzorski modul temelji na Cortex 1768 mikroprocesorju in MRF24J40 radijski enoti. Senzorski modul omogoča zamenjavo strojne programske opreme na daljavo ter uporabo različnih senzorjev združljivih z AD, SPI, CAN in I²C vodilom.

SPaRCSoft je skupek programske opreme: strojne programske opreme, ki teče na SPaRCMosquito modulih in SPaRCSoft programa (Fig. 4), na katerem je programska oprema, ki kontrolira SPaRCMosquito bazno postajo (BS). SPaRCSoft omogoča, da se SPaRCMosquito obnaša kot bazna postaja, navadna senzorska enota ali vohljač. SPaRCSoft omogoča modeliranje in realno časovni prikaz stanja omrežja (Fig. 5 in Fig. 6), kjer s pomočjo lokalizacije izrisujemo senzorska vozlišča in v določenem razmerju glede na realno omrežje. Delovanje AeWSN sistema smo preizkusili v par različnih aplikacijah, med drugim tudi na problemu določanja lokacije posameznih senzorskih vozlišč. .

1. Introduction

Wireless sensor networks has become intensive research field recent years. Due to their difference from conventional Ad-Hoc wireless networks, researches have covered all the layers of an ISO/OSI model. Originally, IEEE as the Working Group for Wireless Personal Area Networks (WPANs) defined the 802.15 standard, and soon the 802.15.4 standard known as low-rate wireless personal area networks was defined. ZigBee alliance /1/ built their wireless sensor network solution called ZigBee on top of the 802.15.4. standard, as used for physical and medium access layer.

Primarily the need for wireless sensor networks arose in army applications. Remote battlefield and Base-Camp surveillance became simpler and possible using wireless technology. In the future, military applications and decisions

will be based more and more on data gathering, including data from the battlefields. WSN is one of the most promising intelligence data gathering systems /2/.

A typical WSN consists of a large number, even a few thousand, nodes equipped with different types of sensors, microprocessors, radio transceivers, and usually an autonomous power supply, deployed randomly within the area of interest with the goal of collecting sensors measured data and transferring it through one or more data sinks called User Access Point (UAP) or a Base Station (BS) to the end users of WSN services. The random deployment of sensors, for example in battlefields or in plantations, usually means that the positions of the nodes are neither known exactly nor accessible for maintenance and local administration. Consequently, they should have the capabilities for self-organization, within an ad-hoc multihop

network fashion. Under normal working circumstances the majority of traffic flows towards BS /3/, since the BS is a data collector.

1.1. Problem formulation

When developing new algorithms, it is crucial to test and evaluate them. Testing and evaluating is possible through two phases: simulating and evaluating the algorithms in the simulators and then testing, and evaluating algorithms on a real WSN. When simulating the WSN, it is crucial to have a good wireless sensor network and node model and, of course a suitable simulation tool.

There are several network simulators (NS2, OMNET++, OPNET) to choose from but mainly none of them supports WSN natively. OPNET /4/ supports practically all physical radios with many types of modulations and, therefore, it is quite easy to implement a custom PHY layer for wireless communications. Among other models OPNET supports ZigBee and all three types of devices (RFD, FFD and Co-ordinator). For PHY and MAC layers there is source code available, but for the network and application layers there is only an object code. OMNET++ on the other hand, offers a good discrete simulator and 3 party models for the WSN simulations /5/ with or without the limited support, what is expected, because the majority of simulation models are open source projects, done by non-profit organizations (faculties) or individuals. The authors in /6/ offered answers which simulator is more appropriate for certain types of simulation (for example: they recommend the NS-2 simulator for high-precision PHY layers simulation) and how a simulator differs in the same setup and scenarios. The same comparison was done in /7/ where the authors found great differences in MANET simulations executed in the OPNET Modeler /4/, NS-2 and GloMoSim. For example: OPNET simulates a very high time delay in MANET compared to NS-2 and GloMoSim /7/. After evaluation the OPNET simulation tool was selected for simulating WSN.

When selecting the hardware evaluation platform a decision had to be faced: to use one of the existing platforms for wireless sensor networks or develop a new one, despite a few solutions available on the market. AeWSN is developed for education and research work, which at some point include working with images, so the WSN node should use a CPU which is powerful enough. We didn't want to depend on

only one CPU, sensor(s) and radio modules; so, the node has to have modular design. Different setup properties and experiments led us to believe that custom hardware would be the smart choice for us. Hardware choice was based on our previous knowledge, and support from different vendors and companies.

The third part of the problem was the appropriate support software selection. Because there is practically no similar software for developing protocols and evaluating WSN parameters it was decided to create one.

1.2. Related work

There are a lot of manufactures who provide the market with solutions for wireless sensor networks. Some manufactures created a consortium called ZigBee Alliance /1/. Zigbee alliance proposed high layer communication protocol based on IEEE 802.15.4 standard for wireless personal networks (WPAN). The main advantage of a ZigBee is its simpler and cheaper protocol in comparison with Bluetooth, which makes ZigBee very appropriate for wireless sensor networks. Two alliance members, Microchip and Texas Instruments are the world's best-known providers for Zig-Bee protocols and equipment. As a member of the ZigBee Alliance, Microchip offers its customers a certified ZigBee Compliant Platform (ZCP) for the ZigBee® PRO, ZigBee RF4CE, and ZigBee 2006 protocol stacks. The ZCPs ensure interoperability with the ZigBee industry standard. Microchip's ZigBee Compliant Platforms consist of the 2.4 GHz IEEE 802.15.4 compliant MRF24J40 transceiver products, the PIC18, PIC24, dsPIC, and PIC32 families of microcontrollers, and the certified firmware protocol stacks. TI offers cost effective low power RF solutions for the ISM band, ZigBee hardware and software solutions. TI's product offers include RF transceivers, RF transmitters, RF receivers, System-on-Chips, Front Ends and ZigBee Processors.

Some universities and companies use basic hardware to produce their own wireless sensor nodes but, in general, almost all of them use IEEE 802.15.4 compliant hardware.

Table 1. shows the that market offers WSN nodes ranging from simple low power CPUs to high performance ARM processors (PXA271). A conclusion can be made that the selection of a WSN node is typically depended on application.

Table 1: The comparison of some WSN nodes available on the market.

	WeC Mote	Mica2 Mote	MiCAz	Medusa MK2	µAMPS	Imote2.NET
Radio	TR1000	CC1000	CC2420	TR1000	LXM3162	CC2420
MCU	AT90LS8535	ATMEGA128L	ATMEGA128L	ATMEGA 128L AT91FR4081 ARM	StrongARM SA-1100	Marvell PXA271
Operating system		Tiny OS	TinyOS	uCos-II	eCos	Win CE, .NET micro framework
Memory	23KB EEPROM	128 + 512K FLASH	128 + 512K FLASH	1MB FLASH		32MB FLASH 32MB SDRAM

2. AeWSN.NET system

2.1. Hardware – SPaRCMosquito

The Laboratory for Signal Processing and Remote Control (SPaRC) has developed its own wireless sensor node platform called SPaRCMosquito. One of the reasons for developing its own platform was the absence of an ARM microcontroller based sensor node platform on the market. Microcontrollers based on ARM architecture are very popular these days for mobile devices due to their small power consumption, efficiency, reasonable prices, etc. Two sensor node platforms have been developed. One for connecting to a PC, used for data gathering (base station), which is named the SPaRCMosquito Base Station. The independent sensor node, deployed for the field (sensor node), is called SPaRCMosquito. Microchip's MRF24J40 radio module /8/ based on 802.15.4 standard and TI's CC2500 radio module /9/ were chosen for the wireless part.

2.1.1. SPaRCMosquito Base Station

The task of a base station is the gathering of data from an entire wireless sensor network, so, the connection to the higher entity is needed. The SPaRCMosquito Base Station can communicate with a PC, laptop, etc. via USB link. The hearth of base station is a low power LPC 1768 Cortex, 32-bit microcontroller. In addition to the microcontroller, the platform consist of USB and LED drivers, JTAG connector, general-purpose connector (includes I2C, SPI, ADC and GPIO) and other. The power supply is assured over the USB connection. Fig. 1 presents the SPaRCMosquito Base Station.
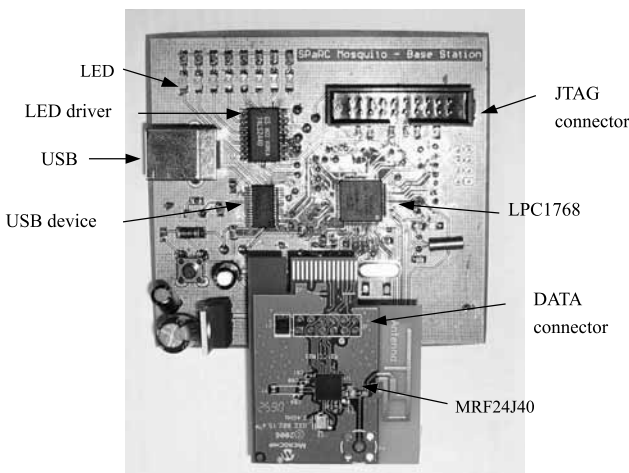

Fig. 1: SPaRCMosquito base station

2.1.2. SPaRCMosquito Sensor Node

The SPaRCMosquito Sensor Node is based on the same platform as the base station with some modifications. There is no longer USB driver and some LED indicators. Instead a connector for the sensor (for measuring physical phenomena), a DC/DC converter and flash memory have been added (Fig. 2).

MRF24J40 Daughter board

The MRF24J40 Daughter board from Microchip is a wireless radio originally designed for the PICDEM Z evaluation platform. This module was used for the SPaRCMosquito platforms. MRF24J40 is fully compatible with IEEE802.15.4 (ZigBee and MiWi). Communication between radio module and microcontroller is established over a 4-wire SPI protocol. CSMA-CA, automatic acknowledge and retransmit are implemented physically on a chip. The data rate is up to 250 kb/s with QPSK modulation and center frequency 2,4 GHz.

CC2500 Radio Module

The CC2500 is a low-power, low cost radio transmitter from Texas Instruments. CC2500 is very appropriate for wireless device like PC mouse, etc. Its embedded modem is designed for a few different modulations: MSK, 2-FSK, GFSK, OOK) and programmable data rates up to 500 kb/s. Power consumption in the receiving mode is 13,3 mA. The surrounding temperature can be measured using a build-in analog temperature sensor. In order to implement the CC2500 radio module only a chip was purchased, because only a chip, few extern passive elements and folded cupper dipole antenna on substrate is needed for the assembly /10/.
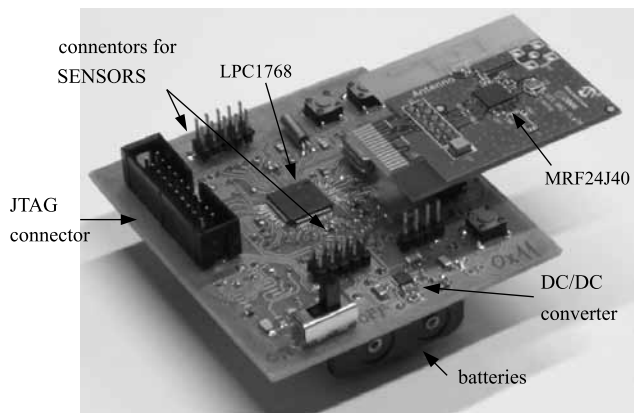

Fig. 2: SPaRCMosquito sensor node

2.2. Software - SPaRCSoft

As mentioned in section 1, wireless sensor networks use at least one base station. A base station is computationally more powerful, with more available resources than standard sensor nodes. In the case of using centralized algorithms (e.g. topology, routing, addressing), the base station normally calculates them. The base station is not normally battery powered, so the energy consumption limitations for the BS do not stand.

In a typical sensor network application, the sensor nodes deployed in the field have low CPU power, limited resources and most importantly: limited power supply. The majority of algorithms (MAC, topology, routing) for WSN are designed for preserving battery power.

Frame	Time(us) +1816512	Len	MAC Frame Control	Seq Num	Dest PAN	Dest Addr	Source Addr	Invalid Data		FCS		
00001	=1816512	15	0x8841	0x05	0x1234	0x0005	0x1111	0x25	0x25	RSSI 0xEB	Corr 0x69	CRC 1

Fig. 3: Data frames used in AeWSN.NET

Software covering the AeWSN.NET can be divided into three main parts:

- Software for the SPaRCMosquito (also referred as node firmware).
- Base station software, including BS firmware and communication protocol to the PC.
- SPaRCSoft, base station and utility software.

SPaRCSoft and all other program components are still the subject of on-going research. Because of this, new modules and algorithms are added weekly.

Wireless communication in AeWSN.NET is based on IEEE 802.15.4. standard /11/. All sensor nodes (including base stations) are using the MRF24J40 module for communication. MRF24J40 is a ZigBee compliant transceiver but, in our case, only data frames with short addressing fields are used (Fig. 3) /11/.

For developing localization, topology, and routing algorithms, the ZigBee or the MiWi stack is too large and complex; therefore we implemented our own, simple algorithms.

2.2.1. SPaRCMosquito firmware

The SPaRCMosquito is, as mentioned in section 2.1.2, based on Cortex 1768 CPU (ARM7 architecture). The programming of a processor is done in ANSI C language with the use of KEIL development tools. The main parts of the software are drivers: for communication with the radio MRF24J40, sensor part drivers, boot loader (a custom boot loader is used for flashing purposes as explained below), and the main application, including topology controls, and routing.

When deployed, the sensor node becomes part of the wireless network. Testing, routing, and topology algorithms on already-deployed networks can be difficult if the firmware can't be replaced remotely. It is for this reason that why we are developing sensor node(s) which can be reprogrammed online (upgraded with any new version of the firmware). If we want to upload new firmware on the sensor node, we must reprogram the microcontroller's flash memory with new firmware. The Internal LPC's flash memory 512KB with external 1MB memory flash has been extended for this purpose. We have developed an "extended" bootloader which flashes the ARM from firmware on the external memory flash.

New firmware is transferred from base station to each sensor node wirelessly. Each sensor's node stores new firmware in external flash memory. When done, the first byte flashed on the external flash is marked as 0x01 (new firmware). The program running on the ARM resets the

ARM. When entering our own bootloader, first, the check of the first byte on the external flash is made. If the first byte is set to 0x00 the ARM boots normally, otherwise (if the first byte on the external flash is set to 0x01), code in our bootloader copies firmware from the external flash to ARM internal flash, clears the first byte on the external flash, and moves the program counter to the start of the program just flashed.

2.2.2. SPaRCSoft

SPaRCSoft is the main application in the AeWSN.NET system. WSN modeling, testing, and evaluating is done using this application. It is also a gateway to the WSN base station. SPaRCSoft runs on a PC and can be connected to a WSN base station via USB /12/, /13/. The software is modularly based, and currently consist of eight modules (Fig. 4) working together.

The I/O module is the SPaRCMosquito interface. Currently SPaRCMosquito is connected as a virtual com port (VCP) to the PC. The I/O module frames the data from the application module and sends it towards the base station or receives the data, creates an identical data structure, as seen in Fig. 4 and then forwards it to the application module.

Application module contains the firmware for the base station. Due to firmware, the BS hardware module can act as a base station, regular module, analyzer module (like Microchips Zena), and a sniffer. All higher modules communicate with the application module.

Remote firmware upgrade module reads the binary file using the nodes firmware and distributes it over the network as stated in section 2.2.1.

Web server module is used for accessing data over the internet (e.g. reading temperature or moisture).

WSN properties module uses evaluation metrics for evaluating protocols if necessary.

SPaRCGraph module calculates different topology and routing algorithms and distributes the virtual topology over the network. Data for simulating are available through this module.

Meta data module prepares data and information for simulating in OPNET or for firmware development.

Internal settings for the modules are, if necessary, all read from the XML. Users can change it to XML or in SPaRCSoft GUI, if offered. Some settings (like com port settings) can only be changed only in XML.

The basic structure of the SPaRCSoft is a mathematically defined undirected graph G = (V, E, W) with vertexes (sensor nodes), edges (communication links between them), and weights (function of channel properties, delay and similar). The graph model is used for all the protocol calculations. SPaRCSoft can work online (connected to the real network) or offline (as a modeling and analyzing tool). When working online, sensors can be visualized as a graph on the SPaRCSoft graphic panel. Nodes are randomly distributed and the link shows the nodes neighbors. Of course, the graph can be imported (for example TSPLIB), created by the user or created randomly (working offline). When the basic structure is created (or imported) calculations can be done on it. The majority of the research work is done according to topology and routing protocols, so the SPaRCSoft is prepared for the mentioned topics. From the ISO/OSI perspective the physical and data link layers are implemented on the MRF modem (PHY and MAC). Higher layers (topology, routing) are implemented in the application module.
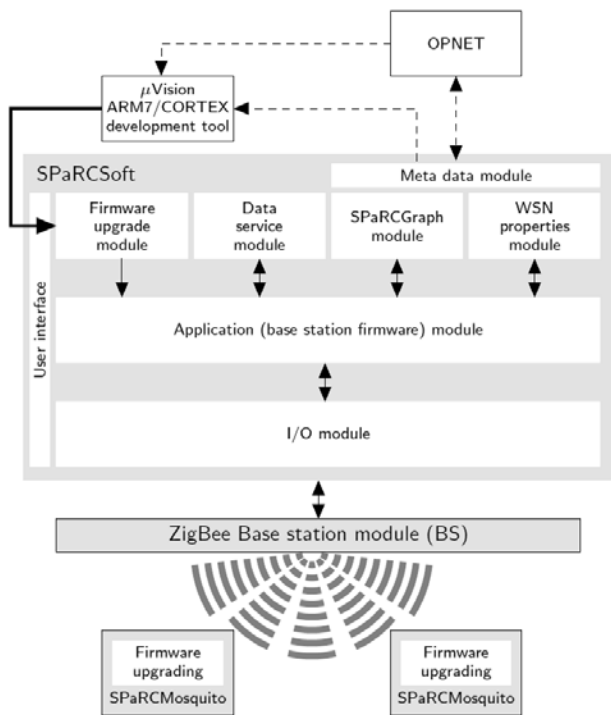

Fig. 4:   SPaRCSoft modules

Let's assume that 10 wireless nodes and the base station are in WSN at the moment and the initial phase of creating the network is over. The network topology is shown in Fig. 5. All nodes are transmitting at 100% of their power. The circle around node 10 represents its communication radius without channel properties – the gray color. The communication radius with logarithmic channel model is displayed in the green color. We decided that simple topology routing (minimum spanning tree - MST) would be used. SPaRCSoft firstly calculates MST, after that the software calculates the communication radius reduction for every node that still guarantees the MST topology (Fig. 6). Information about

the topology and routing is flushed over the network and the network can be turned into a running mode. It can be seen that node 2 energy was reduced by 50%, and if the free space propagation model is used /14/ Eq.1, energy saving can be simply calculated.

$$P_r = C_f \frac{P_t}{r^2}$$

(Eq. 1.)

Where P_r = received power, C_f = transceiver characteristics, P_t = received power, r = distance.
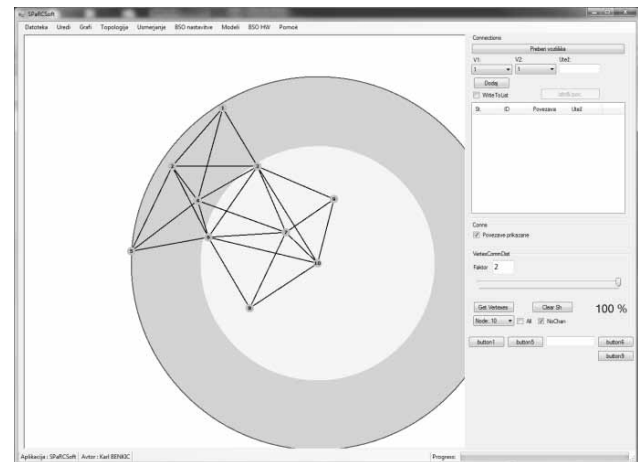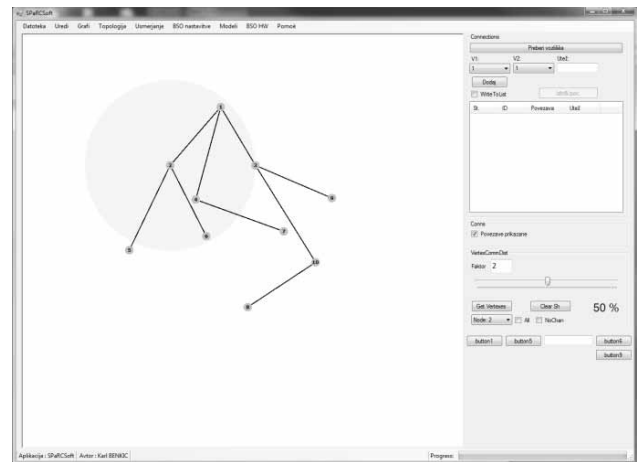

Fig. 5:   WSN topology

Fig. 6:   Calculated "virtual" topology

Topology control is practically done using changing transmission power. If all the MRF module features were be used, the channel number could be used for topology control (in the sense of creating links with different channel numbers). The SPaRCGraph module, in the case of topology control calculates transmitting power of every node that still enables desirable topology (e.g. Connected, MST, RNG, minR) /14/. Energy consumption, from the topology point of view, mainly depends on the transmitting power. Some examples showed us that two hops are less energy-demanding that only one /14/, but achieving a minimum number of hops within a network can sometimes be one of WSN properties goals. This is why we are convinced

that topology control is an important factor in developing WSN routing.

3. Application example - Localization

All data from the sensor's field are usually collected on the base station and this data is usually meaningless without positional information. Therefore, the node's location or position estimation has been a very interesting research topic over the last few years. Position estimation facilitates applications, such as inventory tracking, intruder detection, tracking of fire-fighters or miners, home automation, and patient monitoring. There are many techniques for determining the distances between nodes. Physically, we can measure the time of a signal (acoustic or RF) arrival, the angle of the signal arrival or power of the received signal. Our research focused on measuring the strength of the received signal (RSSI - Received Signal Strength Indicator). The RSSI technique was chosen due to its integration in most 802.11 radio modules. RSSI practically allows us to calculate the received power for each received packet. This parameter can be used together with path-loss and shadowing model for distance estimation.

A centralized algorithm is used for calculating the coordinates of the sensor's nodes. The base station sends RSSI parameters from the entire sensors field (all the nodes) to the PC. Then the PC calculates all the coordinates of the sensors within the network. The packets consist of next data: addresses from two neighboring nodes and RSSI between them. The algorithm calculates the average value of the last 20 measured RSSI and calculates the distances between nodes using one of the appropriate path-loss models (Fig. 7). The first three calculated distances be-
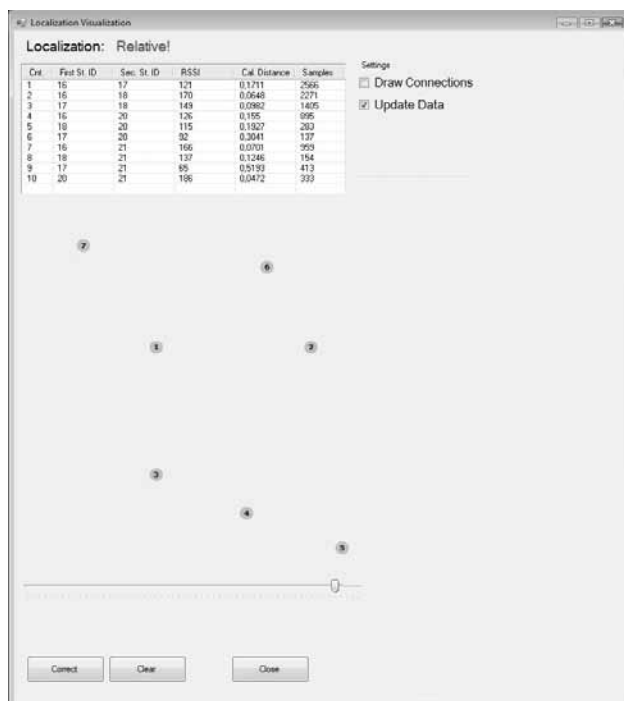

Fig. 7: SPaRCSoft module

tween the nodes creates three reference nodes (anchors or beacons). When we have reference nodes it is easy to calculate other node's coordinates.

3.1. Localization error

During the experiments we discovered that the relative localization error could reach up to 30%. In a typical radio link transmission, waves are reflected and obstructed by all objects illuminated by the transmitter antenna. Calculating the distance within realistic environment is a very complex task. Relative errors occur because of this. Fig. 8 shows relative errors from three different scenarios calculated from ideal models and real measured values /15/.
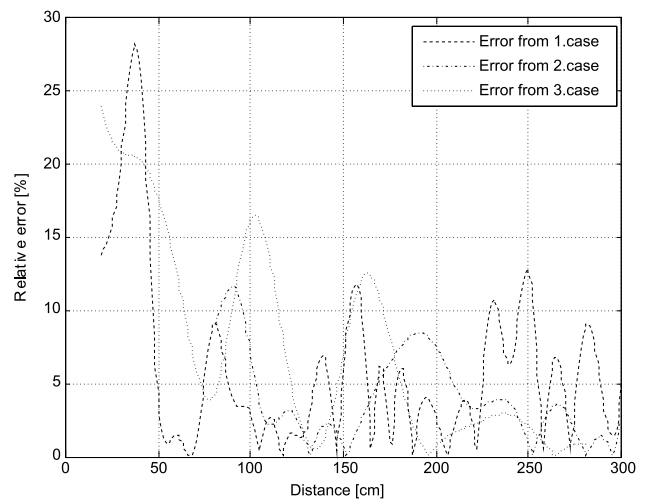

Fig. 8: Localization error

4. Conclusion

In this article, an overview of a wireless sensor network platform called AeWSN is done. Nowadays wireless sensor networking is a very promising, rapidly growing research field. Therefore, many vendors offer wireless transceivers (based on IEEE 802.15.4) or complete wireless sensor nodes (MicaMote, iMOTE2…). Despite this, we decide to develop our own wireless sensor node for the AeWSN platform. Developing our own platform gives us the freedom to simply modify the hardware and/or the software to our needs for research or project work, not to mention the experience and knowledge gained during the hardware and software development. AeWSN is still a subject to an ongoing research and development project. Our main goal is to fulfill an AeWNS platform with OPNET simulator node model, which would have the same characteristics as SPaRCMosquito. When the project is stable enough we are planning to launch a web site and making AeWSN a public open-source platform. Finally a simple localization application example is demonstrated as a case study, as to how AeWSN platform works.

Bibliography

/1/ Z. Alliance. (2010, Mar.) ZigBee Alliance. /Online/. http://www. zigbee.org/

/2/ B. Ames, »Electronics are central to 21st century warfare tactics,« military and Aerospace Electronics, 2004.

/3/ H. Dai and R. Han, »A node-centric load balancing algorithm for wireless sensor networks,« in Global Telecommunications Conference, 2003.

/4/ OPNET. (2010, Mar.) OPNET. /Online/. http://www.opnet.com/

/5/ OMNET++. (2010) Simulation Models. /Online/. http://www. omnetpp.org/models

/6/ L. Hogie, P. Bouvry, and F. Guinand, "An Overview of MANETs Simulation," Electronic Notes in Theoretical Computer Science, 2006.

/7/ D. Cavin, Y. Sasson, and A. Schiper, "On the accuracy of manet simulators," Proceedings of the second ACM international workshop on Principles of mobile computing, pp. 38-43, 2002.

/8/ Microchip. (2009) MRF24J40. /Online/. http://www.microchip. com/wwwproducts/Devices.aspx?dDocName=en027752

/9/ T. Instruments. (2009) Low Power RF ICs - 2.4GHz - CC2500 - TI.com. /Online/. http://focus.ti.com/docs/prod/folders/print/ cc2500.html

/10/ M. Malajner, K. Benkič, and Ž. Čučej, "Implementacija sprejemno/oddajnega modula CC2500 za uporabo v brezžičnih senzorskih omrežjih," in Zbornik šestnajste mednarodne Elektrotehniške in računalniške konference ERK 2007, vol. A, Portorož, 2007, pp. 140-143.

/11/ D. Gislason, ZigBee Wireless networking. Elsevier, 2008.

/12/ K. Benkic, M. Malajner, A. Peulic, and Z. Cucej, "Academic education Wireless Sensor Network: AeWSN," in Proceedings ELMAR, Zadar, 2008, pp. 535-538.

/13/ K. Benkic, M. Malajner, and Z. Cucej, "AeWSN.NET: framework for the wireless sensor networks," in New Master curricula and EU practice : proceedings, Niš, 2008, pp. 91-94.

/14/ P. Santi, Topology control in Wireless Ad Hoc and Sensor Networks. John Wiley & Sons, Ltd, 2005.

/15/ M. Malajner, K. Benkič, P. Planinšič, and Ž. Čučej, "The accuracy of propagation models for distance measurement between WSN nodes," in In Proceedings of 16th International Conference on System, Signals & Image Processing, vol. 3, Chalkida, Greece, 2009.

mag. Karl Benkič, mag. Marko Malajner, prof.dr. Žarko Čučej
Fakulteta za elektrotehniko, računalništvo in informatiko Maribor, Smetanova 17, 2000 Maribor

THZ IMAGING SYSTEM FOR HIDDEN OBJECTS DETECTIONS

Andrej Švigelj, Janez Trontelj

University of Ljubljana, Faculty of electrical Engineering, Ljubljana, Slovenia

Key words: THz sensor array, bolometer, THz imaging, Hidden objects detection

Abstract: The motivation of the work is to develop a flexible and low cost THz imaging system which can be used for various security applications. The key element is therefore a room temperature operation of THz sensor element capable to be integrated into a sensor array. The selected sensor is antenna-bolometer type which can be fabricated with micro-system and micromachining technologies based on silicon wafer substrate allowing low-cost mass production. These fabrication technologies are available in Laboratory for Microelectronic at Faculty of Electrical Engineering. Additional electronic and signal processing is described in the paper providing THz image. The complete system is described and results of THz images are presented.

THZ vizijski sistem za odkrivanje skritih predmetov

Kjučne besede: Polje THz senzorjev, bolometer, THz vizijski sistem, detekcija skritih predmetov

Izvleček: Cilj dela je razvoj prilagodljivega in cenovno ugodnega THz vizijskega sistema ki se lahko uporablja v številnih aplikacijah, predvsem pa v varnostne namene. Ključni element sistema je delovanje THz senzorskega elementa pri sobni temperaturi in možnost integracije elementa v polje THz senzorjev. Izbrani senzor je tipa antena-bolometer, ki je lahko izdelan s tehnologijo mikrosistemov na osnovi silicija, ki omogoča nizkocenovno masovno proizvodnjo. Takšna tehnologija je na voljo tudi v Laboratoriju za mikroelektroniko na Fakulteti za elektrotehniko. V prispevku je opisan celoten sistem, skupaj z dodatno elektroniko in procesiranjem signalov, ki omogoča izdelavo THz slike. Na koncu so prikazani tudi rezultati slik dobljenih z opisanim sistemom.

1. Introduction

One of the most important benefits of the THz radiation is that its photons have low energies and do not cause harmful photo-ionization in biological matter. The mm Waves are also known for good penetration through different materials, like clothes, paper, plastic, ceramic. /1/ Different materials can also be identified by their specific spectral response in THz region. This makes mm waves very useful in many applications such as industrial process inspection, pharmaceutical product inspection, radar applications, high speed communications, biomedical imaging and security purposes like explosive detection and THz imaging instead of X-ray imagers.

A THz low cost imaging system for hidden objects detection which is capable of detecting a hidden object through multiple layers of different types of clothes is presented. It is capable of producing the image of size up to 32x32 pixels. The image is processed and observed on laptop computer with near real time image refresh rate.

2. THz imaging system design

The concept of a THz vision system is based on the reflected pattern of THz waves from the target. In figure1 the complete system is shown. It consists of a THz continuous wave source emitting at 0,3THz with an output power nominally 1mW. The reflected waves from the target are gathered with a Fresnel type lens with diameter of 250mm. The detector pixel array of 16 detectors positioned in a horizontal line is processed in parallel, while the vertical scanning is processed sequentially to cover the array of 16 x 16. The goal is to obtain a full 256 pixel array. The physical size of

the detector array is therefore 27 mm x 27 mm. The signals from the array are processed with a laptop using National instruments USB-6251 Mass Term 16-Bit, 1.25 MS/s M Series Multifunction DAQ and Lab View based software.
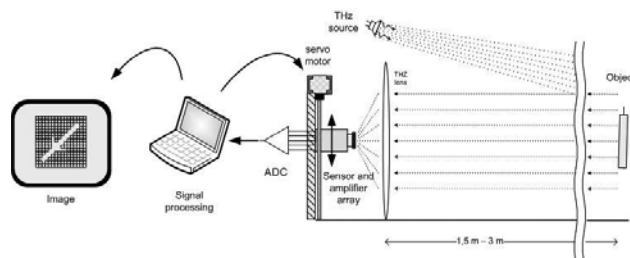

Fig. 1: THz imaging system

2.1. Pixel design

For the THz pixel a bolometer operating at room temperature has been chosen. In the literature the best NEP figures for a bolometer are in the range of hundred of pW$\sqrt{Hz}$. As our target is in 1.5m – 3m away from the THz source and detector, such figures are not acceptable.

A novel antenna and bolometer THz pixel has been developed with a NEP value in the range of 20 – 30 pW$\sqrt{Hz}$. /3/ Such figure is actually extending state of the art for room temperature THz sensors. The bolometer is fabricated on a silicone-dioxide foil with a thickness of 2 µm, the bolometer element is lifted above it with the dimensions of 10um x 1um. The sensitivity figure for such element is close to 100V/W, the bolometer resistance is 300Ω. It has been proved that the noise voltage corresponds to Johnson noise of 300Ω resistor. The bias current of the bolometer is 1mA which increases the operating temperature for about 30

degrees above the ambient temperature. Fig.2 shows the antenna bolometer photog
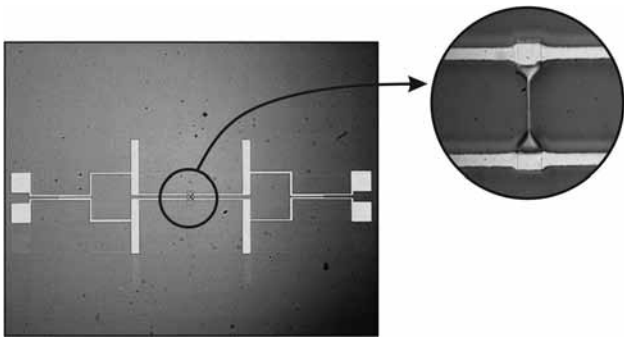

Fig. 2: Photomicrograph of antenna-bolometer

2.2. 4x1 pixel array

An array of 4 x 1 pixel array has been designed and fabricated to provide a building block for larger array. The antenna dimensions are roughly 1mm x 1mm, providing effective area of 1mm². The 4X1 pixel array was fabricated in LMFE using its micro system and micromachining facilities. The pitch was selected to be 1,7mm to allow an easy way to join the 4x1 to a larger pixel matrix. Figure 3 shows a test PCB containing the 4x1 pixel array.
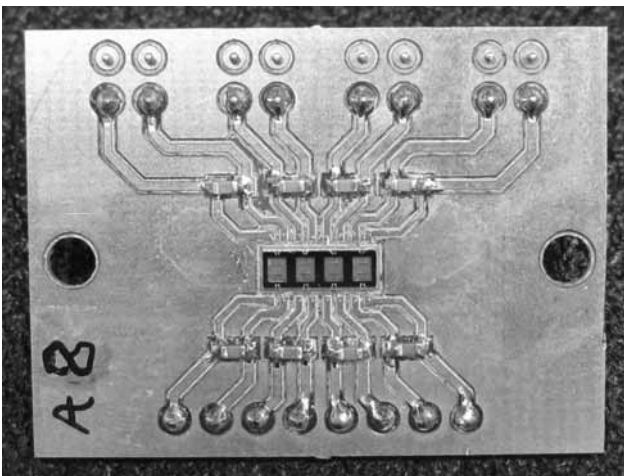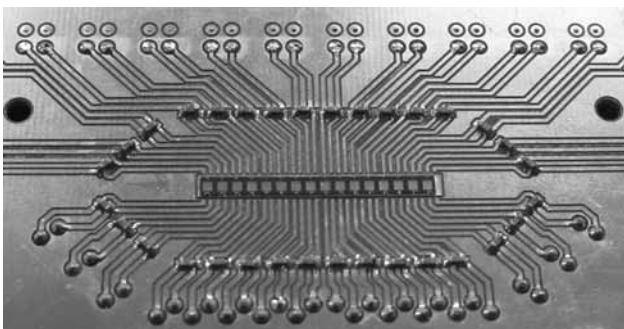

Fig. 3: 4x1 pixel array

Fig. 4: Linear array of 16 pixels

2.3. 16x1 pixel array

A Linear array of 16 pixels, assembled with four parts of 4 X 1 arrays, together with connection wires and capacitors for ESD protection is shown on Figure 4. To minimize the number of electrical joints, the contacts from bolometers are bonded directly to PCB board which has to be gold-plated to allow gold wire ball bonding.

Figure 5 shows a photo of the final 16 pixel array together with the associated bolometer biasing and amplifying electronics.
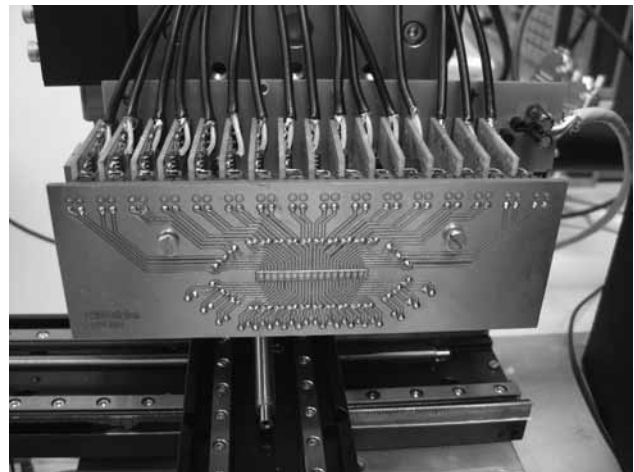

Fig. 5: linear array of 16 pixels with pixel electronic

2.4. Amplifier

The most critical element is LNA (Low noise amplifier) /2/ which should generate lower noise compared to bolometer nose. The measured noise of the amplifier is close to 5nV$\sqrt{Hz}$ at 300 Hz which is the chopping frequency of the THz source. The amplifier is AC coupled with the gain transfer bandwidth characteristic shown in figure 7. The LNA Is connected in a close loop configuration with high pass filter to avoid the LNA offset amplification and a low pass filter to suppress high frequency noise. In figure 6 the schematics of complete electronics for one pixel is shown.
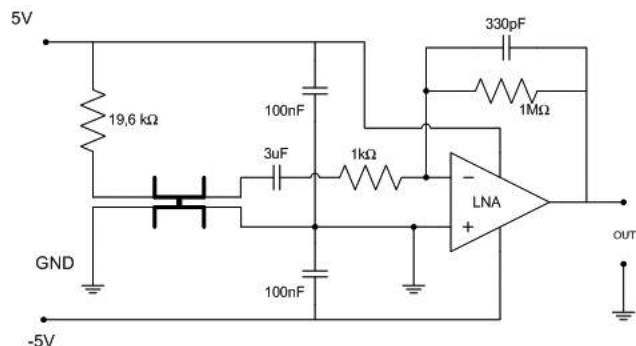

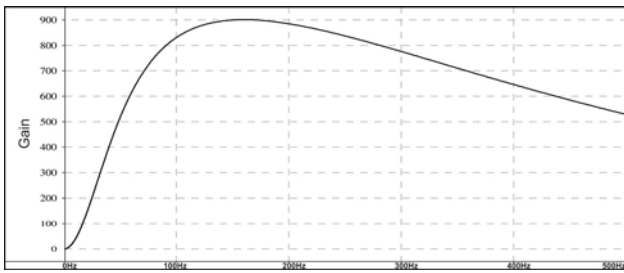*Fig. 6: Complete pixel electronic schematic*

Fig. 7:   Gain transfer bandwidth characteristics of
           amplifier

Fig. 11: FFT of signal with poor reflection

2.5. Signal Processing

Figure 8 shows a typical signal obtained on the pixel in the case that there is a fair reflected signal. If there is no reflected signal there is almost no 300Hz signal as shown on Figure 9. As seen the signal to noise ratio would need to be improved. This was done by using Fast Fourier Transform (FFT) which gave quite good result as shown in figure 10 and 11.

2.6. Mechanical scanner

To get a square matrix of 16 x 16 pixels an electro-mechanical micromanipulator is used to move the pixel array of 16 x 1 in vertical direction in 16 steps. To get a symmetrical image, the vertical step must be 1.7mm, which is the same as pixel array pitch. The scanning rate is adjustable by controlling software. The fastest scan rate is 4 seconds for full screen which gives us near real time acquisition of the THz scene. For good signal to noise ratio a longer acquisition time is recommended.

It has been introduced an increase of a pixel array to a size of 32 x 32 with additional electro-mechanical micro-manipulator which moves the 16 x 1 array of sensors in horizontal direction for a half of a pixel pitch and scanning in a vertical direction has to be done twice with 32 steps of half of pitch of the pixels

2.7. Image processing

In the described project some effort was invested into the image processing algorithms also. Each pixel is represented as a square in the image. For each square a 300 Hz component from the FFT of the measured signal is represented with 256 shades of grey. Because the difference in signal levels can be very high, compared to 256 levels, two algorithms were implemented. At first all values can be normalized in the way, that the highest value is 255. To present a larger value
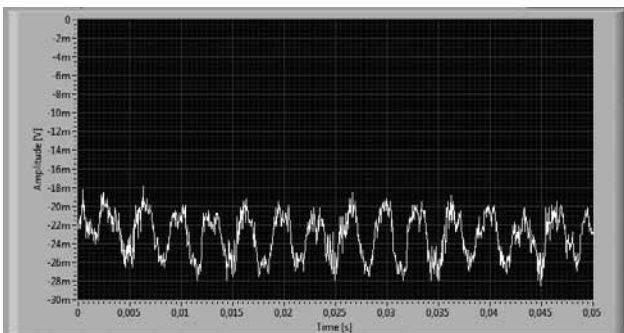

Fig. 8:   Pixel signal with good reflection
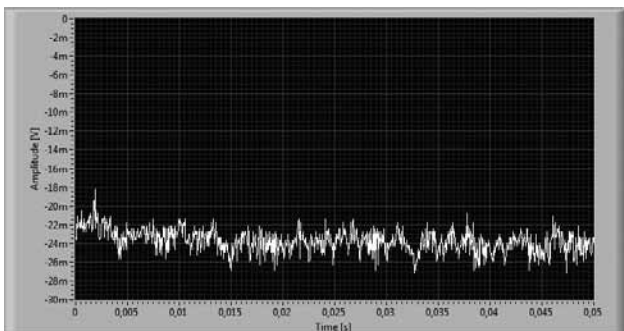
Fig. 9:   Pixel signal with poor THz reflection
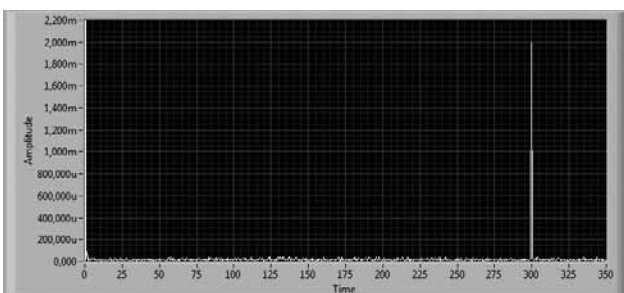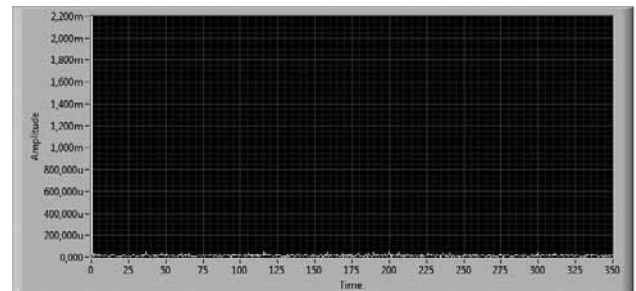

Fig. 10: FFT of reflected signal
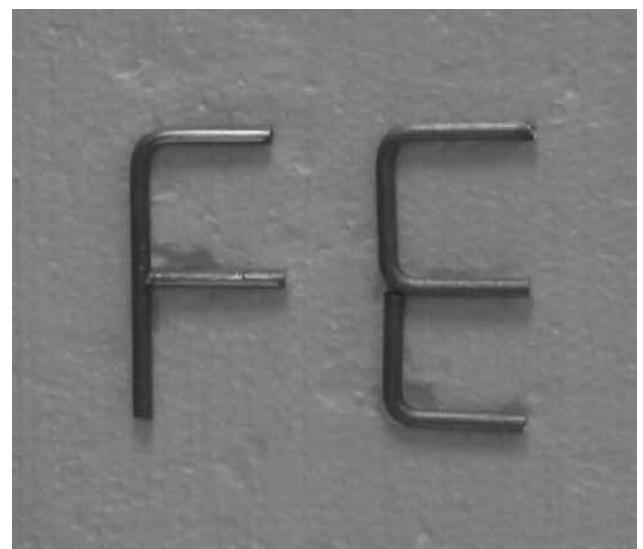
Fig. 12: Optical photo of the target

span, all values can also be exponentiated which provides the same effect as gamma correction in standard video signals

3.   Results

The raw image suffers from well known resolution limitation which is governed by the ratio of lens diameter and THz wavelength. In our case the expected resolution was no better than 1mm. An optical photo of the target is shown on figure 12 and its THz image on the figure13. For this image the pixel count was increased to 32 x 32 and only a resolution enhancement was implemented.
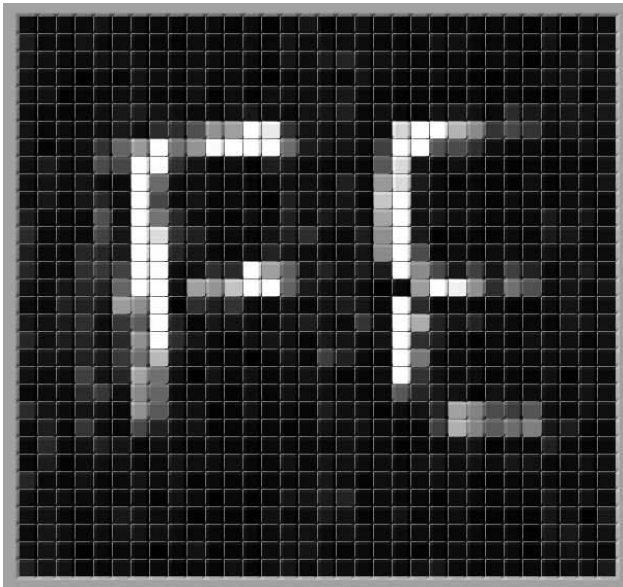
Fig. 13:   THz image of the targed

Two layers of clothes are covered over the target as shown on figure 14 and its THz image is shown on figure 15. An additional two layers of T-shirt and a towell are covered over the previous two layers of clothes as seen on figure 16. The THz radiation can penetrate through all these layers, as it can be seen from the figure 17.

Fig. 14:   Optical photo of covered target
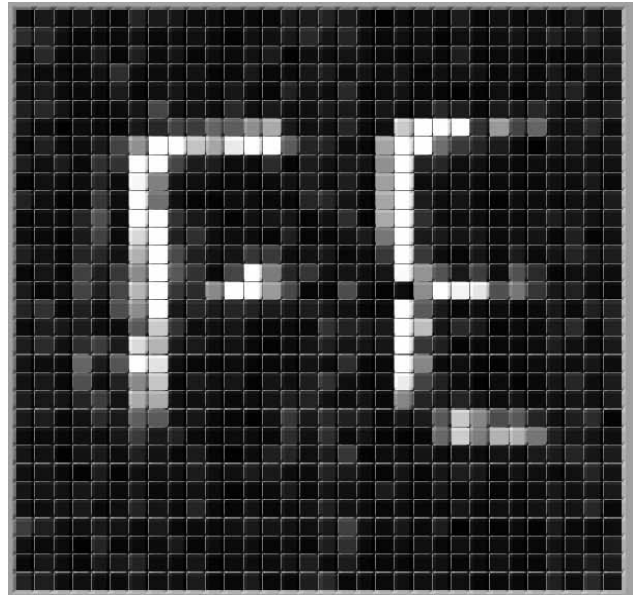
Fig. 15:   THz image of covered target

Fig. 16:   Optical photo of multiple layer covered target
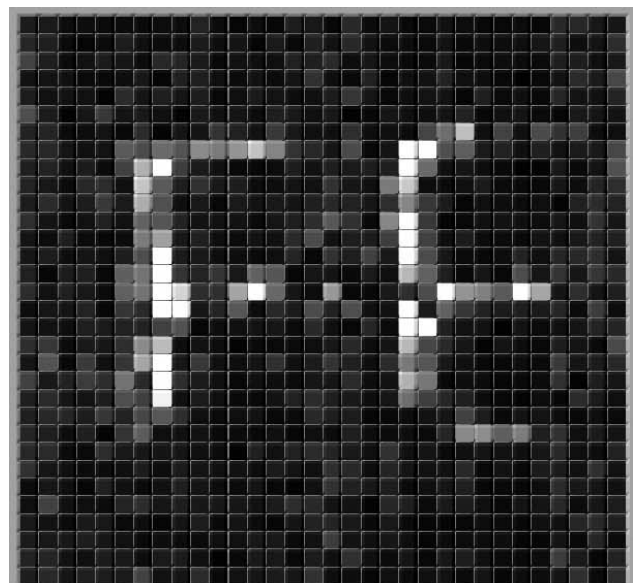
Fig. 17:   THz image of multiple layer covered target

4. Conclusions

A low cost THz antenna-bolometer type imaging sensor array of 1x4 and 1x16 has been designed, fabricated and demonstrated at room temperature conditions. A system for near real time imaging has been introduced with capability of producing the image of up to 32x32 pixels. Additional signal processing has been performed on laptop computer and the detection of the target under multiple layers of different clothes has been achieved.

5. Acknowledgements

6. References

/1/ ULRICH R. Pfeiffer, Erik Öjefors. Terahertz Imaging with CMOS/BiCMOS Process Technologies. Proceedings of the 36th European Solid-State Circuits Conference 14-16 Sep. 2010,Seville, Spain, pp. 52-60

/2/ TRONTELJ, Janez, SEŠEK, Aleksander. Ultra low noise PAGC amplifier for microsystem sensor signal processing. Inf. MIDEM, vol. 35, no. 1, pp. 8-12, 2005

/3/ Dr. Leon Pavlovič, Dr. Drago Kostevc, Dr. Anton Pleteršek, Dr. Marijan Maček, Dr. Aleksander Sešek, Dr. Janez Trontelj.300 GHz Microbolometer Parallel-Dipole Antenna for focal-Plane-Array Imaging, NATO RTO MP SET159

*Andrej Švigelj, univ. dipl. ing. el.
Univerza v Ljubljani, Fakulteta za elektrotehniko
Tržaška 25, SI-1000 Ljubljana
E-mail: andrej.svigelj@fe.uni-lj.si
Tel: (01) 4768 - 340*

*Prof. Dr. Janez Trontelj
Univerza v Ljubljani, Fakulteta za elektrotehniko
Tržaška 25, SI-1000 Ljubljana
E-mail: janez.trontelj1@guest.arnes.si
Tel: (01) 4768 – 333*

CONVERGENCE OF FIXED AND MOBILE NETWORKS BY RADIO OVER FIBRE TECHNOLOGY

Boštjan Batagelj, Leon Pavlovič, Luka Naglič and Sašo Tomažič

University of Ljubljana, Faculty of Electrical Engineering, Ljubljana, Slovenia

Key words: Radio over Fibre, remote antenna unit, cellular architecture, fibre access, fixed and mobile convergence

Abstract: This article presents a solution for the convergence of mobile and fixed access networks on the physical level that allows different service providers to share the same mobile infrastructure. A mobile cell solution is presented which features a fibre optic access infrastructure that is independent of the standard and allows the transmission of different types of broadband telecommunication traffic. For an efficient broadband network frequencies in the millimetre-wave range need to be used (30 – 300 GHz) and the cell size needs to be reduced to a pico (100 m) or even femto (10 m) of a cell.

The network presented is based on the transmission of a radio signal over optic fibre, namely 'Radio over Fibre' (RoF). The goal is to transfer complex signal processing functions from the base station to the central station. This decreases the costs of remote antenna units in the base station, making a larger number of picocells a viable solution. Uneconomical radiofrequency signal processing functions such as (de)modulation, synchronisation, multiplexing, frequency hopping, spread spectrum technology and other technologies are now located in the central station. The RF signal created in the central station is distributed through remote base station antenna units which cover the picocells used by mobile users. This article also presents the key building blocks of the RoF system, such as a photodiode with an integrated antenna, an electro absorption modulator, an optic millimetre-wave generator with a phase-locked loop and an optic-controllable antenna.

Zlivanje mobilnih in fiksnih omrežij s tehnologijo prenosa radijskega signala preko optičnega vlakna

Ključne besede: prenos radiofrekvenčnega signala prek optičnega vlakna, oddaljena antenska enota, celična arhitektura, vlakenski dostop, fiksno in mobilno zlivanje

Izvleček: V članku je predstavljena rešitev za zlitje mobilnih in fiksnih dostopovnih omrežij na fizičnem nivoju, kar omogoča različnim ponudnikom storitev souporabo iste prenosne infrastrukture. Predstavljena je mobilno-celična rešitev z optično vlakensko dostopovno infrastrukturo, ki je neodvisna od standarda in omogoča prenos raznovrstnega širokopasovnega telekomunikacijskega prometa. Za učinkovito širokopasovno omrežje je potrebno uporabiti frekvence v milimeterskem valovnem področju (30 – 300 GHz) in zmanjšati velikost celice na piko (100 m) ali celo femto (10 m) celice.

Osnova predstavljenega omrežja je prenos radijskega signala preko optičnega vlakna (angl. Radio over Fiber – RoF), katerega cilj je premestitev kompliciranih funkcij za obdelavo signalov iz bazne postaje na centralizirano postajo. S tem se zmanjšajo stroški oddaljene antenske enote v bazni postaji, tako da je večje število pikocelic smotrna rešitev. Potratne radiofrekvenčne signalno procesne funkcije, kot so (de)modulacija, sinhronizacija, razvrščanje, frekvenčno skakanje, tehnike razširjenega spektra in ostale morebitne so izvedene v centralni postaji. V centralni postaji pripravljen RF signal je razdeljen med oddaljenimi antenskimi enotami baznih postaj, ki pokrivajo pikocelice, kjer se nahajajo mobilni uporabniki. V članku so predstavljeni tudi ključni gradniki RoF sistema, kot so fotodioda z integrirano anteno, elektroabsorpcijski modulator, optični generator milimeterskih valov s fazno sklenjeno zanko in optično vodljiva antena.

1. Introduction

The main representatives of today's and future /1/ wireless radio communications are mobile communications and nomadic communications where the user is somewhat less mobile. There are also fixed directional radio connections and fixed one-to-multiple point radio connections, however fibre connections are the most suitable for the stationary user. This renders fixed radio connections obsolete except in cases where optic fibre lines have not yet been laid, or where telecommunication network redundancy needs to be ensured.

A fibre optic link is superior to a radio connection in both parameters of significance which determine the value of telecommunication lines /2/. The first is the range of the telecommunication line measured in units of length, where optic fibre is the absolute winner with the attenuation of 0.2 dB/km. The second parameter is link capacity which measures the amount of information transmitted in units of

time, where the optic fibre's broadband properties make it a practically bandwidth unlimited medium.

Fixed-mobile convergence is a phenomenon which involve services, applications, devices and networks. Meanwhile the service and application convergence have started already /3/, device and network convergence are still on hold since fixed and mobile industry are not ready to merge and to build an integrated radio-optical platform for efficient end-to-end service delivery with guaranteed performance. Although network convergence seems far away from nowadays techno-economical reality, this paper presents technical solutions for the convergence of mobile and fixed access network. Since the end user want to have wireless broadband access, the access network is main convergence point of interest.

Today, most base stations are connected to central stations via fibre optics, using the Plesiochronous Digital Hierarchy (PDH), Asynchronous Transfer Mode (ATM) or IP transfer systems. The base station is where conversion

to radio frequency occurs, bringing a broadband signal to the user's mobile station, as illustrated in Figure 1. Across greater distances, transmission from the central station to the base stations is achieved via fibre optics. Across smaller distances within the cell area transmission from the base station equipped with an antenna unit to the user is achieved wirelessly using radio waves.
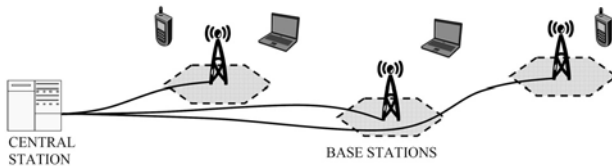

Fig. 1:   Network segmentation by picocells.

For short-range communications, the frequency range of around 60 GHz has been identified, which is the absorption peak of oxygen molecules. Since atmospheric attenuation for millimetre waves is high, radio propagation is limited to small area. For an efficient broadband network frequencies in the millimetre-wave range need to be used (30-300 GHz) and the cell size needs to be reduced to a pico (100 m) or even femto (10 m) radius of a cell.

In the new radio frequency plan prepared by Electronic Communications Committee (ECC) within the European Conference of Postal and Telecommunications Administrations (CEPT) /4/, it is clearly evident that frequency bands from 57 GHz to 66 GHz are used for broadband data transmission. The 62 GHz to 63 GHz band is reserved for land mobile broadband connections. The 60 GHz band is highly suitable for use in home communication /5/ where we can already see the first examples of its commercial use.

2.   Radio over Fibre

The basic idea of technology which allows the transmission of a radio frequency (RF) signal over fibre (Radio over Fibre - RoF) is a simple combination of fixed fibre and mobile RF transmission. The transmission of an RF signal over fibre using optical media /6/ is viable where the network is accessible to the end-user wirelessly using the cellular network.

The common principle, which has been in use for a number of years and can be seen in most currently available commercial cellular networks, is illustrated in Figure 2. Optical fibre is used as an effective substitute for a twisted pair or coaxial cable. Through an optical line, comprising an emitting laser diode (LD) and photodiode (PD) transmission is achieved with PDH or ATM, which in recent times are being replaced by IP. With this type of solution the transition from wired to wireless transmission requires a complex signal conversion at each base station. Frequency mixers and a reference RF oscillator are used to up-convert the baseband signal into the modulated carrier needed for the wireless transmission. This network architecture is complex and uneconomical due to its large number of cells.
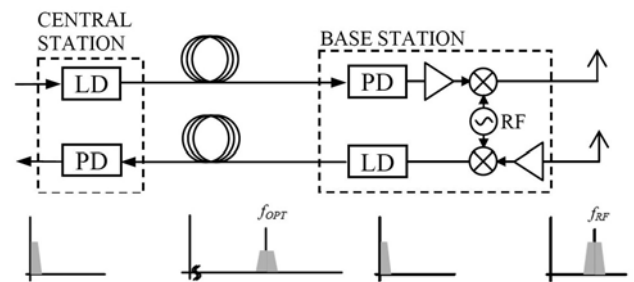

Fig. 2:   Transmission over fibre in the baseband and signal processing at the base station.

A fibre optical line with a large bandwidth allows the transmission of data signals directly over the RF carrier. In this way complex signal conversions at the base station side can be avoided. The complex signal processing functions are transferred from base stations to the central station. Thus, radiofrequency signal processing functions such as (de)modulation, synchronisation, multiplexing, frequency hopping, spread spectrum technology etc are now carried out at the central control station. The transmission of broadband signal above described is illustrated in Figure 3. In a practical network with a large number of terminal base stations and a small number of central stations, the above type of RoF transmission brings a significant economical advantage.
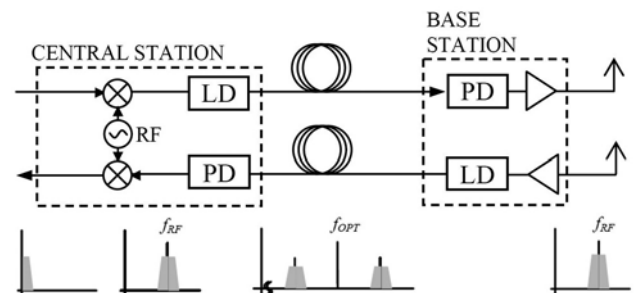
Fig. 3:   RF signal transmission over fibre and signal processing at the central station.

A transmission from the central station to individual base stations can be made also over a single optic fibre using wavelength-division multiplexing (WDM), as shown in Figure 4. However, from a practical standpoint the dual-fibre concept is easier to implement.
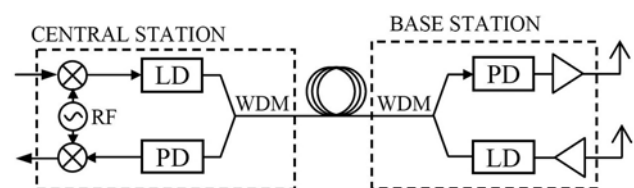
Fig. 4:   RF signal transmission via an optic WDM connection.

It makes sense to use the same antenna for signal transmission and reception at the base station where the transmission and reception signals are joined/divided via a

micro-wave circulator (Figure 5). In this case, the base station contains a laser, photodiode, circulator, RF amplifiers, control unit and power circuitry. Although it is all packed into a small casing, the unit is still quite complex.
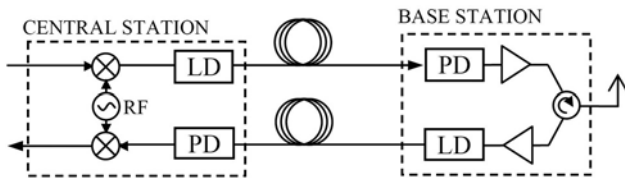
Fig. 5:   RF signal transmission via fibre optic and transmission and reception via a single antenna.

In order to reduce the number of elements, it was proposed to replace the laser, photodiode and circulator with a single semiconductor electroabsorption modulator (EAM) /7/. This device can act as both a receiver and transmitter. The advantage of such a solution is that a laser source is no longer necessary at the base station. This makes a remote antenna unit much less complex and costly /8/.

A remote antenna unit can be further simplified (Figure 6) if radio coverage is limited to a small area. This eliminates the need for RF amplifiers and the electroabsorption modulator can operate without any biasing. In this case, the base station consists only of an electroabsorption modulator and antenna /9/.
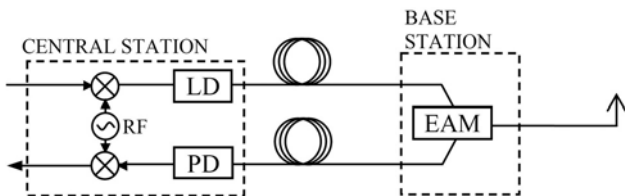

Fig. 6:   RF signal transfer via fibre optic and the use of an electroabsorption modulator.

The use of carrier re-modulation at the base station rather than a local light source is promising technique. Avoiding stabilisation and provisioning issues associated with a laser at base station is a good way of reducing installation and maintenance costs. An electroabsorption modulator integrated with a reflective semiconductor optical amplifier (R-SOA) can provide optical amplification and optical modulation in a single device /10/. As shown in Figure 7, the implementation of R-SOA with EAM into RoF system is replacing dual fibre link by only one single
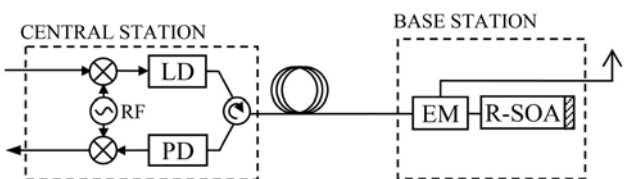
Fig. 7:   RF signal transfer via fibre optic and the use of an electroabsorption modulator and R-SOA.

It should be noted that there are certain disadvantages of processing the RF signal at the central station. Due to the broadband nature of the RF signal, it is often impossible to directly modulate the laser and therefore an external Mach-Zehnder modulator (MZM) is required. Furthermore, the amplitude modulation is highly sensitive to chromatic dispersion of the optical fibre which accumulates with the length of fibre /11/. As the optical signal is transferred across the fibre with the carrier and double sidebands, the chromatic dispersion causes a different phase delay on each of the spectral components, as shown in Figure 8.
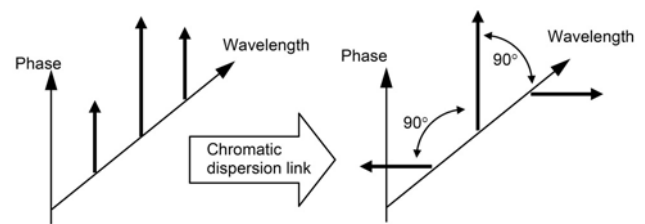
Fig. 8:   Chromatic dispersion changes the phase relationship between the optical carrier and upper and lower sideband.

The phase delay depends on the fibre length, modulation frequency and dispersion coefficient. The power of detected signal is length dependent /12/

$$P(L, f_{mod}) \propto \cos\left(\pi L c D \left(\frac{f_{mod}}{f_0} \right)^2 \right),$$

where L is the fibre length, c is the speed of light in free space, D is the fibre dispersion coefficient, f_0 is the optical carrier frequency, and f_{mod} is the frequency of subcarrier.

If the phase delay between the sidebands at the end of the fibre line is 180°, the destructive mixing on the photodiode will negate the entire RF signal, as shown in Figure 9. For an example of the standard single-mode optical fibre with a 17 ps/(nm km) dispersion at 1550 nm, a 3 dB RF signal degradation for double sideband modulation occurs at 6 km, at a 20 GHz modulation frequency. At a 60 GHz

Fig. 9:   Power penalty of the RF signal depending on the fibre length and modulation frequency.

B. Batagelj, L. Pavlovič, L. Naglič, S. Tomažič:
Convergence of Fixed and Mobile Networks by Radio over ...

Informacije MIDEM 41(2011)2, str. 144-149

modulation frequency a 3 dB degradation already occurs at 0.7 km /13/.

Direct modulation is only applicable for frequencies up to 10 GHz. For higher frequencies the limiting dispersion occurrence can be reduced by using a single sideband modulation /14, 15/ with an optic filtration or specially controlled MZM.

With detailed knowledge of the dispersion characteristics of the RoF system, the disruptive phenomenon can be used to one's advantage. In the special case of the optical regulation of an antenna array, the phenomenon is welcome as it enables control over the antenna array beam /16/.

In cases where a high level of resistance to dispersion is desired on the connection between the central and base station, the final signal processing must once again be transferred to the base station. Another reason for this is the limiting direct modulation of the laser source. Simultaneity, warless system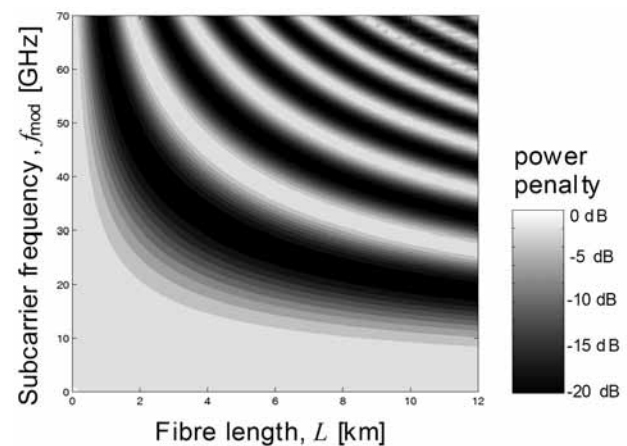s which are based on orthogonal frequency-division multiplexing (OFDM) are requiring RF signal source with high stability located in temperature regulated enviroment. Because greater complexity of the base station is undesirable, the optic generation of the carrier RF signal is recommended, as shown in Figure 10. The RF signal generation through optical photomixing eliminates the need for frequency stabilisation of the local oscillator due to the thermal dependence of the oscillation frequencies. Unfortunately, in case of presence of PMD in the transmission fibre, efficiency of RF signal is reduced or even equal to zero in the worst case. Consequently, low PMD fibre is required.
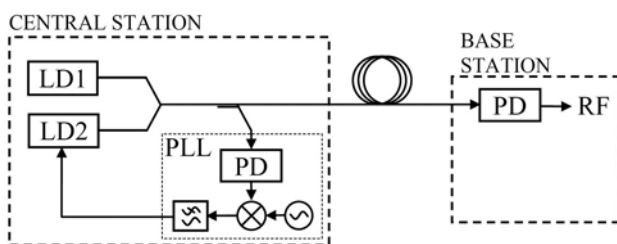

Fig. 10: Illustrations of RF signal generation through photomixing.

With separate optic carriers, the signal is transmitted from the central station over the baseband frequency. At the remote base station, the optical signals are mixed on the photodiode, creating a RF signal suitable for frequency conversion of the data signal in the mixer. The technology which uses separate optic lines for the data signal and for mixing signal is displayed in Figure 11. All optical lines can also be joined in a single optic fibre using WDM technology.

Unfortunately, power supply for amplifier and RF mixers is needed in base station location. Complication with electric power delivery can be avoided by using photonic power delivery /17/. In this case, the base station can be readily energized by high-power laser which illuminate optical energy and photovoltaic converter, as shown on Figure 12.
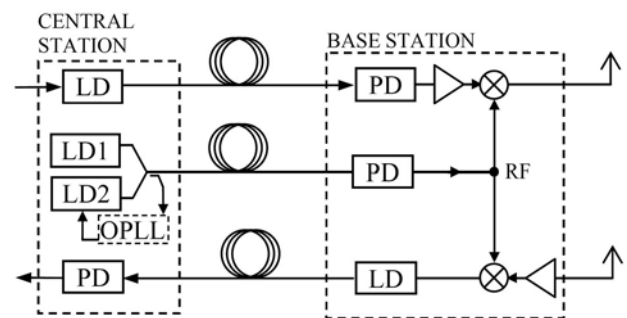
Fig. 11: Transmission by RF signal generation.

Photovoltaic cells can convert up to 50% of the incident light into electrical energy. If the wavelength of low fibre attenuation is used optical power can be transmitted up to 10 km. This approach offers total electrical isolation and independence of base station.
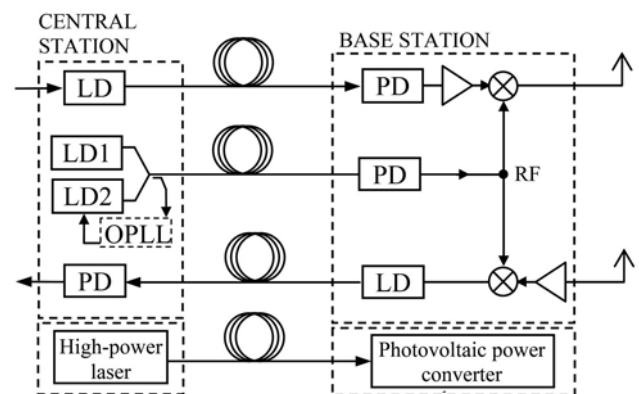
Fig. 12: Photonic power conversion delivers electric power to base station.

3. Key elements for Radio over Fibre technology

If we wish to create an RF signal through photomixing, the used photodetector needs a sufficient bandwidth for the relevant frequency area. Travelling wave photodiodes are currently the most suitable option for this /18/.

The optical carriers for photomixing can be obtained from two separate lasers where the signals are joined into a single optical fibre using an optical coupler. A dual-line laser can be used, which oscillates on two wavelengths simultaneously.

A heterodyne OPLL (Figure 13) allows the slave laser to be phase-locked to the master laser by a frequency deference equal to the frequency of the microwave reference. The offset frequency can in principle be arbitrary, but in practice is restricted by the bandwidth of the photodetector or microwave components. When the used optic sources are phase-locked there is no error signal at the phase detector output and the obtained RF signal is clear in terms of the spectrum and the phase noise. An electro-optical phase-locked loop /19/ is used for the phase locking of separate

laser sources. Even when using very narrow linewidth solid-state lasers, the complete loop delay has to be kept very small to avoid cycle slips. An electro-optic phase-locked loop is not necessary if a dual-line laser is used as the laser's structure itself ensures phase harmonisation.
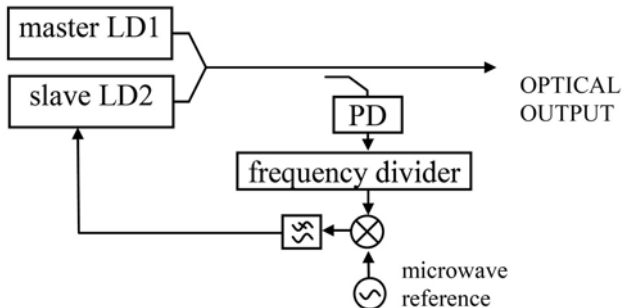
Fig. 13: Heterodyne optical phase-locked loop with frequency divider.

At the output of the photodetector, the issue of choosing a suitable waveguide arises due to the great bandwidth. In order to avoid the waveguide from the photodetector to the antenna, the photodiode can be placed on the antenna itself. As the antenna is much larger than the photodetector, the photodiode can be placed directly on the antenna's supply junction (Figure 14).

The antenna's working frequency range needs to cover the frequency area of the RF signal coming from the photodetector. As we are dealing with a broad frequency spectrum from several GHz to several THz, the antenna needs to be broadband to accommodate this.
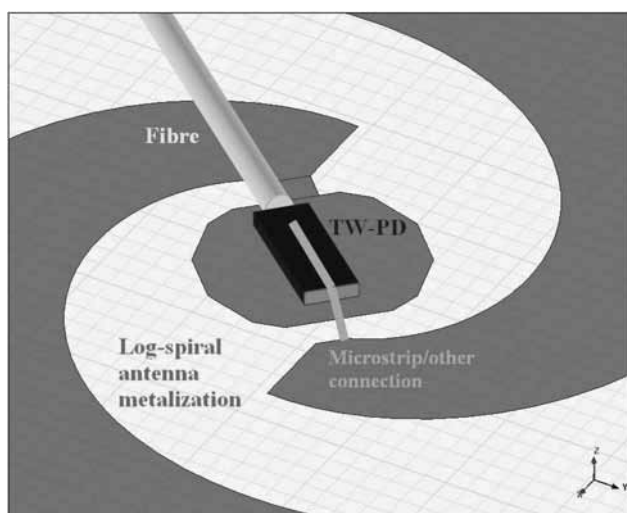
Fig. 14: Layout of the photodetector integrated with the planar antenna.

At the moment, the most appropriate option has proven to be the planar spiral antenna as it has a well-defined radiation pattern and relatively constant impedance over a broad frequency range. The spiral antenna rests on a hemispherical silicone lens (Figure 15). If the diameter of the spiral antenna is about 2 mm on a lens with the diameter of 4 – 8 mm the

usable operating frequency range is above approximately 70 GHz. The calculated radiation pattern of this structure at 100 GHz is illustrated in Figure 16.
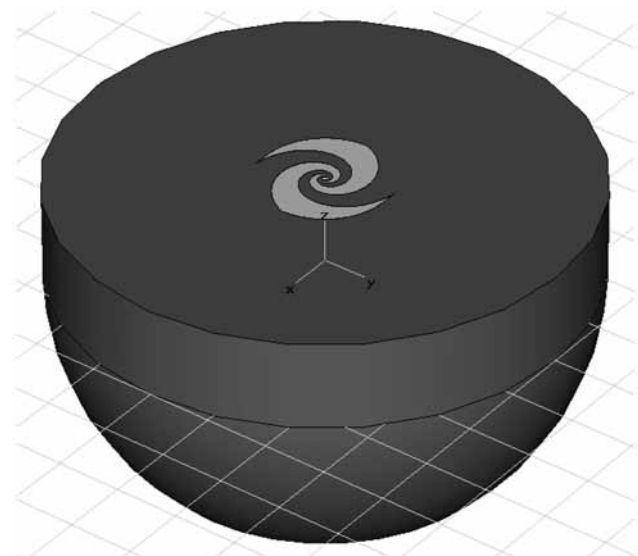
Fig. 15: Planar spiral antenna on a dielectric lens.

The antenna emits the main beam in the direction of the lens axis through the substrate and the lens. Side beams are relatively low. The gain is around 7 dBi at 100 GHz. The antenna's impedance is relatively constant and changes between 20 Ω and 80 Ω, which fits well to the impedance of the travelling wave photodetector.
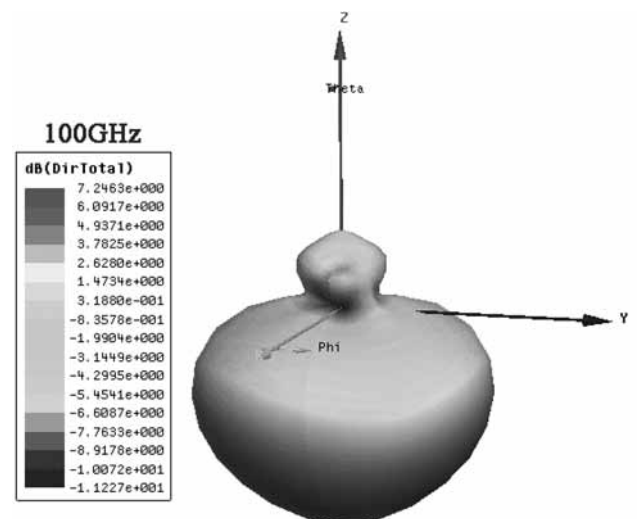
Fig. 16: Simulated radiation pattern of the spiral antenna on a hemispherical silicon lens at 100 GHz.

4. Conclusion

This article presents the convergence of mobile and fixed access network on the physical level. It describes a mobile solution based on a fibre optic access infrastructure which is standard independent. Presented convergent network

architectures are able to transfer any telecommunication protocol.

With the aim of reducing the costs of a remote antenna unit of a picocell network, the solution is based on RoF technology. The RoF system transfers complex radio frequency signal processing functions from the base station to the centralised control station. However, all signal processing concentrated at central station brings some limitations manly due to fibre chromatic dispersion.

Among the presented uses of fibre optical lines for the distribution of radio frequency signal from the central location to the remote antenna units, the most attractive solution involves the large-scale integration of electro optical components. A simple base station consisting only of an electroabsorption modulator integrated with reflective SOA and antenna is certainly the best solution and supports different types of traffic. The use of carrier re-modulation at the base station rather than a local light source has been suggested as a way of reducing installation and maintenance costs. I the case when RF signal is generated by optical mixing in base station, power supply can be delivered as photonic power what further reduce implementation costs.

The presented key building blocks of the RoF system, such as the photodiode with an integrated antenna, electroabsorption modulator, optic millimetre-wave generator with a phase-locked loop and an optic-controllable antenna have been developed as prototypes and are ready for industrialization and use in both system solutions and networks.

Acknowledgements

References

/1/ Ferdo Ivanek, 4G: Where are we going?, Informacije MIDEM, 2008, year 38, No. 3, pp. 170-174

/2/ Matjaž Vidmar, Optical-fiber communications: components and systems, Informacije MIDEM, 2001, year 31, No. 4, pp. 246-251

/3/ Marko Jagodič, Fixed-Mobile Convergence, Informacije MIDEM, 2008, year 38, No. 3, pp. 175-179

/4/ The European Table of frequency allocations for the frequency range 9 kHz to 3000 GHz, ERC REPORT 25, 2009

/5/ B. Charbonnier, P. Chanclou, J.L. Corral, G.-H. Duan, C. Gonzalez, M. Huchard, D. Jager, F. Lelarge, J. Marti, L. Naglic, L. Pavlovic, V. Polo, R. Sambaraju, A. Steffan, A. Stohr, M. Thual, A. Umbach, F. van Dijk, M. Vidmar, and M. Weiss, "Photonics for broadband radio communications at 60 GHz in Access and Home Networks," Microwave Photonics, 2008. Jointly held with the 2008 Asia-Pacific Microwave Photonics Conference. MWP/APMP 2008. International Topics Meeting , vol., no., pp.5-8, Sept. 9 2008-Oct. 3 2008.

/6/ Alwyn Seeds, Chin-Pang Liu and David Wake, Broadband Access using Wireless Over Fibre Technology, Strokovni seminar Optične komunikacije, Ljubljana, 29. - 31. januar 2003.

/7/ L. D. Westbrook and D. G. Mooie, Simultaneous bi-directional analogue fibre-optic transmission using an electroabsorption modulator, Electron. Lett., 1996, Volume 32, Issue 19, pp. 1806-1807.

/8/ Jeha Kim, Yong-Duck Chung, Kwang-Seong Choi, Dong-Soo Shin, Jae-Shik Sim, and Hyun-Kyu Yu, 60-GHz System-on-Packaging Transmitter for Radio-Over-Fiber Applications, J. Lightwave Technology, Vol. 26, No. 15, August 1, 2008, pp. 2379-2387.

/9/ D. Wake, D. Johansson, D. G. Moodie, Passive picocell: a new concept in wireless network infrastructure, Electronics Letters, Volume 33, Issue 5, 27 Feb 1997, pp. 404 – 406.

/10/ Filip Öhman, Kresten Yvind, Lotte J. Christiansen, Jesper MØrk, Christophe Peucheret, Palle Jeppesen, Monolithically integrated reflective SOA-EA carrier re-modulator for broadband access nodes, Optics Express, Vol. 14, Issue 18, pp. 8060-8064, 2006.

/11/ U. Gliese, S. Norskov, and T. N. Nielsen, "Chromatic dispersion in fiber-optic microwave and millimeter-wave links," IEEE Trans. Microwave Theory Tech., vol. 44, pp. 1716-1724, Oct. 1996.

/12/ H. Schmuck, Comparison of optical millimeter-wave system concepts with regard to chromatic dispersion, Electron. Lett., vol. 31, no. 21, pp. 1848–1849, Oct. 1995.

/13/ B. Davies, J. Conradi, Hybrid modulator structures for subcarrier and harmonic subcarrier optical single sideband, IEEE Photonics Technology Letters, Vol. 10., No. 4., pp. 600-602, Apr. 1998

/14/ G. H. Smith, D. Novak, and Z. Ahmed, "Technique for optical SSB generation to overcome dispersion penalties in fiber-radio systems," Electron. Lett., vol. 33, pp. 74-75, 1997

/15/ G.H.Smith, D. Novak, Z. Ahmed, Overcoming chromatic-dispersion effects in fiber-wireless systems incorporating external modulators, IEEE Transactions on Microwave Theory and Techniques, vol.45, no.8, pp.1410-1415, Aug 1997.

/16/ Patrik Ritoša, Boštjan Batagelj and Matjaž Vidmar, Optically steerable antenna array for radio over fibre transmission, Electron. Lett., Aug. 2005, vol. 41, no. 16, p. 917-918.

/17/ J.-G. Werthen, M. Cohen, Photonic Power: Delivering Power Over Fiber for Optical Networks, International Conference on Photonics in Switching, 2006, pp 1-3.

/18/ A. Stoehr, A. Malcoci, A. Sauerwald, I. Camera, R. Guesten, D. Jager, "Ultra-Wideband Travelling-Wave Photodetectors for Photonic Local Oscillators", IEEE J. Light. Tech, vol. 21, no. 12, 2003, pp. 3062-3070.

/19/ Luka Naglič, Leon Pavlovič, Boštjan Batagelj and Matjaž Vidmar, Improved phase detector for electro-optical phase-locked loops, Electron. Lett., Jun. 2008, vol. 44, no. 12, p. 758-760.

dr. Bostjan Batagelj
University of Ljubljana, Faculty of Electrical Engineering, Ljubljana, Slovenia
Tržaška cesta 25
1000 Ljubljana
Tel. 01 4768 400
Gsm. 031 31 8760
e-mail. bostjan.batagelj@fe.uni-lj.si

CVL OCR DB, AN ANNOTATED IMAGE DATABASE OF TEXT IN NATURAL SCENES, AND ITS USABILITY

Andrej Ikica, Peter Peer

Computer Vision Laboratory (CVL), Faculty of Computer and Information Science, University of Ljubljana, Ljubljana, Slovenia

Key words: computer vision, text detection, optical character recognition, natural scenes

Abstract: Text detection and optical character recognition (OCR) in images of natural scenes is a fairly new computer vision area but yet very useful in numerous applicative areas. Although many implementations gain promising results, they are evaluated mostly on the private image collections that are very hard or even impossible to get. Therefore, it is very difficult to compare them objectively. Since our aim is to help the research community in standardizing the evaluation of the text detection and OCR methods, we present CVL OCR DB, a public database of annotated images of text in diverse natural scenes, captured at varying weather and lighting conditions. All the images in the database are annotated with the text region and single character location information, making CVL OCR DB suitable for testing and evaluating both text detection and OCR methods. Moreover, all the single characters are also cropped from the original images and stored individually, turning our database into a huge collection of characters suitable for training and testing OCR classifiers.

Anotirana podatkovna baza slik teksta v naravnih scenah CVL OCR DB in njena uporaba

Kjučne besede: prenos radiofrekvenčnega signala prek optičnega vlakna, oddaljena antenska enota, celična arhitektura, vlakenski dostop, fiksno in mobilno zlivanje

Izvleček: Detekcija teksta in optična razpoznava simbolov (OCR) na slikah naravnih scen je razmeroma novo področje računalniškega vida, pa vendar zelo uporabna na številnih aplikativnih področjih. Mnoge implementacije dosegajo spodbudne rezultate, vendar njihova evalvacija večinoma poteka na privatnih zbirkah slik, ki so težko dostopne ali celo nedostopne, zato je metode med seboj zelo težko objektivno primerjati. Naš namen je pomagati raziskovalni skupnosti pri standardizaciji evalvacije omenjenih metod. Zato predstavljamo CVL OCR DB, javno bazo anotiranih slik teksta v naravnih scenah, ki so zajete pod različnimi vremenskimi in svetlobnimi pogoji. Vse slike v bazi vsebujejo informacijo o lokacijah prisotnih tekstovnih regij in posameznih črk, kar omogoča testiranje in evalvacijo tako metod detekcije teksta, kot tudi metod razpoznave simbolov. Vsi posamezni znaki so dodatno izrezani iz originalnih slik ter individualno shranjeni, kar naredi našo podatkovno bazo ogromno zbirko znakov, primerno za učenje in testiranje klasifikatorjev OCR.

1. Introduction

Due to a broad range of applicative areas, text detection and OCR in natural scene images have gained a lot of research interest in the last decade. Since the research area is just beginning to evolve, there are obviously no widely accepted standards for both evaluation methodology as well as the common evaluation database, as it is typical in other computer vision areas such as face detection and recognition /1,2/. Indeed, there already exist image databases of text in natural scenes such as the ICDAR database /3/. These collections, however, include only a couple of hundreds of images and are more or less intended for private use or for competitions, whereas our idea is to establish a public collection of thousands of images that would organically grow over time.

Our approach has several advantages. First, all the existing methods can be validated and objectively compared to each other on the same dataset and against the same ground-truth data. Second, with CVL OCR DB it is easy to compare the new text detection and OCR approaches with the state-of-the-art methods. Many authors claim to achieve better results compared to other (older) methods, although they often do not explicitly reveal which datasets have been used for evaluation or they simply evaluate methods on their

private datasets. Finally, CVL OCR DB is a public database, which hopefully will be expanded by a diverse number of researchers and volunteers, so all the image data will actually represent a vast variety of possible scenarios. Many researchers, unfortunately, establish their private image datasets with the drawbacks of their methods in mind. Thus, they (not being aware of) avoid integrating "worst-case scenario" images into their datasets. We already tried to avoid this issue in the process of collecting and annotating image data by intentionally including the volunteers who had no previous experience in text detection and OCR whatsoever. Therefore, the collected data were actually the images seen by an average human observer, not a computer vision expert. The results were often contrary to our expectations and included complicated fonts and styles, very complex backgrounds, characters substituted by other symbols, text skews, rotations etc.

The article is organized as follows. First, the CVL OCR DB construction life-cycle is described in section 2, followed by the description of the capturing methodology in Section 3. The conceptual model of annotation and the model implementation are presented in Section 4 and Section 5, respectively. In Section 6 the annotation process is described and in Section 7 we present the practical aspects of our database and evaluation results of several text detection
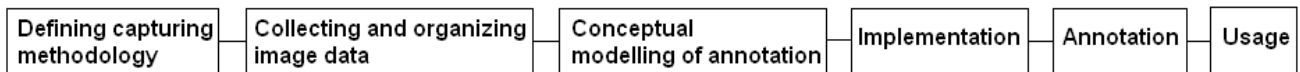
A. Ikica, P. Peer:
CVL OCR DB, An Annotated Image Database of Text in Natural ….

Informacije MIDEM 41(2011)2, str. 150-154

Fig. 1.   The CVL OCR DB construction life-cycle.

methods on the CVL OCR DB subset. Finally, the article is concluded with the discussion and the terms for using CVL OCR DB in Section 8.

2.   Construction life-cycle

The CVL OCR DB construction life-cycle is divided into 6 stages as shown in Fig. 1. After defining the coarse capturing methodology, the image data was collected and organized. Through the process of collecting and organizing the image data the methodology was constantly refined in order to capture as broader set of different scenarios as possible in the best possible way. The conceptual model of annotation developed afterwards was used for the actual implementation and the ground-truth data annotation. Finally, the last stage is dissemination and usage of the database for evaluation of different computer vision algorithms.

3.   Capturing methodology

In the image data collecting stage both the authors and the volunteers were involved. We captured a great number of images of text in natural scenes, including images of signboards, shop names, traffic signs and jumbo posters (Fig. 2). All the images were captured at varying weather and lighting conditions with either a compact camera (up to 7 mega pixels) or a mobile phone (up to 5 mega pixels), but were eventually resized to fit the computer screen. There are three main reasons for resizing the images. First, the resized (smaller) images contain enough visual information, therefore, the original (bigger) images would unnecessarily

(a)

(b)

(c)

(d)
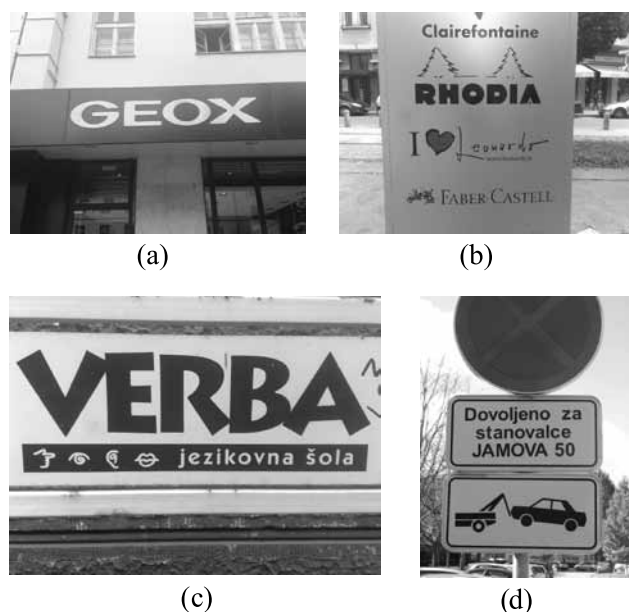
Fig. 2.   Examples of captured text images.

occupy the disk space. Second, smaller images can be processed much faster. The third reason, however, lies in the fact that precise annotation (selecting bounding polygons and cropping characters) can be performed much easier on the images that do not stretch beyond the computer screen dimensions.

All the collected images are divided into three main categories: "day", "night" and "artificial" (tree structure in Fig. 3). The "day" category corresponds to the images captured at daylight, the "night" category corresponds to the images captured at night time and, finally, the "artificial" category corresponds to the images captured on locations where only artificial light is present (eg. shopping centers). Further on, the "day" category is divided into 4 subcategories: "normal" (normal sunlight), "sun" (very intense sunlight), "fog" and "rain". Similarly the "night" category is divided into 2 categories: "dusk" and "night" (the actual night time). This top level structure is maintained in a directory structure (Fig. 3). Every leaf node of the diagram in Fig. 3 corresponds to the actual image repository for a given category/subcategory. In other words, all the images of the particular category/subcategory are physically stored in these repository directories. We will refer to these directories as data folders.
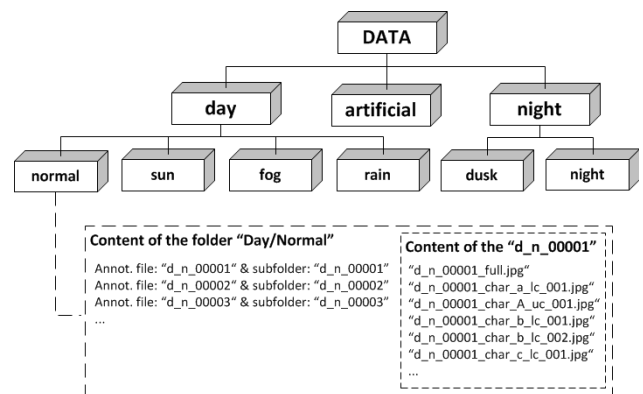
Fig. 3.   File organization of CVL OCR DB.

Each data folder contains a list of annotation files. The annotation file naming convention is the following: The filename starts with one of the following prefixes: "d_n" (day/normal), "d_s" (day/sun), "d_f" (day/fog), "d_r" (day/rain), "a" (artificial), "n_d" (night/dusk) and "n_n" (night, night), depending on the category/subcategory of the data folder. The prefix is followed by the underscore and a 5-digit image index (including the leading zeros). For example: an annotation file for a 325th image in the day/fog category is named as "d_f_00325". Similarly a 12345th annotation file in the artificial category is named as "a_12345". The 5-digit index has an upper bound of maximum 99,999 images in a certain data folder, which is more than enough for the purpose.

A. Ikica, P. Peer:

Informacije MIDEM 41(2011)2, str. 150-154   CVL OCR DB, An Annotated Image Database of Text in Natural .....

Every annotation file is linked to an actual image and a list of character images in it (Section 6 describes the process of getting the character images in the annotation stage). Both are stored in a subdirectory of the particular data folder. We will refer to these subdirectories as the image folders. The image folder naming convention is the same as the annotation file naming convention.

The actual images in the image folders are stored as JPEG files. Their naming convention is again simple and very similar to the naming convention used so far. The full image is named after the image folder it resides in and is concluded with the "_full.jpg" suffix. For example, a full text scene image in a "d_f_00325" subdirectory is named "d_f_00325_full.jpg". Single character naming convention is a little more complicated, since the single characters can occur more than once. For instance, the text scene image in Fig. 2b contains 2 letters "C", 4 letters "a" and 3 letters "A". Every character image filename starts with a subdirectory prefix followed by the "_char_<char_symbol>_<lc|uc>_<3_digit_index>.jpg" (see dashed rectangle in Fig. 3 for details), where "lc" corresponds to the lowercase and "uc" to the uppercase. For example, if our imaginary image "d_f_00325_full.jpg" consisted of 2 letters "C", 1 letter "a" and 1 letter "A", the corresponding character image filenames would be:

"d_f_00325_char_C_uc_001.jpg",

"d_f_00325_char_C_uc_002.jpg",

"d_f_00325_char_a_lc_001.jpg",

"d_f_00325_char_A_uc_001.jpg".

The "lc/uc" labels are used to avoid treating the upper and lowercase character filenames as the same filename. Without these labels some operating systems would treat "d_f_00325_char_a_001.jpg" and "d_f_00325_char_A_001.jpg" as the same filename. Moreover, the "lc/uc" labels are a great advantage when, for example, researcher wants to find all the uppercase letters in the database. The given naming convention allows a maximum of 999 of same characters per single full image, which is more than enough for the purpose.

It might seem that the proposed naming convention introduces redundant data into our methodology – the image prefixes and folder names, for example, contain the same attributes. There are two main reasons why we proposed such a naming convention. First, the category is included in the filename to exploit the operating system functionality for simple queries – all the images of a certain category/subcategory can be obtained via simple filename operating system search. Second, we want our database to be consistent even in the case of human errors – for example, when some image files are accidentally moved to other folders.

4. Conceptual model of annotation

Another added value of CVL OCR DB is the annotated ground-truth data, ie. the annotation files which correspond

to the text in images. For every image in the database there exists a corresponding annotation file. As shown on the left side in Fig. 4, every annotation file ("AnnotationFile" class) is linked to the actual image ("TextSceneImg" class) and multiple single character images ("CharImage" class) cropped from the image. Single characters can be used for OCR classifier training and testing. Fig. 5 shows an example of an image with three text regions. For clarity, cropped characters of the first region are displayed as well on the right side of the figure.
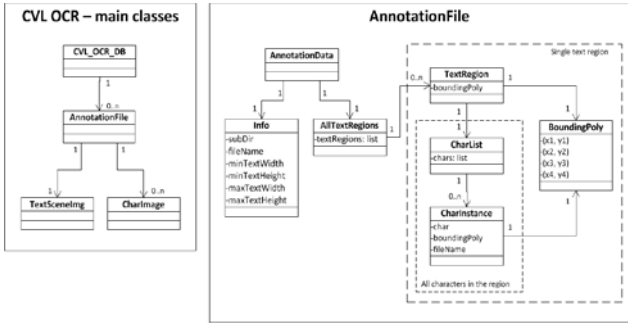
Fig. 4.   The CVL OCR DB conceptual model.

Fig. 5.   Text regions (left) and single characters of the first text region (right).

The annotation file (see the right side in Fig. 4) contains two main classes: the "Info" class and the "AllTextRegions" class. The "Info" classincludes the actual image filename ("filename"), its location ("subdir") and the size constraints (min. and max. dimensions) of the text regions present in the particular image. In the database usage stage, all the text regions detected by the text detection methods violating the size constraints are simply ignored, making the evaluation process equally fair for all the methods. "AllTextRegions" class is a list of all text regions present in the image. Each text region, namely "TextRegion" class, corresponds to the physical text region in the image and is described with a bounding polygon ("boundingPoly") and a list of characters it contains. For example, the first text region in Fig. 5 contains characters "N", "O", "K", "I" and "A". Each character "CharInstance" in the "CharList" is described with the UTF-8 character code, its filename and again with the bounding polygon.

A. Ikica, P. Peer:
CVL OCR DB, An Annotated Image Database of Text in Natural ....

Informacije MIDEM 41(2011)2, str. 150-154

5. Model implementation

Since the XML files represent a very flexible, easy-to-read data format, they are a reasonable choice for describing the annotation files. Therefore, the conceptual model was implemented in the XML Schema Definition (XSD) Language /4/. The schema defines the grammar and the XML documents that follow its rules are nothing more than words in language defined by the schema. An implementation decision was taken as well, to follow a recommendation that all tags be elements with no attributes /5/. Fig. 6 shows an XSD schema for the XML annotation files derived from the conceptual model of annotation.

Fig. 6. XML implementation of the conceptual model - XSD schema for XML annotation files.

6. Annotation

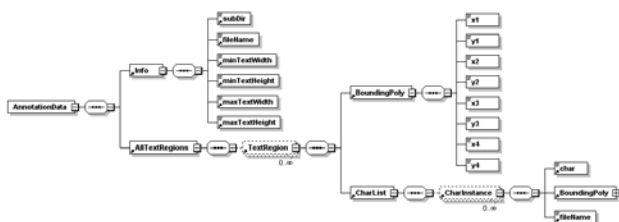For the annotation purposes a program for fast and effective annotation, namely TextAnnotator, was implemented. An average user can select multiple images, mark the text regions (with bounding polygons) and crop the individual characters. The annotation program automatically stores the image data in the appropriate data/image folders and creates new XML annotation files or updates the existing. In order to preserve database consistency, all XML annotation files are validated against the XSD schema (Fig. 6). Since the images are often affected by perspective and projective transformations, the text can appear rotated and skewed. To solve these issues, a 4-point bounding polygon is chosen (instead of a rectangular bounding box) to represent the text regions. Moreover, the rotated single characters pose a serious problem to OCR classifiers, so the cropped characters can be rotated by a human annotator by simply dragging the mouse in the desired direction.

Currently there are much over 1,000 annotated images of text in natural scenes in the CVL OCR DB. We encourage other researchers to participate in expanding the database by annotating and uploading new text scene images (see Discussion and URL sections of the article for participation details).

7. Using cvl ocr db in practice

CVL OCR DB has an enormous practical potential, since it is a step towards standardizing the evaluation approach for text detection and OCR methods on images of text in natural scenes. It is of vital importance to be able to objec-

tively compare methods on the same input images and the same ground-truth data.

CVL OCR DB has already been used to compare several text detection methods /6/. We compared our proposed text detection method based on the projection profiles /7,8/ against two other text detection methods, namely Ezaki /9/ and Shivakumara /10/ methods. The evaluation results in terms of precision p, recall r and quality measure f /6/ are shown in Table 1.

Table 1. Practical example of CVL OCR DB usage: evaluation results of different text detection methods (bigger number means better result).

Text detection method	p	r	f
Shivakumara /8/	58,7%	51,0%	54,6%
Ezaki /7/	58,0%	53,1%	55,4%
Proposed method /4/	70,9%	55,2%	62,1%

8. Discussion

In this article we presented CVL OCR DB, a public annotated image database of text in natural scenes. CVL OCR DB has several advantages. First of all, the database is public and can therefore be expanded with new images. Second, CVL OCR DB comes with the TextAnnotator program which is easy to use and enables fast database expansion without affecting the structure and internal relationships. And finally, CVL OCR DB was constructed through several iterations and revisions, so the exceptions, special cases and boundary conditions are taken into account. It is important to understand that CVL OCR DB differs from the raw image databases that contain only images and no ground-truth data whatsoever. Our database is ground-truth annotated – not only in terms of region and character locations, but also in terms of capture and lighting conditions. The important aspect is definitely its multi-functionality, since it can serve for both text detection and OCR purposes.

Our aim is to try to contribute to the research community by proposing a functional and easy-to-use framework for evaluating and comparing text detection and OCR methods. We would like to encourage the research community to participate in CVL OCR DB usage – not only for the evaluation purposes but also as active contributors who help expanding it by adding and annotating new images. All the necessary material, including text annotation program, documentation and usage agreement can be downloaded from the CVL OCR DB web portal:
URL
CVL OCR DB web portal: http://www.lrv.fri.uni-lj.si/~peterp/CVLOCRDB/.

References

/1./   Resources for Face Detection (2010). Retrieved December 20 2010 from http://vision.ai.uiuc.edu/mhyang/face-detection-survey.html#face-database

A. Ikica, P. Peer:

Informacije MIDEM 41(2011)2, str. 150-154   CVL OCR DB, An Annotated Image Database of Text in Natural .....

/2./   Face Databases (2010). Retrieved December 20 2010 from http://web.mit.edu/emeyers/www/face_databases.html

/3./   S. M. Lucas, A. Panaretos, L. Sosa, A. Tang, S. Wong, and R. Young, "ICDAR 2003 robust reading competitions", Proc. of 7th Int. Conf. on Document Analysis and Recognition (ICDAR 2003), Vol. II, 3-6 August 2003, pp. 682–687

/4./   XML Schema Definition (XSD) Language (2010). Retrieved December 20 2010 from http://www.w3.org/TR/xmlschema-0/

/5./   XML tags and attributes (2010). Retrieved December 20 2010 from http://www.oasis-open.org/cover/elementsAndAttrs.html

/6./   A. Ikica, P. Peer, "An improved edge profile based method for text detection in natural images", Eurocon 2011

/7./   J. Park, G. Lee, E. Kim, J. Lim, S. Kim, H. Yang, M. Lee, S. Hwang, "Automatic detection and recognition of Korean text in outdoor signboard images", Pattern Recognition Letters, 2010.

/8./   T. N. Dinh, J. Park, G. Lee, "Korean Text Detection and Binarization in Color Signboards", Proc. of The Seventh Int. Conf. on Advanced Language Processing and Web Information Technology (ALPIT 2008), pp. 235-240

/9./   N. Ezaki, M. Bulacu, L. Schomaker, "Text Detection from Natural Scene Images: Towards a System for Visually Impaired Persons", Int. Conf. on Pattern Recognition (ICPR 2004), vol. II, pp. 683-686

/10./ P. Shivakumara, T. Q. Phan, C. L. Tan, "Video text detection based on filters and edge features", Int. Conf. on Multimedia & Expo (ICME 2009), pp. 514-517

Andrej Ikica, Peter Peer

Computer Vision Laboratory (CVL)
Faculty of Computer and Information Science,
University of Ljubljana
Tržaška 25, Ljubljana, Slovenia
andrej.ikica, peter.peer}@fri.uni-lj.si

ZAPISNIK OBČNEGA ZBORA STROKOVNEGA DRUŠTVA MIDEM
24. 3. 2011

Predlagani dnevni red:

1. Otvoritev občnega zbora in ugotovitev sklepčnosti
2. Sprejem predlaganega dnevnega reda ter zapisnika prejšnjega občnega zbora
3. Izvolitev delovnega predsedstva, dveh overovateljev zapisnika in volilne komisije (3 člani)
4. Poročilo o delu društva v zadnjem mandatu (S. Amon, I. Šorli, I. Pompe)
5. Finančno poročilo (I. Šorli)
6. Poročilo nadzornega odbora (F. Smole)
7. Poročilo častnega razsodišča (J. Furlan)
8. Razprava o podanih poročilih in glasovanje o razrešnici dosedanjim organom društva
9. Predlogi in volitve novih organov društva
10. Poročilo volilne komisije o izidu volitev
11. Nagovor novega predsednika in predstavitev programa dela za naslednje obdobje, predlogi članov za nadaljnje delo društva in sprejem programa dela
12. Razno

1. TOČKA:
Otvoritev občnega zbora

Nagovor in pozdrav gospoda prof. dr. Andreja Žemve, prodekana UL FE.

Ugotovljeno je bilo, da sklepčnosti ni, zato se je počakalo pol ure. V skladu s statutom društva MIDEM je po pol ure občni zbor društva postal sklepčen.

2. TOČKA:
Sprejem dnevnega reda ter zapisnika prejšnjega OZ

Dnevni red je bil sprejet brez pripomb.

3. TOČKA:
Izvolitev delovnega predsedstva

Dr. Slavko Amon predlaga za predsednika delovnega predsedstva dr. Janeza Trontlja, za dva overovatelja dr. Janeza Krča in dr. Iztoka Šorlija. Za člane volilne komisije pa predlaga dr. Kristijana Brecla, dr. Boštjana Glažarja in g. Miho Filipiča. Sledilo je glasovanje glede predlaganih kandidatov. Predlagani so bili soglasno potrjeni.

SKLEP št. 1:
Občni zbor je izvolil vse zgoraj navedene kandidate.

Dr. Janez Trontelj kot izvoljeni delovni predsednik prevzame vodenje občnega zbora.

4. TOČKA:
Poročilo o delu društva v zadnjem mandatu (S. Amon, I. Šorli, I. Pompe)

Poročilo predsednika društva (S. Amona)

Dr. Slavko Amon je kot predsednik društva opisal delovanje društva med obema občnima zboroma (od 22.6.2010 do 24.3.2011). Opisal je delovanje društva, IO in sekretariata na področju izdajanja revije, organizacije konferenc, poslovanja in administracije. Omenil je sodelovanje društva z drugimi institucijami (IMAPS, CO NAMASTE, TC SEMTO). Glej priloženo poročilo.

5. TOČKA:
Finančno poročilo (I. Šorli)

Dr. Šorli je dopolnil predsednikovo poročilo s konkretnimi podatki. Najprej je predstavil VSEBINSKO FINANČNO POROČILO od leta 2007 do 2009. Društvo je takrat poslovalo pozitivno, s presežkom prihodkov nad odhodki. Presežek se prišteje v društveni sklad. Največji delež prihodkov predstavljajo subvencije ARRS, nato plačane kotizacije s konferenc, nazadnje šele plačane članarine. Največje stroške društva predstavljajo plačani računi za revijo Informacije MIDEM, stroški organizacije konferenc in izplačani avtorski honorarji.

KONFERENCA MIDEM

Dr. Šorli je nadalje predstavil zgodovino organiziranja konferenc s strani društva od leta 1992 do 2010. Od leta 1998 se na pobudo dr. Dejana Križaja na konferencah en dan nameni delavnici. Vsako leto se konferenca organizira na različni lokaciji v Sloveniji. Udeležba na konferencah je med 60-80 udeleženci (tuji in domači). Število predstavljenih referatov niha med 50 -70, več je domačih kot tujih. Zaradi tega tudi ARRS obravnava konferenco kot domačo konferenco z mednarodno udeležbo. Želja je, da se poveča udeležba na 100 udeležencev na konferenco in da se jo popularizira. Od vsega začetka se držimo cilja, da se konferenco dobro organizira in izvede od začetka do konca. Poudariti moramo tudi to, da se pred konferenco zberejo vsi referati, ki so na njej predstavljeni in se izda zbornik referatov, ki ga udeleženci konference dobijo ob prijavi na mestu konference. To se je do zdaj izkazalo za zelo dobro potezo.

REVIJA INFORMACIJE MIDEM

Predstavljena je bila zgodovina izhajanje revije Informacije MIDEM. Revija se je najprej imenovala Informacije SSOSD

(Savezni odbor za elektronske sastavne delove), nato se je preimenovala v Informacije SSESD (Strokovna sekcija za elektronske sestavne dele in materiale pri Jugoslovanski zvezi ETAN), leta 1986 se revija preimenuje v Informacije MIDEM. Od leta 1988 je dr. Šorli glavni in odgovorni urednik revije, ki ostaja vse do danes. Leta 1998 postane faktor vpliva (IF) revije od 0 različen. Faktor vpliva se izračunava že 12 let, od leta do leta pa precej variira. Revija ima nizek faktor vpliva in vedno obstaja možnost, da se ga poviša. Ob tej priložnosti je bil narejen apel na prisotne in na njihove kolege, naj v svojih prispevkih, člankih citirajo revijo MIDEM. Podana je bila tudi samokritika, da revija izhaja z zamudo zaradi kroničnega pomanjkanja časa urednika. Revija se v fizični obliki in elektronski verziji tudi pošilja v večje knjižnice (npr. Thompson Scientific, Ebsco Industries,…), kjer hranijo znanstvene publikacije. Glej priloženo poročilo.

Poročilo tajnika (I. Pompe)

G. Igor Pompe je predstavil strukturo trenutnih članov društva (460). Povedal je, da je na leto od 100 do 200 plačanih članarin. Društvo ima tudi elektronsko bazo članov, v kateri je 200 imen in na katere se pošiljajo razna obvestila o delovanju društva. Podal je predlog, da bi se število članov lahko povečalo preko sodelovanja oziroma včlanjevanja tudi oseb, študentov,… npr. z Univerze v Mariboru. Dobro bi bilo tudi nasploh povečati število članov v društvu. Omenil je tudi, da ima društvo status posebnega družbenega pomena, kar bi bilo potrebno vzdrževati.

Prisotni niso imeli nobenih ugovorov na poročila.

6. TOČKA:
Poročilo nadzornega odbora (F. Smole)

V poročilu je v imenu nadzornega odbora dr. Franc Smole ugotovil, da je društvo v iztekajočem mandatnem obdobju izpolnjevalo ustaljene naloge v skladu s programom in pravili društva. Pri pregledu finančnega poslovanja ni ugotovil nepravilnosti. Glej poročilo.

7. TOČKA:
Poročilo o delu častnega razsodišča v zadnjem mandatu (J. Furlan)

Zaradi upravičene odsotnosti je poročilo dr. Jožeta Furlana prebral dr. Slavko Amon. Častno razsodišče v zadnjem mandatu ni zaznalo nobenih nepravilnosti pri delovanju članov društva in od članov ni dobilo nobene pobude za ukrepanje. Glej poročilo.

8. TOČKA:
Razprava o poročilih

Razprave ni bilo, saj ni bilo dodatnih vprašanj ali komentarjev.

Sledilo je GLASOVANJE O RAZREŠNICI DOSEDANJIH ORGANOV DRUŠTVA (izvršilni odbor, nadzorni odbor, častno razsodišče, sekretariat, predsednik, podpredsednik,…)

Pri glasovanju noben ni bil proti in noben se ni vzdržal. Dosedanji organi društva so bili soglasno razrešeni.

Poročila so bila prav tako soglasno sprejeta (noben ni bil proti, noben se ni vzdržal).

SKLEP št. 2:
Občni zbor soglasno sprejema poročila za minulo obdobje in vsem organom društva se soglasno podeli razrešnica za minulo obdobje.

9. TOČKA:
Predlogi in volitve novih organov društva

10. TOČKA:
Poročilo volilne komisije o izidu volitev

Glasovnice (priloga) so se razdelile prisotnim na občnem zboru. Po pregledu vpisanih na seznam prisotnih, je bilo število prisotnih članov 17. Izpolnjene glasovnice so se pobrale in v pregled in štetje jih je vzela volilna komisija, ki je bila izvoljena v 4. točki programa in zapisnika občnega zbora. Ugotovitve so naslednje:

- v 14 primerih so bili izvoljeni vsi predlagani kandidati v skupinah izvršilni odbor društva, nadzorni odbor društva in častno razsodišče društva,
- v 3 primerih je bil dodatno potrjen še kot predsednik dr. Marko Topič,
- v 3 primerih dodatno potrjen dr. Franc Smole kot član nadzornega odbora društva,
- v 2 primerih dodatno potrjen dr. Jože Furlan kot član častnega razsodišča,
- v 1 primeru dodatno potrjen g. Franc Jan kot član častnega razsodišča.

NOVO IZVOLJENI ORGANI DRUŠTVA SO :

IZVRŠILNI ODBOR DRUŠTVA:

predsednik društva: prof. dr. Marko Topič, univ. dipl. inž. el., UL Fakulteta za elektrotehnikopodpredsednica: prof. dr. Barbara Malič, univ. dipl. kem., Institut Jožef Stefan

podpredsednik: dr. Iztok Šorli, univ. dipl. fiz., Mikroiks d.o.o., Ljubljana

tajnik: Igor Pompe, univ. dipl. inž. el., upokojenec

blagajnik: prof. dr. Janez Trontelj, univ. dipl. inž. el., UL Fakulteta za elektrotehnikočlan: Darko Belavič, univ. dipl. inž. el., HIPOPT-RR, d.o.o., Šentjernej

član: prof. dr. Bruno Cvikl, univ. dipl. fiz., UM Fakulteta za gradbeništvočlan: Leopold Knez, univ. dipl. inž. el., Iskra TELA d.d., Ljubljana

član: dr. Miloš Komac, univ. dipl. kem., UL Fakulteta za kemijo in kemijsko tehnologijočlan: Jožef Perne, univ. dipl. inž. el., Zavod TC SEMTO, Ljubljana

član: prof. dr. Slavko Amon, univ. dipl. fiz.; UL Fakulteta za elektrotehnikočlan: prof. dr. Miran Mozetič, univ. dipl. fiz. , Institut Jožef Stefančlan: prof. dr. Marija Kosec, univ. dipl. kem., Institut Jožef Stefan

član: dr. Werner Reczek, Infineon AG, Austrija

član: prof. dr. Giorgio Pignatel, University of Perugia, Italija

član: prof. dr. Leszek J. Golonka, Technical University, Wroclaw, Poljska

NADZORNI ODBOR DRUŠTVA:

prof. dr. Franc Smole, univ. dipl. inž. el., UL Fakulteta za elektrotehnikomag. Andrej Pirih, univ. dipl. inž. el., Iskra zaščite d.o.o., Ljubljana

dr. Slavko Bernik, univ. dipl. kem., Institut Jožef Stefan

ČASTNO RAZSODIŠČE:

zasl. prof.dr. Jože Furlan, univ. dipl. inž. el., upokojenec

prof. dr. Radko Osredkar, univ. dipl. inž. el., UL Fakulteta za računalništvo in informatiko

Franc Jan, univ. dipl. fiz., upokojenec

SKLEP št. 2:
Občni zbor potrjuje rezultate volitev in izvolitev novih članov društvenih organov za naslednje triletno mandatno obdobje.

11. TOČKA :
Nagovor novega predsednika društva midem

Sledil je govor novoizvoljenega predsednika društva g. Marka Topiča. Zahvalil se je dosedanjemu vodstvu, zaželel uspešno delo novi sestavi in opisal prihodnje cilje društva:

- predlagal povečanje prepoznavnosti in obiska konferenc,
- vzpostavitev elektronske izdaje revije
- povezovanje z drugimi znanstvenimi revijami, ki imajo faktor vpliva večji kot 1,
- pohitritev izdajanja revije,
- izboljšati informiranje in komunikacijo društva,
- povezati posamezne laboratorije preko strokovnih izletov ali sejmov, ki jih organizira posamezen laboratorij,
- povečati vpetost podjetij v članstvo društva,
- budno spremljanje razpisov,…

Za dodatne informacije glej poročilo g. Topiča.

12. TOČKA:
Razno

Dr. Trontelj je dal predlog novemu vodstvu o pomlajevanju članstva tako, da mladi raziskovalci, študenti, ne bi plačevali članarine.

Dr. Topič je omenil (tudi predlog novega vodstva), da bi se ob 25. letnici ustanovitve društva (1986-2011) podelila priznanja dolgoletnim članom in dosedanjim predsednikom društva. Organiziral bi se dogodek v Ljubljani (verjetno kar na Fakulteti za elektrotehniko), na kateri bi bilo organizirano vabljeno predavanje (mogoče dr. Koščeve), nato bi sledila svečana podelitev priznanj in na koncu druženje. Dogodek bi se organiziral v spomladanskem času, verjetno v mesecu maju ali juniju. Vsi prisotni so se s predlogom strinjali.

Občni zbor je bil zaključen ob 15:15.

Zapisala: Polona Šorli

Predsednik delovnega predsedstva OZ
prof. dr. Janez Trontelj

Dosedanji predsednik društva
Prof. dr. Slavko Amon

Novoizvojeni predsednik društva
Prof. dr. Marko Topič

Overovitelja zapisnika:

prof. dr. Janez Krč
dr. Iztok Šorli

PRILOGE:

- poročilo predsednika MIDEM o delu društva v obdobju med občnima zboroma (22.6.2010-24.3.2011)
- poročilo o delu častnega razsodišča v zadnjem mandatu
- poročilo nadzornega odbora društva MIDEM
- poročilo o delu društva program dela in smernice delovanja društva v prihodnje

Informacije MIDEM
Strokovna revija za mikroelektroniko, elektronske sestavine dele in materiale

NAVODILA AVTORJEM

Informacije MIDEM je znanstveno-strokovno-društvena publikacija Strokovnega društva za mikroelektroniko, elektronske sestavne dele in materiale - MIDEM. Revija objavlja prispevke s področja mikroelektronike, elektronskih sestavnih delov in materialov. Ob oddaji člankov morajo avtorji predlagati uredništvu razvrstitev dela v skladu s tipologijo za vode-nje bibliografij v okviru sistema COBISS.
Znanstveni in strokovni prispevki bodo recenzirani.

Znanstveno-strokovni prispevki morajo biti pripravljeni na naslednji način:
1. Naslov dela, imena in priimki avtorjev brez titul, imena institucij in firm
2. Ključne besede in povzetek (največ 250 besed).
3. Naslov dela v angleščini.
4. Ključne besede v angleščini (Key words) in podaljšani povzetek (Extended Abstract) v angleščini, če je članek napisan v slovenščini
5. Uvod, glavni del, zaključek, zahvale, dodatki in literatura v skladu z IMRAD shemo (Introduction, Methods, Results And Discsussion).
6. Polna imena in priimki avtorjev s titulami, naslovi institucij in firm, v katerih so zaposleni ter tel./Fax/Email podatki.
7. Prispevki naj bodo oblikovani enostransko na A4 stra-neh v enem stolpcu z dvojnim razmikom, velikost črk namanj 12pt. Priporočena dolžina članka je 12-15 strani brez slik.

Ostali prispevki, kot so poljudni cčlanki, aplikacijski članki, novice iz stroke, vesti iz delovnih organizacij, inštitutov in fakultet, obvestila o akcijah društva MIDEM in njegovih članov ter drugi prispevki so dobrodošli.

Ostala splošna navodila
1. V članku je potrebno uporabljati SI sistem enot oz. v oklepaju navesti alternativne enote.
2. Risbe je potrebno izdelati ali iztiskati na belem papirju. Širina risb naj bo do 7.5 oz.15 cm. Vsaka risba, tabela ali fotografija naj ima številko in podnapis, ki označuje njeno vsebino. Risb, tabel in fotografij ni potrebno lepi-ti med tekst, ampak jih je potrebno ločeno priložiti članku. V tekstu je treba označiti mesto, kjer jih je potrebno vstaviti.
3. Delo je lahko napisano in bo objavljeno v slovenščini ali v angleščini.
4. Uredniški odbor ne bo sprejel strokovnih prispevkov, ki ne bodo poslani v dveh izvodih skupaj z elektronsko verzijo prispevka na disketi ali zgoščenki v formatih ASCII ali Word for Windows. Grafične datoteke naj bodo priložene ločeno in so lahko v formatu TIFF, EPS, JPEG, VMF ali GIF.
5. Avtorji so v celoti odgovorni za vsebino objavljenega sestavka.

Rokopisov ne vračamo. Rokopise pošljite na spodnji naslov.

Informacije MIDEM
Journal of Microelectronics, Electronic Components and Materials

INSTRUCTIONS FOR AUTHORS

Informacije MIDEM is a scientific-professional-social publication of Professional Society for Microelectronics, Electronic Components and Materials – MIDEM. In the Journal, scientific and professional contributions are published covering the field of microelectronics, electronic components and materials.
Authors should suggest to the Editorial board the classification of their contribution such as : original scientific paper, review scientific paper, professional paper…
Scientific and professional papers are subject to review.

Each scientific contribution should include the following:
1. Title of the paper, authors' names, name of the institution/company.
2. Key Words (5-10 words) and Abstract (200-250 words), stating how the work advances state of the art in the field.
3. Introduction, main text, conclusion, acknowledgements, appendix and references following the IMRAD scheme (Introduction, Methods, Results And Discsussion).
4. Full authors' names, titles and complete company/institution address, including Tel./Fax/Email.
5. Manuscripts should be typed double-spaced on one side of A4 page format in font size 12pt. Recommended length of manuscript (figures not included) is 12-15 pages
6. Slovene authors writing in English language must submit title, key words and abstract also in Slovene language.
7. Authors writing in Slovene language must submit title, key words and extended abstract (500-700 words) also in English language.

Other types of contributions such as popular papers, application papers, scientific news, news from companies, institutes and universities, reports on actions of MIDEM Society and its members as well as other relevant contributions, of appropriate length , are also welcome.

General informations
1. Authors should use SI units and provide alternative units in parentheses wherever necessary.
2. Illustrations should be in black on white paper. Their width should be up to 7.5 or 15 cm. Each illustration, table or photograph should be numbered and with legend added. Illustrations, tables and photographs must not be included in the text but added separately. However, their position in the text should be clearly marked.
3. Contributions may be written and will be published in Slovene or English language.
4. Authors must send two hard copies of the complete contributon, together with all files on diskette or CD, in ASCII or Word for Windows format. Graphic files must be added separately and may be in TIFF, EPS, JPEG, VMF or GIF format.
5. Authors are fully responsible for the content of the paper.

Contributions are to be sent to the address below.

M I D E M

Strokovno društvo za mikroelektroniko,
elektronske sestavne dele in materiale
MIDEM pri MIKROIKS
Stegne 11, 1521 Ljubljana
SLOVENIJA

TEL.: +386 (0)1 5133 768
FAX: +386 (0)1 5133 771
Email / WWW
iztok.sorli@guest.arnes.si
http://paris.fe.uni-lj.si/midem/

MIDEM SOCIETY REGISTRATION FORM

1. First Name ....Last Name...

   Adress ....

   City ....

   Country ....Postal Code ....

2. Date of Birth ....

3. Education (please, circle whichever appropriate)

   PhD   MSc   BSc   High School   Student

3. Profession (please, circle whichever appropriate)

   Electronics   Physics   Chemistry   Metallurgy   Material Sc.

4. Company ....

   Adress ....

   City ....

   Country ....Postal Code ....

   Tel.: ....FAX: ....

   Email ....

5. Your Primary Job Function

   Fabrication   Engineering   Facilities   QA/QC

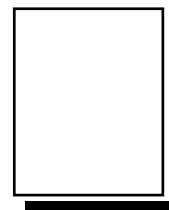   Management   Purchasing   Consulting   Other

6. Please, send mail to   a) Company adress   b) Home Adress

7. I wil regularly pay MIDEM membership fee, 25,00 EUR/year

MIDEM member recive Journal "Informacije MIDEM" for free !!!

Signature ....Date ....

MIDEM at MIKROIKS
Stegne 11

1521 Ljubljana
Slovenija

ORGANI DRUŠTVA MIDEM - BOARDS OF MIDEM

Predsednik društva MIDEM
MIDEM President

Prof. dr. Marko Topič, univ. dipl. inž. el., UL Fakulteta za elektrotehniko, Ljubljana, Slovenija

IZVRŠILNI ODBOR MIDEM - MIDEM EXECUTIVE BOARD

Podpredsednika
Vice-presidents

Prof. dr. Barbara Malič, univ. dipl. kem., Institut Jožef Stefan, Ljubljana, Slovenija
Dr. Iztok Šorli, univ. dipl. inž. fiz., MIKROIKS, d. o. o., Ljubljana, Slovenija

Tajnik
Secretary

Igor Pompe, univ. dipl. inž. el., Ljubljana, Slovenija

Člani izvršilnega odbora MIDEM
Executive Board Members

Prof. dr. Janez Trontelj, univ. dipl. inž. el., UL Fakulteta za elektrotehniko, Ljubljana, Slovenija, blagajnik
Darko Belavič, univ. dipl. inž. el., HIPOPT-RR, d.o.o., Šentjernej, Slovenija
Prof. dr. Bruno Cvikl, univ. dipl. fiz., UM Fakulteta za gradbeništvo, Maribor, Slovenija
Leopold Knez, univ. dipl. inž. el., Iskra TELA d.d., Ljubljana, Slovenija
Dr. Miloš Komac, univ. dipl. kem., UL Fakulteta za kemijo in kemijsko tehnologijo, Ljubljana, Slovenija
Jožef Perne, univ. dipl. inž. el., Zavod TC SEMTO, Ljubljana, Slovenija
Prof. dr. Slavko Amon, univ. dipl. fiz.; UL Fakulteta za elektrotehniko, Ljubljana, Slovenija
Prof. dr. Miran Mozetič, univ. dipl. fiz. , Institut Jožef Stefan, Ljubljana, Slovenija
Prof. dr. Marija Kosec, univ. dipl. kem., Institut Jožef Stefan, Ljubljana, Slovenija
Dr. Werner Reczek, Infineon AG, Austrija
Prof. dr. Giorgio Pignatel, University of Perugia, Italija
Prof. dr. Leszek J. Golonka, Technical University, Wroclaw, Poljska

Nadzorni odbor
Supervisory Board

Prof. dr. Franc Smole, univ. dipl. inž. el., Fakulteta za elektrotehniko, Ljubljana
Mag. Andrej Pirih, univ. dipl. inž. el., Iskra - Zaščite, d. o. o. , Ljubljana
Dr. Slavko Bernik, univ. dipl. inž. kem., Institut "Jožef Stefan", Ljubljana

Častno razsodišče
Court of Honour

Zasl. prof.dr. Jože Furlan, univ. dipl. inž. el.,Ljubljana, Slovenija
Prof. dr. Radko Osredkar, univ. dipl. inž. el., UL Fakulteta računalništvo in informatiko, Ljubljana
Franc Jan, univ. dipl. fiz., Kranj, Slovenija

Sponzorji MIDEM

JAVNA AGENCIJA ZA RAZISKOVALNO DEJAVNOST RS, Ljubljana

INSTITUT "JOŽEF STEFAN", Odsek za elektronsko keramiko, Ljubljana

FAKULTETA ZA ELEKTROTEHNIKO - LMFE, Ljubljana

FAKULTETA ZA ELEKTROTEHNIKO - LMSE, Ljubljana

FAKULTETA ZA ELEKTROTEHNIKO - LPVO, Ljubljana

MIKROIKS, d.o.o., Ljubljana

TC SEMTO, Ljubljana

ISKRA ZAŠČITE d.o.o., Ljubljana

RLS, d.o.o., Ljubljana